



*Advancing  
Astronomy and  
Geophysics*

## True versus apparent shapes of bow shocks

Journal:	<i>Monthly Notices of the Royal Astronomical Society</i>
Manuscript ID	MN-17-4291-MJ.R1
Manuscript type:	Main Journal
Date Submitted by the Author:	n/a
Complete List of Authors:	Tarango-Yong, Jorge; UNAM, IRyA Henney, W.J.; UNAM, IRyA
Keywords:	(stars:) circumstellar matter < Stars, hydrodynamics < Physical Data and Processes, stars: winds, outflows < Stars

SCHOLARONE™  
Manuscripts

# True versus apparent shapes of bow shocks

Jorge A. Tarango-Yong<sup>\*</sup> & William J. Henney<sup>†</sup>

*Instituto de Radioastronomía y Astrofísica, Universidad Nacional Autónoma de México, Apartado Postal 3-72, 58090 Morelia, Michoacán, México*

Accepted XXX. Received YYY; in original form ZZZ

## ABSTRACT

Astrophysical bow shocks are a common result of the interaction between two supersonic plasma flows, such as winds or jets from stars or active galaxies, or streams due to the relative motion between a star and the interstellar medium. For cylindrically symmetric bow shocks, we develop a general theory for the effects of inclination angle on the apparent shape. We propose a new two-dimensional classification scheme for bow shapes, which is based on dimensionless geometric ratios that can be estimated from observational images. The two ratios are related to the flatness of the bow’s apex, which we term *planitude* and the openness of its wings, which we term *alatitude*. We calculate the expected distribution in the planitude–alatitude plane for a variety of simple geometrical and physical models: quadrics of revolution, wilkinoids, cantoids, and ancantoids. We further test our methods against numerical magnetohydrodynamical simulations of stellar bow shocks and find that the apparent planitude and alatitude measured from infrared dust continuum maps serve as accurate diagnostics of the shape of the contact discontinuity, which can be used to discriminate between different physical models. We present an algorithm that can determine the planitude and alatitude from observed bow shock emission maps with a precision of 10 to 20%.

**Key words:** circumstellar matter – hydrodynamics – stars: winds, outflows

## 1 INTRODUCTION

The archetypal bow shock is formed when a solid body moves supersonically through a compressible fluid. Terrestrial examples include the atmospheric re-entry of a space capsule, or the sonic boom produced by a supersonic jet (van Dyke 1982). In astrophysics the term bow shock is employed more widely, to refer to many different types of curved shocks that have approximate cylindrical symmetry. Instead of a solid body, astrophysical examples usually involve the interaction of *two* supersonic flows, such as the situation of a stellar wind emitted by a star that moves supersonically through the interstellar medium (van Buren & McCray 1988; Kobulnicky et al. 2010; van Marle et al. 2011; Mackey et al. 2012, 2015). In such cases, two shocks are generally produced, one in each flow. Sometimes, especially in heliospheric studies (Zank 1999; Scherer & Fichtner 2014), the term “bow shock” is reserved for the shock in the ambient medium, with the other being called the “wind shock” or “termination shock”. However, in other contexts such as colliding wind binaries (Stevens et al. 1992; Gayley 2009) such a distinction is not so useful.

A further class of astrophysical bow shock is driven by highly collimated, supersonic jets of material, such as the Herbig Haro objects (Schwartz 1978; Hartigan et al. 1987) that are powered by jets from young stars or protostars. Additional examples are seen in planetary nebulae (Phillips et al. 2010; Meaburn et al. 2013),

active galaxies (Wilson & Ulvestad 1987), and in galaxy clusters (Markevitch et al. 2002). In the jet-driven case, the term “working surface” is often applied to the entire structure comprising the two shocks plus the shocked gas in between them, separated by a *contact discontinuity*. The working surface may be due to the interaction of the jet with a relatively quiescent medium, or may be an “internal working surface” within the jet that is due to supersonic temporal variations in the flow velocity (Raga et al. 1990).

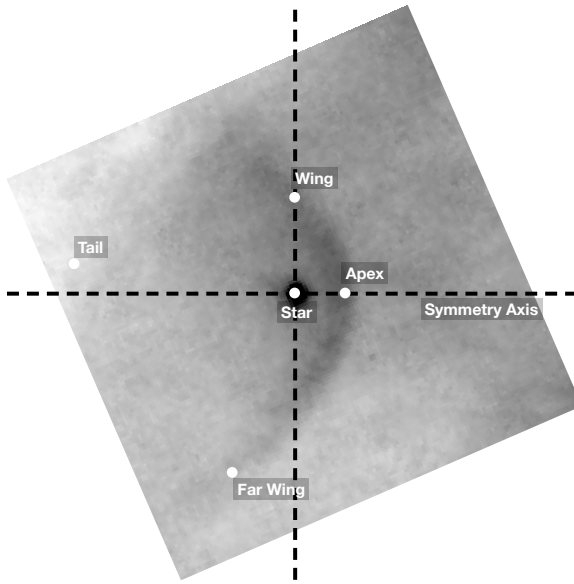
In empirical studies the relationship between these theoretical constructs and the observed emission structures is not always clear. In such cases the term “bow shock” is often used in a more general sense to refer to the entire arc of emission. In this paper, we will concentrate on *stellar bow shocks*, in which the position of the star can serve as a useful reference point for describing the bow shape. The empirical terminology that we will employ is illustrated in Figure 1. The *apex* is the point of closest approach of the bow to the star, which lies on the approximate symmetry axis, and the region around the apex is sometimes referred to as the *head* of the bow. The *wings* are the swept-back sides of the bow, which lie in a direction from the star that is orthogonal to the axis, with the *far wings* being the wing region farthest from the apex. Finally, the *tail* is the region near the axis but in the opposite direction from the apex.

Figure 2 shows an idealized schematic of how a double bow-shock shell is formed from the interaction of two supersonic streams: an *inner wind* and an *outer wind*, with the inner wind being the weaker of the two (in terms of momentum), so that the shell curves back around the inner source. The outer wind may be from another star, or may be a larger scale flow of the interstellar medium, such

\* E-mail: j.tarango@irya.unam.mx

† E-mail: w.henney@irya.unam.mx

1  
2      *Tarango-Yong & Henney*  
3  
4  
5  
6  
7  
8  
9  
10  
11  
12  
13  
14  
15  
16  
17  
18  
19  
20  
21  
22  
23  
24  
25



**Figure 1.** Descriptive terminology for a stellar bow shock. The apex is the closest approach of the bow to the star, while the wings are the parts of the bow that curve back past the star.

as the *champagne flow* produced by the expansion of an H II region away from a molecular cloud (Tenorio-Tagle 1979; Shu et al. 2002; Medina et al. 2014). Alternatively, it may be due to the supersonic motion of the inner source through a relatively static medium, in which case the outer wind will not be divergent as shown in the figure but rather plane-parallel. The thickness of the shocked shells at the apex depends on the Mach number,  $\mathcal{M}$ , of the flows and the efficiency of the post-shock cooling. For sufficiently strong cooling, the post-shock cooling zone thickness is negligible and the shock can be considered isothermal. In this case, the shell thickness is of order  $\mathcal{M}^{-2}$  times the source-apex separation (Henney 2002), which can become very small for high Mach numbers. The shell thickness will tend to increase towards the wings, due to the increasing shock obliqueness, which reduces the perpendicular Mach number.

In the extreme thin-shell limit, the entire bow structure can be treated as a surface. The bow radius measured from the inner source (star) is  $R(\theta, \phi)$ , where  $\theta$  is the polar angle, measured from the star-apex axis, and  $\phi$  is the azimuthal angle, measured around that axis. Assuming cylindrical symmetry about the axis, this reduces to  $R(\theta)$ , which is illustrated in Figure 3, following Canto et al. (1996). The separation between the two sources is  $D$  and the complementary angle, as measured at the position of the outer source, is  $\theta_1$ . The minimum value of  $R(\theta)$  is the stagnation radius,  $R_0$ , which occurs at the apex ( $\theta = 0$ ). In a steady state, ram-pressure balance on the axis implies that

$$\frac{R_0}{D} = \frac{\beta^{1/2}}{1 + \beta^{1/2}}, \quad (1)$$

where  $\beta$  is the momentum ratio between the two winds. If the winds are isotropic, with inner wind mass-loss rate  $\dot{M}_w$  and terminal velocity  $V_w$ , while the outer wind has corresponding values  $\dot{M}_{w1}$  and  $V_{w1}$ , then the momentum ratio is

$$\beta = \frac{\dot{M}_w V_w}{\dot{M}_{w1} V_{w1}}. \quad (2)$$

The case where the outer wind is a parallel stream (Wilkin 1996)

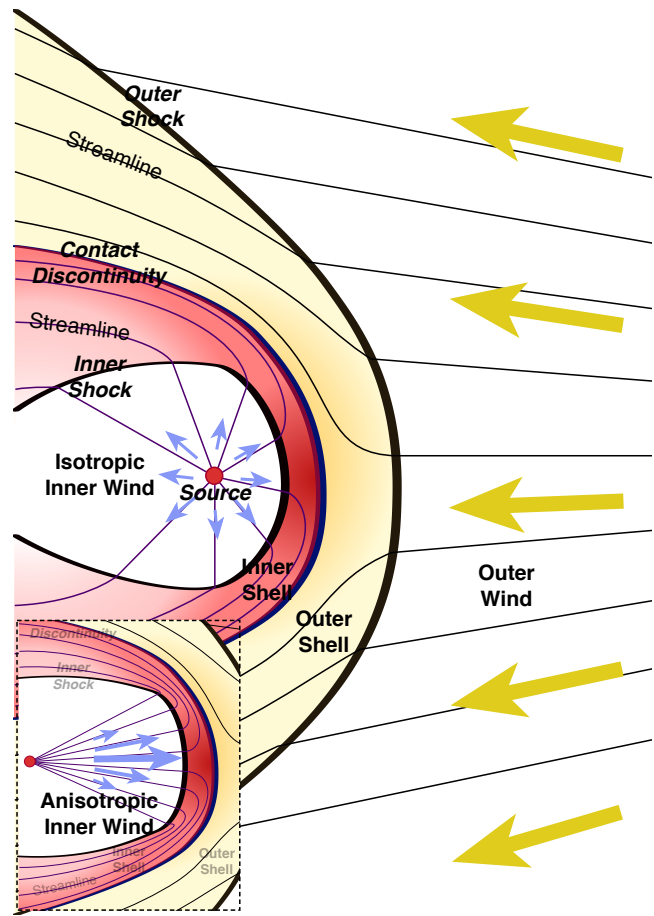


**Figure 2.** Quasi-stationary bow shock structure formed by the interaction of two supersonic winds. Lower-left inset box shows the case where the inner wind is anisotropic. The streamlines (thin lines) are drawn to be qualitatively realistic: they are straight in regions of hypersonic flow, but curved in subsonic regions, responding to pressure gradients in the shocked shells. Streamline slopes are discontinuous across oblique shocks.

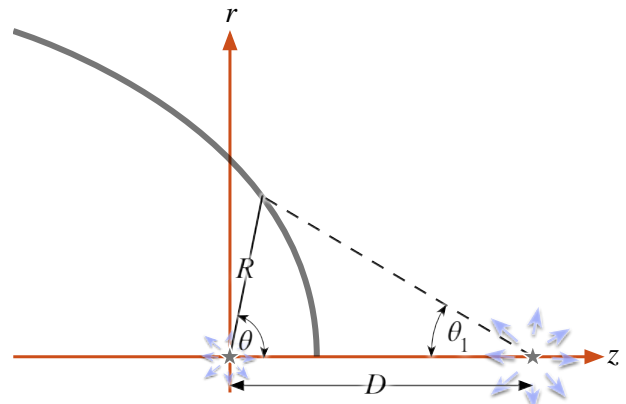


**Figure 3.** Schematic diagram of cylindrically symmetric two-wind interaction problem in the thin-shell limit, following Canto et al. (1996).

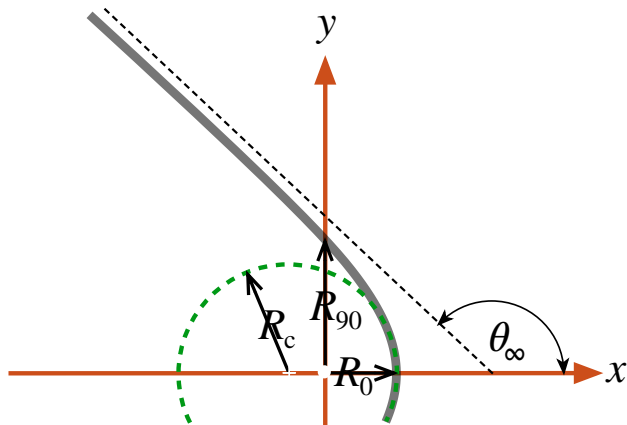


**Figure 4.** Parameters for characterizing a bow shape. Bow radius from the star, measured parallel ( $R_0$ ) and perpendicular ( $R_{90}$ ) to the symmetry axis, together with radius of curvature ( $R_c$ ) at apex and asymptotic opening angle ( $\theta_\infty$ ) of the far wings.

corresponds to the limit  $\beta \rightarrow 0$ , in which case  $D$  is no longer a meaningful parameter.

The paper is organized as follows. In § 2 we outline the geometric parameters that are necessary for describing bow shapes and introduce two dimensionless ratios: planitude and alatitude. In § 3 we derive general results for the projection of bow shapes on to the plane of the sky. In § 4 we apply the results to the simplest possible class of geometric bow models: the quadrics of revolution, which comprise spheroids, paraboloids, and hyperboloids, each of which occupies a distinct region of the planitude–alatitude plane. In § 5 we consider thin-shell hydrodynamic models for the parallel-stream case (wilkinoids) and wind-wind case (cantoids), including extension to an anisotropic inner wind (ancantoids). We calculate the location of the models in the planitude–alatitude plane as a function of the inclination of the bow shock axis to the plane of the sky. In § 6 we test our methods against the results of more realistic numerical simulations of bow shocks, including the derivation of the shape parameters from maps of infrared dust emission. In § 7 we apply our methods to example observations of proplyd bow shocks in the Orion Nebula, paying close attention to the systematic uncertainties that arise when our algorithms are applied to real data. In § 8 we summarise our results and outline how following papers will apply these ideas to observations and to a more extensive set of observations, models and numerical simulations.

## 2 PLANITUDE AND ALATITUDE OF BOW SHAPES

The stagnation radius  $R_0$  describes the linear scale of the bow shock, but in order to characterize its shape more parameters are required. To efficiently capture the diversity of bow shapes, we propose the parameters shown in Figure 4. The perpendicular radius  $R_{90}$  is the value of  $R(\theta)$  at  $\theta = 90^\circ$ , whereas  $R_c$  is the radius of curvature of the bow at the apex ( $\theta = 0$ ). For a cylindrically symmetric bow, we show in Appendix A that this is given by

$$R_c = \frac{R_0^2}{R_0 - R_{\theta\theta,0}}, \quad (3)$$

where  $R_{\theta\theta,0}$  is  $d^2R/d\theta^2$  evaluated at  $\theta = 0$ .

A fourth parameter is the asymptotic opening angle of the far wings,  $\theta_\infty$ , which is useful in the case that the wings are asymptotically conical. However, in many bow shocks the wings tend towards the asymptotic angle only slowly, making  $\theta_\infty$  difficult to measure, especially since the emission from the far wings is often weak at best. In contrast, the three radii,  $R_0$ ,  $R_{90}$ , and  $R_c$ , are straightforward to determine from observations. One simple method to estimate the radius of curvature is to make use of the Taylor expansion<sup>1</sup> of  $R(\theta)$  about the apex (with  $\theta$  in radians):

$$R(\theta) = R_0 + \frac{1}{2} R_{\theta\theta,0} \theta^2 + O(\theta^4), \quad (4)$$

so that fitting a polynomial in  $\theta^2$  to  $R(\theta)$  for  $|\theta| < \Delta\theta$  yields  $R_0$  and  $R_{\theta\theta,0}$  from the first two coefficients, and hence  $R_c$  from equation (3). Experience has shown that  $\Delta\theta = 30^\circ$  and three terms in the polynomial are good choices, where the third term is used only as a monitor (if the co-efficient of  $\theta^4$  is not small compared with  $R_0$ , then it may indicate a problem with the fit).

Since we have three radii, we can construct two independent dimensionless parameters:

$$\text{Planitude } \Pi \equiv \frac{R_c}{R_0} \quad (5)$$

$$\text{Alatitude } \Lambda \equiv \frac{R_{90}}{R_0} \quad (6)$$

and these will be the principal shape parameters that we will use in the remainder of the paper. The *planitude*,  $\Pi$ , is a measure of the flatness of the head of the bow around the apex, while the *alatitude*,  $\Lambda$ , is a measure of the openness of the bow wings. Although “planitude” can be found in English dictionaries, “alatitude” is a new word that we introduce here, derived from the latin *ala* for “wing”.

Several previous studies have discussed the relation between  $R_{90}$  and  $R_0$  as a diagnostic of bow shape (for example Cox et al. 2012; Meyer et al. 2016; Robberto et al. 2005; Cox et al. 2012; Meyer et al. 2016), but as far as we know, we are the first to include  $R_c$ . Robberto et al. (2005) § 4.2 use the ratios  $R_0/D$  and  $R_{90}/D$  in analyzing proplyd bow shapes in the Trapezium cluster in the center of the Orion Nebula (Hayward et al. 1994; García-Arredondo et al. 2001; Smith et al. 2005). In that case, the source of the outer wind is known, and so  $D$  is well-determined (at least, in projection), but for many bow shocks  $D$  is not known, and is not even defined for the moving-star or parallel-stream case. Cox et al. (2012) § 4.1 compare the observed shapes of bow shocks around cool giant stars with an analytic model, and use  $A$  and  $B$  for the projected values of  $R_0$  and  $R_{90}$ , respectively (see next section for discussion of projection effects). Meyer et al. (2016) § 3.2 analyze the distribution of  $R_0/R_{90}$  (the reciprocal of our  $\Lambda$ ) for hydrodynamic simulations of bow shocks around runaway OB stars.

## 3 PROJECTION ONTO THE PLANE OF THE SKY

In this section we calculate the apparent shape on the plane of the sky of the limb-brightened border of a shock or shell that is idealized as an arbitrary cylindrically symmetric surface.

<sup>1</sup> This method assumes both that  $R(\theta)$  is even (true for a cylindrically symmetric bow) and that the orientation of the axis is already known. Generalization to cases where these assumptions do not hold is discussed in Appendix E.

## 4 Tarango-Yong & Henney

### 3.1 Frames of reference

Consider body-frame cartesian coordinates  $(x, y, z)$ , where  $x$  is the symmetry axis, and spherical polar coordinates  $(R, \theta, \phi)$ , where  $\theta$  is the polar angle and  $\phi$  the azimuthal angle. Since the surface is cylindrically symmetric, it is can be specified as  $R = R(\theta)$ , so that cartesian coordinates on the surface are:

$$\mathbf{r} \equiv \begin{pmatrix} x \\ y \\ z \end{pmatrix} = \begin{pmatrix} R(\theta) \cos \theta \\ R(\theta) \sin \theta \cos \phi \\ R(\theta) \sin \theta \sin \phi \end{pmatrix}. \quad (7)$$

Suppose that the viewing direction makes an angle  $i$  with the  $z$  axis, so that we can define observer-frame coordinates  $(x', y', z')$ , which are found by rotating the body-frame coordinates about the  $y$  axis.

The same vector,  $\mathbf{r}$ , expressed in the observer frame is then

$$\mathbf{r} = \begin{pmatrix} x' \\ y' \\ z' \end{pmatrix} = \mathbf{A}_y(i) \begin{pmatrix} x \\ y \\ z \end{pmatrix} = \begin{pmatrix} x \cos i - z \sin i \\ y \\ z \cos i + x \sin i \end{pmatrix}, \quad (8)$$

where the rotation matrix  $\mathbf{A}_y(i)$  is given in Appendix B. The inclination angle  $i$  is defined so that  $i = 0^\circ$  when the surface is viewed perpendicular to its axis (*side on*) and  $i = \pm 90^\circ$  when it is viewed along its axis (*end on*), with positive  $i$  when the apex points towards the observer.

The relationship between the two frames is illustrated in Figure 5. All quantities in the observer's frame are denoted by attaching a prime to the equivalent quantity in the body frame.

There are two ways of interpreting the primed coordinates. On the one hand, the 3-vector  $(x', y', z')$  specifies a point in Euclidean space,  $\mathbb{R}^3$ , but an alternative interpretation is to take the 2-vector  $(x', y')$  as specifying a point in a projective space,  $\mathbb{P}^2$  (see, for example, § 15.6 of Penrose 2004). Each ‘‘point’’ in  $\mathbb{P}^2$  is equivalent to a line in  $\mathbb{R}^3$ , specifically: a line of sight that passes through the observer. Thus,  $(x', y')$  gives the celestial coordinates on the *plane of the sky*, with  $x'$  being the projected symmetry axis of the surface while the line of sight lies along  $-z'$ . The inclination angle  $i$  is defined so that  $i = 0^\circ$  when the surface is viewed perpendicular to its axis (*side on*) and  $i = 90^\circ$  when it is viewed along its axis (*end on*). We assume that the observer is located at a very large distance, relative to the size of the bow, so that all lines of sight are effectively parallel to the  $z'$  axis, with the observer at  $z' = -\infty$ . But, from the point of view of the plane of the sky, the  $z'$  coordinate is strictly irrelevant since it is a projective plane, and not a Euclidean plane. In the following, we will switch between the  $\mathbb{R}^3$  and  $\mathbb{P}^2$  interpretations as convenient, resolving ambiguity where necessary via the adjectives ‘‘Euclidean’’ for  $\mathbb{R}^3$  and ‘‘plane-of-sky’’ or ‘‘projected’’ for  $\mathbb{P}^2$ .

### 3.2 Unit vectors normal and tangential to the surface

We define unit vectors  $\hat{\mathbf{n}}$ ,  $\hat{\mathbf{t}}$ , such that  $\hat{\mathbf{n}}$  is normal to the surface, while  $\hat{\mathbf{t}}$  is tangent to the surface in a plane of constant  $\phi$ . For  $\phi = 0$  the surface lies in the  $xy$  plane and it is straightforward to show (Fig. 6) that in this case the unit vectors are given by

$$\hat{\mathbf{t}}_0 = \begin{pmatrix} -\cos \alpha \\ \sin \alpha \\ 0 \end{pmatrix} \quad \text{and} \quad \hat{\mathbf{n}}_0 = \begin{pmatrix} \sin \alpha \\ \cos \alpha \\ 0 \end{pmatrix}, \quad (9)$$

where  $\alpha$  is the *slope angle*, given by

$$\tan \alpha = -\left. \frac{dy}{dx} \right|_{R(\theta)} = \frac{1 + \omega \tan \theta}{\tan \theta - \omega} \quad (10)$$

and  $\omega$  is a dimensionless *local growth factor*:

$$\omega(\theta) = \frac{1}{R} \frac{dR}{d\theta}. \quad (11)$$

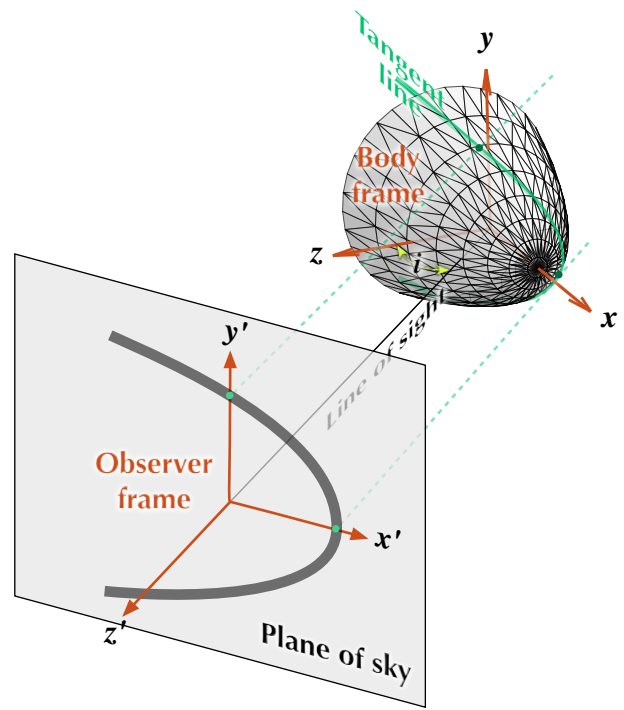


**Figure 5.** Relationship between body frame (unprimed coordinates) and observer frame (primed coordinates). Note that the plane of the sky is a projective plane, not a geometric plane in Euclidean 3-space, see discussion in text.

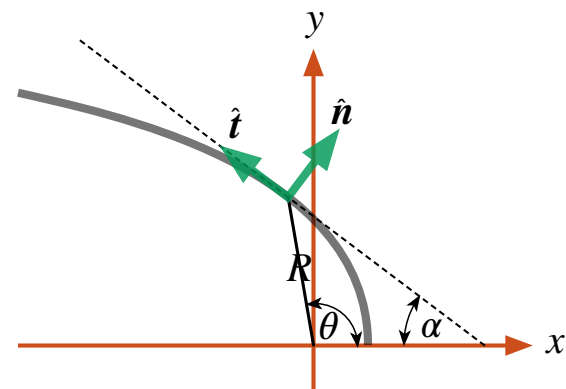


**Figure 6.** Unit vectors in the body frame that are normal and tangential to the surface  $R(\theta)$  in a plane of constant azimuth,  $\phi$ .

For general  $\phi \neq 0$ , we find  $\hat{\mathbf{n}}$  and  $\hat{\mathbf{t}}$  by rotating equations (9) around the  $x$ -axis (and then converting to the observer frame by use of equation (8)) to give with the matrix

$\mathbf{A}_x(\phi)$  (eq. [B5]):

$$\hat{\mathbf{n}} = \mathbf{A}_x(\phi) \hat{\mathbf{n}}_0 = \begin{pmatrix} \sin \alpha \\ \cos \alpha \cos \phi \\ \cos \alpha \sin \phi \end{pmatrix} \quad (12)$$

$$\hat{\mathbf{t}} = \mathbf{A}_x(\phi) \hat{\mathbf{t}}_0 = \begin{pmatrix} -\cos \alpha \\ \sin \alpha \cos \phi \\ \sin \alpha \sin \phi \end{pmatrix}. \quad (13)$$

### 3.3 Tangent line

The boundary on the plane of the sky of the projected surface is the locus of those lines of sight that graze the surface tangentially. This corresponds to a curved line on the surface itself, which we denote the *tangent line*, and which is defined by the condition

$$\hat{\mathbf{n}} \cdot \hat{\mathbf{z}}' = 0. \quad (14)$$

We denote by  $\phi_T$  that value of  $\phi$  that satisfies this relation for a given inclination,  $i$ , and polar angle,  $\theta$ . From equations (12, 14, B4, 10) this is

$$\sin \phi_T = -\tan i \tan \alpha = \tan i \frac{1 + \omega \tan \theta}{\omega - \tan \theta}. \quad (15)$$

From equations (7, 8) it follows that the observer-frame coordinates of the tangent line are given by

$$\begin{pmatrix} x'_T \\ y'_T \\ z'_T \end{pmatrix} = R(\theta) \begin{pmatrix} \cos \theta \cos i - \sin \theta \sin \phi_T \sin i \\ \sin \theta (1 - \sin^2 \phi_T)^{1/2} \\ \cos \theta \sin i + \sin \theta \sin \phi_T \cos i \end{pmatrix}. \quad (16)$$

Note that, in general,  $z'_T$  is not a linear function of  $x'_T$  and  $y'_T$ , so that the tangent line  $(x'_T, y'_T, z'_T)$  is not a plane curve.

The apparent in 3-dimensional Euclidean space,  $\mathbb{R}^3$ . However, for the projected shape  $(x'_T, y'_T)$  of the tangent line on the plane of the sky,  $\mathbb{P}^2$ , the value of  $z'_T$  does not matter (see above). The projected shape can also be described in polar form as  $R'(\theta')$ , where

$$R' = (x'^2_T + y'^2_T)^{1/2} \quad \text{and} \quad \tan \theta' = y'_T / x'_T. \quad (17)$$

Note that equation

Equation (15) will not have a solution for arbitrary values of  $\theta$  and  $i$ , but only when  $|\tan i \tan \alpha| < 1$ . In particular, if  $i \neq 0$ , then the tangent line only exists for  $\theta > \theta_0$  where  $\theta_0$  is the value of  $\theta$  on the tangent line's projected symmetry axis ( $\theta' = 0$ ) given implicitly by. From equations (16, 17) it follows that  $\sin^2 \phi_T = 1$  at  $\theta = \theta_0$ , which yields the implicit equation

$$\tan \theta_0 = \frac{|\tan i| + \omega(\theta_0)}{1 - \omega(\theta_0)|\tan i|}. \quad (18)$$

In addition, if the surface is sufficiently “open” ( $\alpha \geq \alpha_{\min} > 0$  for all  $\theta$ ), then for those inclinations with  $|i| > (90^\circ - \alpha_{\min})$  the tangent line does not exist for any value of  $\theta$ . In other words, when the viewing angle is sufficiently close to face-on, the projected surface has no “edge” and will no longer look like a bow shock to the observer.

After completing this work, it was brought to our attention that the principal results of this section had already been derived in Appendix B of the PhD thesis Wilkin (1997). For instance, Wilkin's equation (8) is equivalent (apart from differences in notation) to our equation (15).

### 3.4 Characteristic radii on the plane of the sky

In order to compare the shell shape given by  $R(\theta)$  with observations, it is convenient to define the following apparent radii in the observer

frame:  $R'_0$  and  $R'_{90}$ . These are projected distances of the shell tangent line from the origin. The first is measured in the direction of the symmetry axis, and the second in a perpendicular direction. More concretely  $R'_0 = x'_T(y'_T = 0)$  and  $R'_{90} = y'_T(x'_T = 0)$ . From equations (15) and (16) we find that:

$$R'_0 = R(\theta_0) \cos(\theta_0 + i) \quad (19)$$

Where  $\theta_0$  is the solution of equation (18), and

$$R'_{90} = R(\theta_{90}) \sin \theta_{90} \left(1 - \sin^2(\phi_T(\theta_{90}))\right)^{1/2} \quad (20)$$

Where  $\theta_{90}$  is the solution of the implicit equation:

$$\cot \theta_{90} = \frac{1 - (1 + \omega(\theta_{90})^2 \sin^2 2i)^{1/2}}{2\omega(\theta_{90}) \cos^2 i} \quad (21)$$

The projected alatitude (see § 2) is then given by  $\Lambda' = R'_{90}/R'_0$ .

Similarly, the projected planitude is  $\Pi' = R'_c/R'_0$ , where  $R'_c$  is found by applying the equivalent of equation (3) for primed quantities:

$$R'_c = \frac{(R'_0)^2}{R'_0 - R'_{\theta' \theta', 0}}. \quad (22)$$

### 3.5 Line-of-sight velocities on the tangent line

Motions in a thin shocked shell will be predominantly tangential to the shell surface. In addition, for the particular case of wind-wind bowshocks, the flow in each azimuthal slice can be shown to be independent (Wilkin 2000), which implies that the shell velocity is parallel to  $\hat{\mathbf{t}}$ . The projected line-of-sight shell velocity is therefore

$$v_{\text{los}} = (\hat{\mathbf{t}}' \cdot -\hat{\mathbf{z}}') v_{\parallel}(\theta) = \frac{v_{\parallel}(\theta)(1 + \omega^2)^{1/2} \sin i}{\sin \theta - \omega \cos \theta}, \quad (23)$$

where  $v_{\parallel}(\theta)$  is the gas velocity along the shell and the standard sign convention has been adopted such that velocities away from the observer are deemed positive.

## 4 QUADRICS OF REVOLUTION

For an arbitrary surface of revolution, application of equations (15, 16) to determine the projected shape of the tangent line is not straightforward and in general requires numerical techniques. However, analytical results can be found for the important class of surfaces known as *quadratics of revolution* (Goldman 1983; Gfrerrer & Zsombor-Murray 2009), which are formed by rotating a conic section plane curve about its symmetry axis. Examples are the sphere, spheroids (oblate and prolate), and right circular paraboloids and hyperboloids.<sup>2</sup> We ignore the degenerate cases of cylinders, cones, and pairs of parallel planes. While mathematically simple, these quadratics are sufficiently flexible that they can provide a useful approximation to more complex bow shock shapes.

The shape of the quadratic curves in the  $xy$  plane ( $\phi = 0$ ) are shown in Figure 7(a) and (b) for the ellipse and hyperbola case, respectively. The conic section itself is fully described by two lengths,  $a$  and  $b$ , which are the semi-axes.<sup>3</sup> However, the curve can

<sup>2</sup> We consider only the case of a single sheet of a 2-sheet hyperboloid or paraboloid, since these are the versions that resemble a bow, whereas the 1-sheet versions resemble the waist of an hourglass.

<sup>3</sup> Note that we do not require that  $a > b$ , so either  $a$  or  $b$  may be the semi-major axis.

## 6 Tarango-Yong & Henney

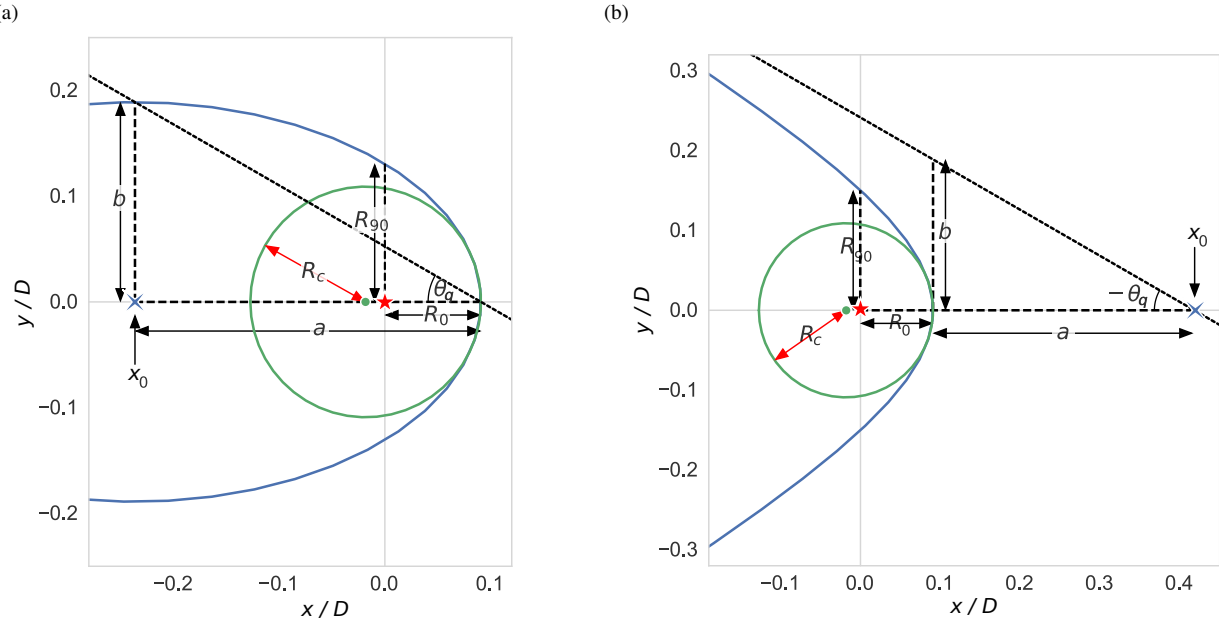


**Figure 7.** Example off-center conic sections that can form quadrics of revolution: (a) ellipse, (b) hyperbola. The relationship is shown between the conic section parameters  $a$ ,  $b$ ,  $\theta_Q$  and the bowshock characteristic radii  $R_0$ ,  $R_{90}$ ,  $R_c$ , as defined in Fig. 4. The origin (center of the weaker flow) is indicated by a red star, the center of curvature of the apex of the bow shock is indicated by a green dot, and the geometric center of the conic section is indicated by a blue cross, which is offset by  $x_0$  from the origin. Note that  $R_0$ ,  $R_{90}$ ,  $R_c$ ,  $a$ , and  $b$  are all lengths and are always positive, whereas  $x_0$  is a displacement and may be positive or negative.

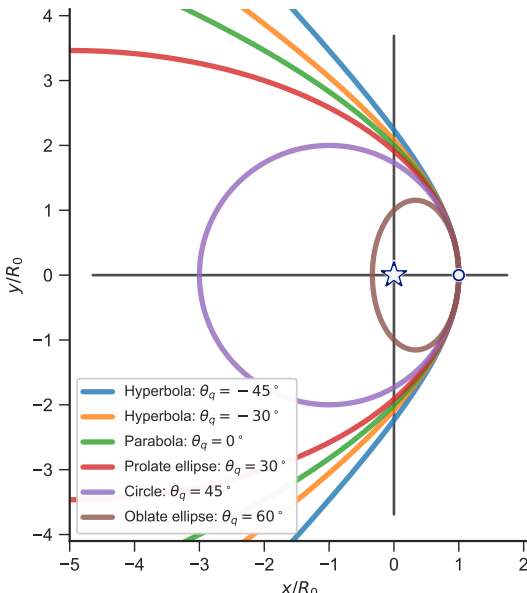


**Figure 8.** Example of a family of conic sections, all with the same planitude (flatness at apex, marked by white dot):  $\Pi = R_c/R_0 = 2$ . The quadric angle,  $\theta_Q$ , varies over the family (see text), with lower values of  $\theta_Q$  giving larger values of the alatitude,  $\Lambda = R_{90}/R_0$ , meaning more open wings. Different values of  $\Pi$  can be achieved for the exact same quadrics by sliding them along the  $x$ -axis, which will also change the axis scales since these are normalized by  $R_0$ .

be translated along the  $x$  axis to an arbitrary point with respect to the star, so that the apex distance  $R_0$  has no necessary relation to  $a$  or  $b$  and therefore the star/bow combination requires three independent lengths for its specification. The displacement  $x_0$  from the star to the “center” of the conic section is

$$x_0 = R_0 - \sigma a \quad \text{with} \quad \sigma = \begin{cases} +1 & \text{ellipse} \\ -1 & \text{hyperbola} \end{cases}. \quad (24)$$

For hyperbolas the center is “outside” of the bow and  $x_0$  is always positive, whereas for ellipses the center is “inside” the bow and  $x_0$  is usually negative, except when  $a < R_0$  (see Figure 7).

A general parametric form<sup>4</sup> for the  $xy$  coordinates of the quadrics (in the  $\phi = 0$  plane, and with the star at the origin) as a function of  $t = [0, \pi]$  is then

$$\begin{aligned} x &= x_0 + \sigma a C(t) \\ y &= b S(t) \end{aligned} \quad (25)$$

where

$$S, C = \begin{cases} \sin, \cos & \text{ellipse} \\ \sinh, \cosh & \text{hyperbola} \end{cases} \quad (26)$$

Except for the circle case ( $\sigma = +1$ ,  $a = b$ ), the parametric variable  $t$  is not actually an angle in physical space. Instead, the polar form of the bow shape  $R(\theta)$  must be found by substituting equations (25) into  $\theta = \tan^{-1} y/x$  and  $R = (x^2 + y^2)^{1/2}$ .

The type of quadric surface can be characterized by the *quadric parameter*:

$$Q \equiv \sigma \frac{b^2}{a^2}, \quad (27)$$

<sup>4</sup> The special case of the parabola needs to be treated differently, see Appendix C.

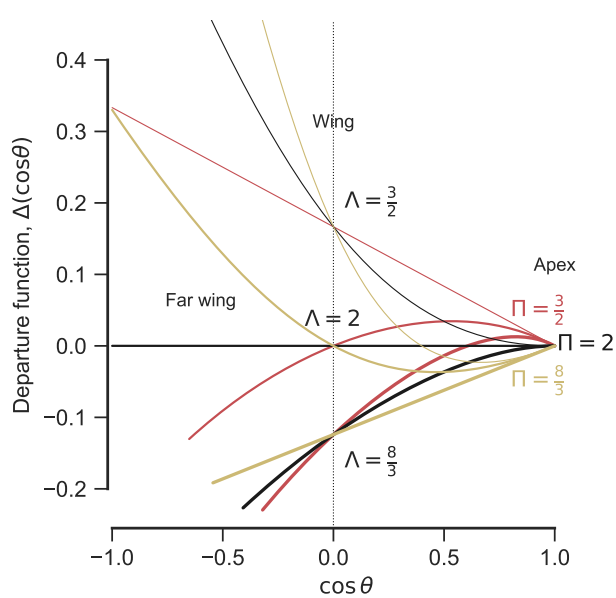


**Figure 9.** Parabolic departure function,  $\Delta(\cos\theta)$ , for conic sections with different planitude and alatitude, centered on that of the confocal parabola,  $(\Pi, \Lambda) = (2, 2)$ , which has  $\Delta(\cos\theta) = 0$ . Planitude (shown by different line colors) determines the slope of  $\Delta$  at the apex,  $\cos\theta = 1$ . Alatitude (shown by different line widths) determines the value of  $\Delta$  at  $\cos\theta = 0$ . All conics with  $\Pi = \Lambda$  have departure functions that are straight lines.

where  $Q < 0$  corresponds to open surfaces (hyperboloids) and  $Q > 0$  corresponds to closed surfaces (oblate spheroids with  $Q > 1$  and prolate spheroids with  $Q < 1$ ). Special cases are the sphere ( $Q = 1$ ) and the paraboloid ( $Q = 0$ ). Alternatively, one can define a *quadric angle*:

$$\theta_Q = \sigma \tan^{-1}(b/a), \quad (28)$$

which is marked in Figure 7. In the case of hyperboloids, the asymptotic opening angle of the wings (§ 2 and Fig. 4) is  $\theta_\infty = \pi + \theta_Q$  (note that  $\theta_Q < 0$  in this case), and the minimum slope angle is  $\alpha_{\min} = |\theta_Q|$ , see discussion following equation (18).

The set of parameters  $(Q, a, x_0)$  are then sufficient to characterize the star/bow combination, where  $a$  is the quadric scale and  $x_0$  is its center displacement from the star. However, we can also characterize the star/bow by  $(R_0, \Pi, \Lambda)$ , where  $R_0$  is the star-apex distance, and  $\Pi$  and  $\Lambda$  are the planitude and alatitude, see § 2. We now derive the equivalences between these two descriptions. The apex radius of curvature for a conic section is

$$R_c = \frac{b^2}{a} = a|Q|, \quad (29)$$

whereas the perpendicular radius,  $R_{90}$ , is the value of  $y$  when  $x = 0$ , which can be found from equations (24, 25) as

$$R_{90}^2 = Q(a^2 - x_0^2). \quad (30)$$

Combining equations (5, 6, 24, 27–30) yields

$$R_0 = x_0 + \sigma a \quad (31)$$

$$\Pi = \frac{aQ}{a + \sigma x_0} \quad (32)$$

$$\Lambda = \left( Q \frac{a - \sigma x_0}{a + \sigma x_0} \right)^{1/2} \quad (33)$$

with  $\sigma = \text{sgn } Q$ . It also follows that the quadric parameter in terms of the planitude and alatitude is

$$Q = 2\Pi - \Lambda^2 \quad (34)$$

Hence, it is the sign of  $2\Pi - \Lambda^2$  that determines  $\sigma$  and whether a quadric is a spheroid or a hyperboloid. For example, for a constant planitude,  $\Pi$ , we can have a family of different quadric types, with varying alatitude,  $\Lambda$ , that increases from oblate, through prolate and paraboloid, to hyperboloid, as illustrated in Figure 8.

#### 4.1 Parabolic departure function

The special case of confocal conic sections ( $\Lambda = \Pi$ ) can be written in polar form as

$$R(\theta) = R_0 \frac{1 + e}{1 + e \cos\theta} \quad (35)$$

where  $e = (1 - Q)^{1/2}$  is the *conic eccentricity*. For the confocal parabola ( $e = 1$ ), the dimensionless reciprocal radius is therefore  $R_0/R(\theta) = \frac{1}{2}(1 + \cos\theta)$ , which suggests the following form for a *departure function* that measures the difference between a given shape  $R(\theta)$  and the parabola:

$$\Delta(\cos\theta) = \frac{R_0}{R(\theta)} - \frac{1}{2}(1 + \cos\theta). \quad (36)$$

From equations (35) and (36) it is clear that  $\Delta$  is a linear function of  $\cos\theta$  for other confocal conics, being positive for ellipses ( $e < 1$ ) and negative for hyperbolae ( $e > 1$ ). Examples are shown in Figure 9 for a grid of 9 conics centered on the confocal parabola, with  $(\Pi, \Lambda)$  ranging from  $3/4$  to  $4/3$  of  $(2, 2)$ . The hyperbolae have negative values of  $\Delta$  in the far wings, with tracks that end at  $\cos\theta_\infty$ .

Strictly speaking, the departure function is redundant if one is interested in only conic sections, since they are fully determined by  $\Pi$  and  $\Lambda$ . Nonetheless, as we will show in following sections, it is a useful tool for studying general  $R(\theta)$ , being very sensitive to small variations in the shape.

#### 4.2 Plane-of-sky projection of quadric surfaces

We now apply the machinery of § 3 to find the projected shape of a quadric bow on the plane of the sky. The intrinsic 3D shape of the shell is given by rotating equations (25) about the  $x$ -axis, but it is more convenient to first transform to a reference frame where the origin is at the center of the conic section:

$$(X, Y, Z) = (x - x_0, y, z). \quad (37)$$

In this new frame, the quadric shape is

$$\begin{aligned} X &= a C(t) \\ Y &= b S(t) \cos\phi \\ Z &= b S(t) \sin\phi \end{aligned} \quad (38)$$

## 8 Tarango-Yong &amp; Henney

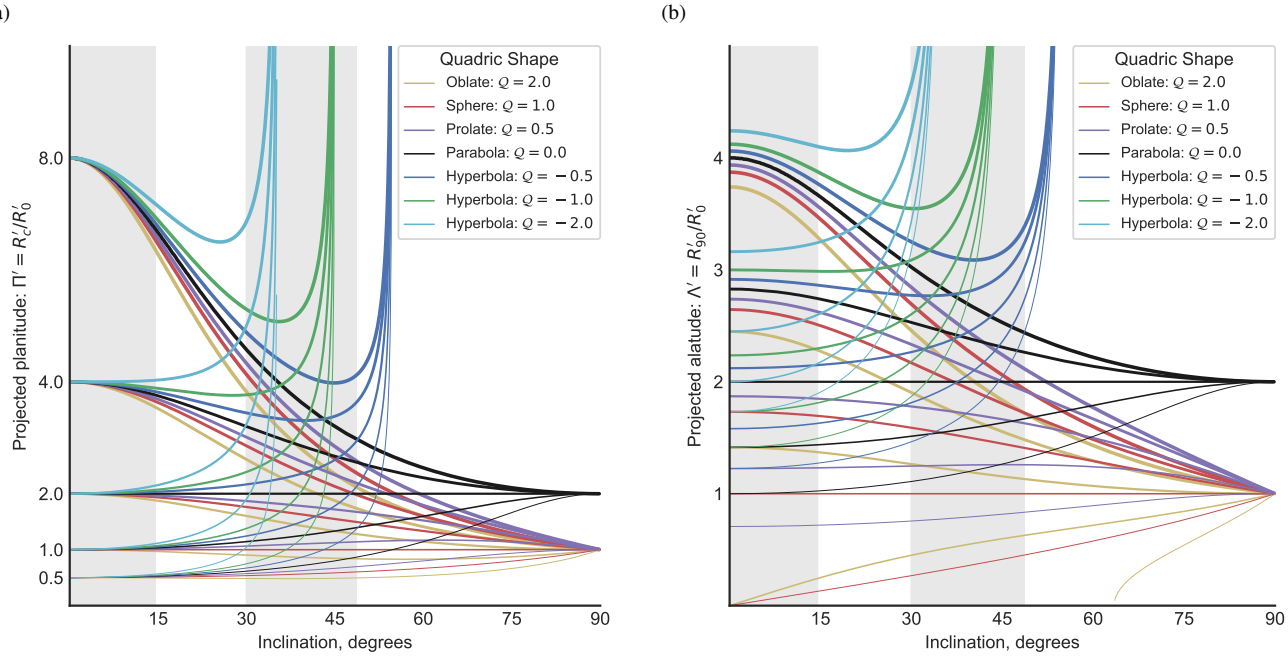


**Figure 10.** Effects of projection on quadrics of revolution: variation with inclination,  $|i|$ , of bow size and shape. Different line colors correspond to varying quadric parameter,  $Q$ , (see key), while variation in line width corresponds to variation in the “true” planitude,  $\Pi$ , or apex radius of curvature. Vertical gray rectangles show quartiles of  $|\sin i|$ , which will be equally populated for an isotropic distribution of orientations. (a) Projected planitude:  $\Pi'$ . (b) Projected alatitude,  $\Lambda'$ .

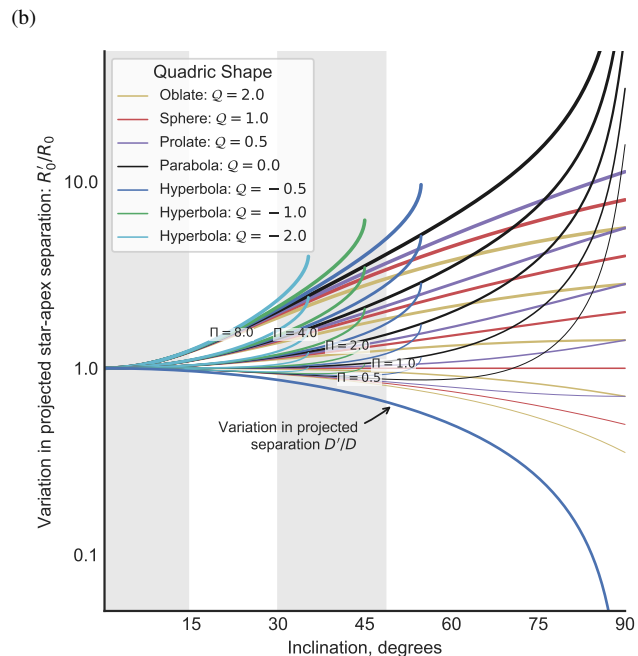
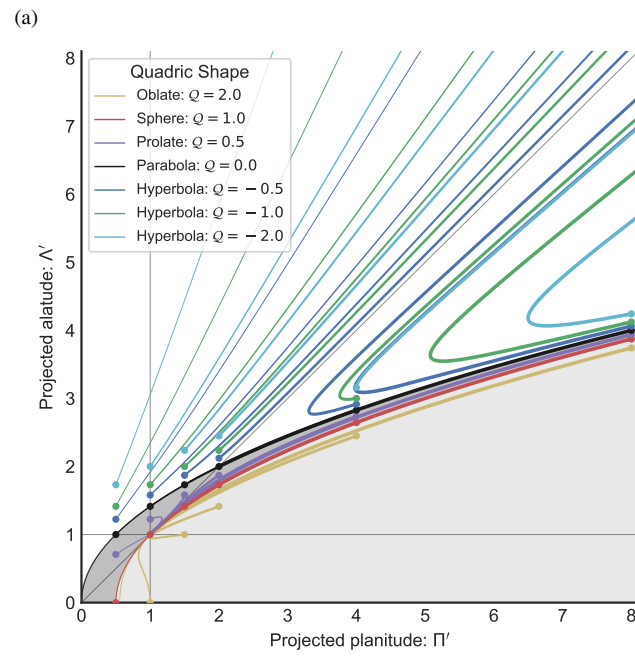


**Figure 11.** As Figure 10, but (a) diagnostic planitude–alatitude diagram:  $\Lambda'$  versus  $\Pi'$ , and (b) projected/true star-apex distance:  $R'_0/R'_0$  versus  $|i|$ . In (a), shading indicates different classes of quadrics: hyperboloids (white), prolate spheroids (dark gray), and oblate spheroids (light gray), with the limiting case of paraboloids shown by the thin black line.

The azimuth of the tangent line as a function of inclination and parametric variable is then found from equations (10, 15) to be

$$\sin \phi_T = \frac{b C(t)}{a S(t)} \tan i . \quad (39)$$

Combining equations (8, 38, 39) gives the observer-frame cartesian plane-of-sky coordinates of the tangent line:

$$\begin{aligned} X'_T &= \frac{C(t)}{a \cos i} (a^2 \cos^2 i + \sigma b^2 \sin^2 i) \\ Y'_T &= b S(t) \left( 1 - \frac{b^2 C^2(t)}{a^2 S^2(t)} \tan^2 i \right)^{1/2} \end{aligned} \quad (40)$$

We wish to show that this projected shape is a conic section of the same variety (ellipse or hyperbola) as the one that generated the original quadric. If this were true, then it would be possible to write the plane-of-sky coordinates as

$$\begin{aligned} X'_T &= a' C(t') \\ Y'_T &= b' S(t'). \end{aligned} \quad (41)$$

Comparing equations (40) and (41), we find after some algebra that the two forms for  $(X'_T, Y'_T)$  are indeed consistent, with the equivalences:

$$a' = a f_{Q,i} \cos i \quad (42)$$

$$b' = b \quad (43)$$

$$t' = C^{-1} [f_{Q,i} C(t)] , \quad (44)$$

where for convenience we define the quadric projection factor:

$$f_{Q,i} = \left( 1 + Q \tan^2 i \right)^{1/2} . \quad (45)$$

This demonstrates the original claim that the projected shape is also a conic section, which means that we can re-use the previous equations (31–34) with primed quantities substituted for unprimed ones. From equations (27, 42, 43) it follows that the quadric parameter of the projected shape is

$$Q' = \frac{Q}{f_{Q,i}^2 \cos^2 i} . \quad (46)$$

Finally, we transform the projected reference frame back to be centered on the star again:

$$(x'_T, y'_T) = (X'_T + x'_0, Y'_T) , \quad (47)$$

where the projected quadric displacement  $x'_0$  follows from simple foreshortening:

$$x'_0 = x_0 \cos i . \quad (48)$$

The projection of the apex distance then follows from the primed version of equation (31) as

$$\frac{R'_0}{R_0} = \cos i \left[ 1 + \frac{\Pi}{Q} (f_{Q,i} - 1) \right] \quad (49)$$

and the projected planitude and alatitude can be calculated from equations (32, 34, 42, 46) as

$$\Pi' = \frac{\Pi}{(R'_0/R_0) f_{Q,i} \cos i} \quad (50)$$

$$\Lambda' = (2\Pi' - Q')^{1/2} . \quad (51)$$

These are all shown in Figures 10 and 11 for a variety of quadric parameter  $Q$  (line color) and true planitude  $\Pi$  (line thickness). The projected planitude and alatitude (Fig. 10) behave in a qualitatively

similar fashion. Whatever the true values of  $\Pi$  and  $\Lambda$ , all spheroids ( $Q > 0$ ) tend towards  $\Pi' = 1$  and  $\Lambda' = 1$  as the inclination increases towards  $90^\circ$ . This is because when the spheroid is oriented edge-on, we see its circular cross-section. Hyperboloids behave differently: although  $\Pi'$  and  $\Lambda'$  initially decrease with increasing inclination (for true  $\Pi > 2$ ), they turn around and increase again as  $|i|$  approaches the critical value  $i_{\text{crit}} = 90^\circ - |\theta_Q|$ . For  $|i| > i_{\text{crit}}$  the tangent line does not exist (see § 3.3) because the line of sight is “inside” the asymptotic cone of the far wings (with opening half angle  $\alpha_{\min} = |\theta_Q|$ ), and so no limb-brightened shell would be visible.<sup>5</sup> For paraboloids and spheroids,  $\alpha_{\min} = 0$ , which means that the tangent line exists for all viewing angles.

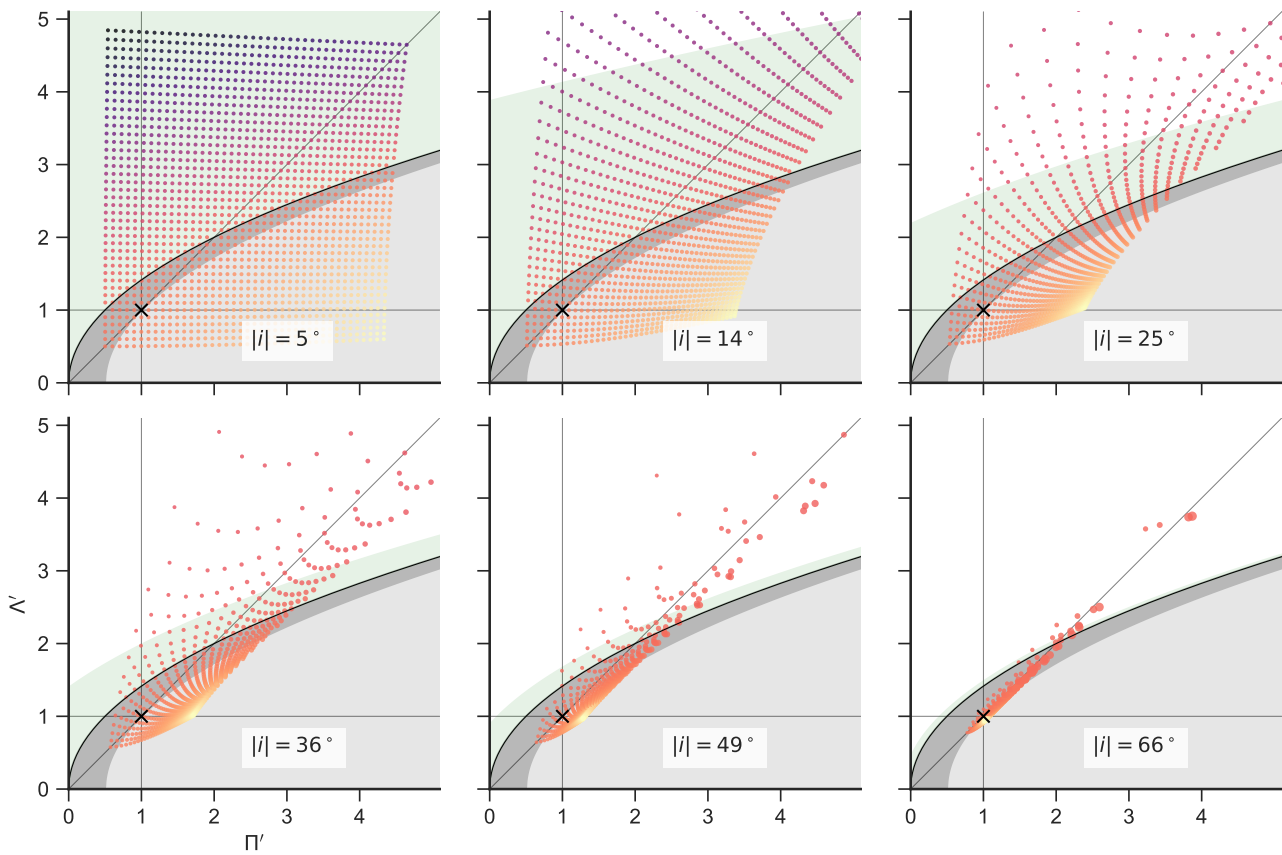
In Figure 11a, we show the inclination-dependent tracks of the quadrics in the diagnostic  $\Pi' - \Lambda'$  plane of projected alatitude versus projected planitude. The true planitude and alatitude, which are seen for an edge-on viewing angle  $i = 0^\circ$ , are marked by filled circles. The zones corresponding to each class of quadric (oblate spheroid, prolate spheroid, or hyperboloid) are marked by gray shading, and it can be seen that the tracks never cross from one zone to another. The convergence of all the spheroid tracks on the point  $(\Pi', \Lambda') = (1, 1)$  is apparent, as is the divergence of the hyperboloid tracks towards  $(\Pi', \Lambda') = (+\infty, +\infty)$  whereas the paraboloids, by contrast, converge on the point  $(\Pi', \Lambda') = (2, 2)$  and the special case of. Two special cases are the confocal paraboloid and the concentric sphere,<sup>6</sup> with true planitude and alatitude  $(\Pi, \Lambda) = (2, 2)$  is the only quadric and  $(1, 1)$ , respectively, which are the only quadrics whose apparent shape remains identical for all inclination angles.

Figure 11b shows how the apparent star-apex separation varies with inclination. For moderate inclinations,  $|i| < 30^\circ$ , this depends primarily on the true planitude  $\Pi$ , with very little influence of the quadric parameter  $Q$ . For  $\Pi > 1$ , the separation increases with  $|i|$ , whereas for  $\Pi < 1$  it decreases slightly. Note, however, that for cases where the projected distance to the source of the external flow,  $D'$ , can be measured, then  $R'_0/D'$  is always an increasing function of  $|i|$ . For larger inclinations,  $|i| > 30^\circ$ , the strands for different  $Q$  begin to separate, with hyperbolae showing the strongest increase of  $R'_0$  with  $|i|$ .

A complementary view of the effects of projection is shown in Figure 12, which shows “snapshots” of  $(\Pi', \Lambda')$  for a sequence of 6 values of the inclination, equally spaced in  $|\sin i|$ , so that each panel is equally likely for an isotropic distribution of orientations. The distribution of the true  $\Pi$  and  $\Lambda$  are each assumed to be uniform on the range  $[0.5, 4.5]$ , giving a uniformly filled square of values for  $|i| = 0$ , which becomes increasingly distorted as  $|i|$  increases. The color scale represents  $Q$  and the symbol size is proportional to  $R'_0/R_0$ . It can be seen that the points tend to cluster closer and closer to the diagonal,  $\Lambda' = \Pi'$ , as the inclination increases, and that the points just below this line tend to have the largest values of  $R'_0/R_0$ . The green shaded region shows the zone of true  $\Lambda, \Pi$  for hyperboloids where the tangent lines still exists for that value of  $|i|$ . This becomes smaller and smaller as  $|i|$  increases, which explains why the hyperboloid zone becomes increasingly depopulated: all quadrics that lay above this region when  $i = 0^\circ$  will no longer be

<sup>5</sup> As illustrated in Figure 8 of Graham et al. (2002), the isophotal emission contours are elliptical in such a case (assuming cylindrical symmetry) and no curved bow shape is apparent. Deviations from cylindrical symmetry can result in a curved emission arc, even for this no-tangent case (Graham et al.’s Fig. 9), but that is beyond the scope of this paper.

<sup>6</sup> So named because the star is at the focus of the parabola or the center of the sphere.



**Figure 12.** Variation with inclination angle of the apparent shape of quadric bows with true planitude and alatitude that are uniformly distributed over the ranges  $\Pi = [0.5, 4.5]$ ,  $\Lambda = [0.5, 4.5]$ . Panels show the apparent  $(\Pi', \Lambda')$  as the inclination is increased through uniform intervals in  $|sin i|$ . Symbol color represents the quadric parameter,  $Q$ , increasing from dark blue, through orange, to yellow. Symbol size is proportional to the increase in apparent star-apex distance,  $R'_0/R_0$ .

visible as a bow for this value of  $|i|$ . Note that this figure is merely illustrative of the qualitative effects of projection, since in reality there is no particular reason to expect a uniform distribution in true  $\Pi$  and  $\Lambda$ .

## 5 THIN-SHELL BOW SHOCK MODELS

More physically realistic examples of bow shapes are provided by steady-state hydrodynamic models for the interaction of hypersonic flows in the thin-shell limit. The classic examples are the solutions for the wind-parallel stream and wind-wind problems (see § 1) of Canto et al. (1996, hereafter CRW), where it is assumed that the two shocks are highly radiative and that the post-shock flows are perfectly mixed to form a single shell of negligible thickness. In this approximation, the shape of the shell is found algebraically by CRW from conservation of linear and angular momentum, following an approach first outlined in Wilkin (1996). For the wind-stream case, the resulting bow shape was dubbed *wilkinoid* by Cox et al. (2012) and has the form:

$$R(\theta) = R_0 \csc \theta (3(1 - \theta \cot \theta))^{1/2}. \quad (52)$$

For the wind-wind case, a family of solutions are found that

depend on the value of  $\beta$ , the wind momentum ratio,<sup>7</sup> see Figure 3, equations (1, 2), and surrounding discussion in § 1. We propose that these shapes be called *cantoids*. The exact solution for the cantoid shapes (eqs. [23, 24] of CRW) is only obtainable in implicit form, but an approximate explicit solution (eq. [26] of CRW) is very accurate for  $\beta \leq 0.1$ . The wilkinoid shape corresponds to the  $\beta \rightarrow 0$  limit of the cantoids. Note that CRW employ cylindrical polar coordinates,  $z$  and  $r$ , see our Figure 3, and we follow this usage for the thin-shell models discussed in this section. CRW's  $z$  axis corresponds to the cartesian  $x$  axis used in sections 3 and 4 of the current paper, while the  $r$  axis corresponds to  $y$  when  $\phi = 0$ .

A generalization of the cantoids to the case of an anisotropic<sup>8</sup> inner wind is developed next, giving rise to what we call *ancantoids*, which depend on an anisotropy index,  $k$ , in addition to  $\beta$ .

### 5.1 Bow shocks from anisotropic wind-wind interactions

We wish to generalize the results of Canto et al. (1996, CRW) to the case where the inner wind is no longer isotropic, but instead has a

<sup>7</sup> By always placing the weaker of the two winds at the origin, it is only necessary to consider  $\beta \leq 1$ .

<sup>8</sup> Note that the wind anisotropy axis must be aligned with the star-star axis to maintain cylindrical symmetry.

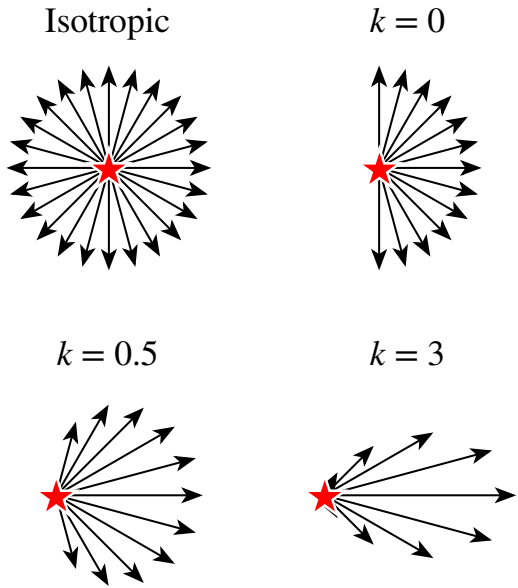


**Figure 13.** Schematic diagram of wind flow patterns in isotropic and non-isotropic cases for different values of the anisotropy index,  $k$ . Arrow length represents the wind momentum loss rate per solid angle.

density that falls off with angle,  $\theta$ , away from the symmetry axis. Specifically, at some fiducial spherical radius,  $R_0$ , from the origin, the wind mass density is given by

$$\rho(R_0, \theta) = \begin{cases} \rho_0 \cos^k \theta & \text{for } \theta \leq 90^\circ \\ 0 & \text{for } \theta > 90^\circ \end{cases}, \quad (53)$$

where  $\rho_0$  is the density on the symmetry axis and  $k \geq 0$  is an *anisotropy index*. The wind velocity is still assumed to be constant and the wind streamlines to be radial, so the radial variation of density at each angle is  $\rho(R, \theta) = \rho(R_0, \theta)(R/R_0)^{-2}$  and the wind mass loss rate and momentum loss rate per solid angle both have the same  $\cos^k \theta$  dependence as the density. Examples are shown in Figure 13 for a variety of different values of  $k$ . As  $k$  increases, the wind becomes increasingly jet-like.

Our primary motivation for considering such an anisotropic wind is the case of the Orion Nebula proplyds and their interaction with the stellar wind of the massive star  $\theta^1$  Ori C (García-Arredondo et al. 2001). The inner “wind” in this case is the transonic photoevaporation flow away from a roughly hemispherical ionization front, where photoionization equilibrium, together with monodirectional illumination of the front, implies that the ionized hydrogen density,  $n$ , satisfies  $n^2 \propto \cos \theta$ , which is equivalent to  $k = 0.5$  in equation (53). Since the primary source of ionizing photons is the same star that is the source of the outer wind, it is natural that the inner wind’s axis should be aligned with the star–star axis in this case. For other potential causes of wind anisotropy (for instance, bipolar flow from an accretion disk), there is no particular reason for the axes to be aligned, so cylindrical symmetry would be broken. Nevertheless, we calculate results for general  $k$  with aligned axes, so as to provide a richer variety of cylindrically symmetric bow shock shapes than are seen in the cantoids.

The general solution for the bow shock shape,  $R(\theta)$ , in the CRW

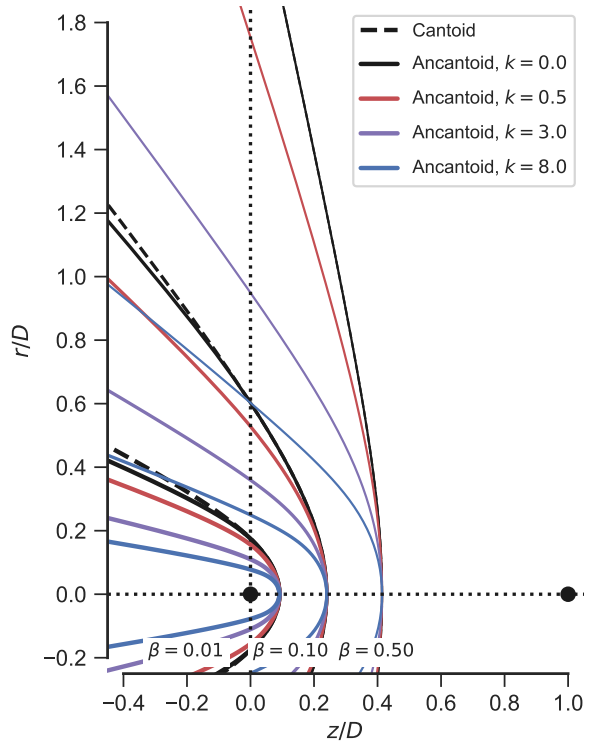


**Figure 14.** Bow shock shapes for interacting winds in the thin-shell approximation: cantoids and ancantoids. Coordinates are normalized by  $D$ , the distance between the two wind sources, which are indicated by black dots on the axis. The weaker source is at  $(0, 0, 0)$  and the stronger source is at  $(1, 0, 0)$ . Results are shown for different values of the wind momentum ratio,  $\beta$  (different line widths), and for the case where the weaker wind is isotropic (black lines) or anisotropic (colored lines).

formalism is

$$R(\theta) = \frac{j_w + j_{w1}}{(\dot{\Pi}_{wr} + \dot{\Pi}_{wr1}) \cos \theta - (\dot{\Pi}_{wz} + \dot{\Pi}_{wz1}) \sin \theta} \quad (54)$$

where  $\dot{\Pi}_{wr}$ ,  $\dot{\Pi}_{wz}$ ,  $j_w$  are the accumulated linear radial momentum, linear axial momentum, and angular momentum, respectively, due to the inner wind emitted between the axis and  $\theta$ . The equivalent quantities for the outer wind have subscripts appended with “1”. The inner wind momenta for our anisotropic case (replacing CRW’s eqs. [9, 10]) are:

$$\begin{aligned} \dot{\Pi}_{wz} &= \frac{k+1}{2(k+2)} \dot{M}_w^0 V_w \max \left[ (1 - \cos^{k+2} \theta), 1 \right] \\ \dot{\Pi}_{wr} &= (k+1) \dot{M}_w^0 V_w I_k(\theta) \end{aligned} \quad (55)$$

where

$$\dot{M}_w^0 = \frac{2\pi}{k+1} r_0^2 \rho_0 V_w \quad (56)$$

is the total mass-loss rate of the inner wind. The integral

$$I_k(\theta) = \int_0^{\max(\theta, \pi/2)} \cos^k \theta \sin^2 \theta d\theta \quad (57)$$

has an analytic solution in terms of the hypergeometric function,  ${}_2F_1(-\frac{1}{2}; \frac{1+k}{2}; \frac{3+k}{2}; \cos^2 \theta)$ , but is more straightforwardly calculated by numerical quadrature. The angular momentum of the inner wind

1  
2  
3  
4 12 Tarango-Yong & Henney  
5  
6  
7  
8  
9  
10  
11  
12  
13  
14  
15  
16  
17  
18  
19  
20  
21  
22  
23  
24  
25  
26

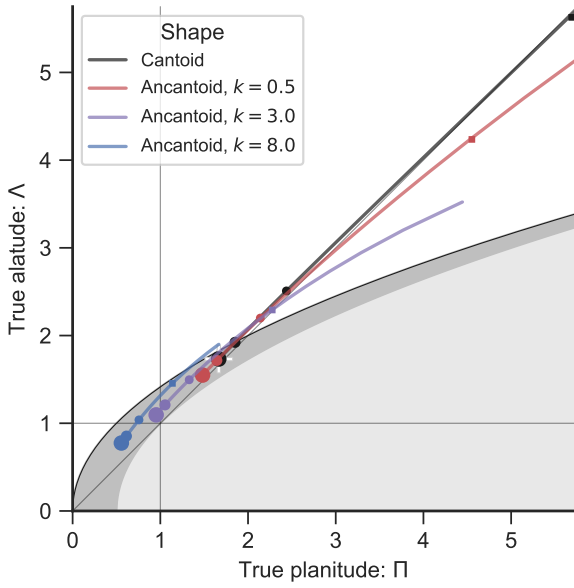


**Figure 15.** True shapes of cantoids and ancantoids in the  $\Pi-\Lambda$  plane, calculated according to results of App. D. For each line,  $\beta$  varies over the range  $[0, 1]$  from lower left to upper right (although the black and red lines are truncated on the upper right), and line colors correspond to different anisotropy indices, matching those used in Fig. 14. Circle symbols mark particular  $\beta$  values: 0, 0.01, 0.1, from largest to smallest circle. Square symbols mark  $\beta = 0.5$ , but with  $\Lambda$  calculated exactly, instead of using the approximation of equation (D14). The white plus symbol marks the result for the wilkinoid:  $(\Pi, \Lambda) = (\frac{5}{3}, \sqrt{3})$ . Background shading indicates the domains of different quadric classes: hyperboloids (white), prolate spheroids (dark gray), and oblate spheroids (light gray).

about the origin is  $j_w = 0$  because it is purely radial. The outer wind momenta are unchanged from the CRW case, but are given here for completeness:

$$\begin{aligned} \dot{\Pi}_{wz1} &= -\frac{\dot{M}_{w1}^0 V_{w1}}{4} \sin^2 \theta_1 \\ \dot{\Pi}_{wr1} &= \frac{\dot{M}_{w1}^0 V_{w1}}{4} (\theta_1 - \sin \theta_1 \cos \theta_1) \\ j_{w1} &= \frac{\dot{M}_{w1}^0 V_{w1}}{4} (\theta_1 - \sin \theta_1 \cos \theta_1) D. \end{aligned} \quad (58)$$

We define  $\beta$  in this case as the momentum ratio *on the symmetry axis*, which means that

$$\dot{M}_{w1}^0 V_{w1} = 2(k+1)\beta \dot{M}_w^0 V_w. \quad (59)$$

Substituting equations (55–59) into equation (54) and making use of the geometric relation between the interior angles of the triangle shown in Figure 3:

$$R \sin(\theta + \theta_1) = D \sin \theta_1, \quad (60)$$

yields

$$\theta_1 \cot \theta_1 = 1 + 2\beta \left( I_k(\theta) \cot \theta - \frac{1 - \cos^{k+2} \theta}{k+2} \right), \quad (61)$$

which is the generalization of CRW's equation (24) to the anisotropic case. Equation (61) is solved numerically to give  $\theta_1(\theta)$ , which is then combined with equations (60) and (1) to give the dimensionless

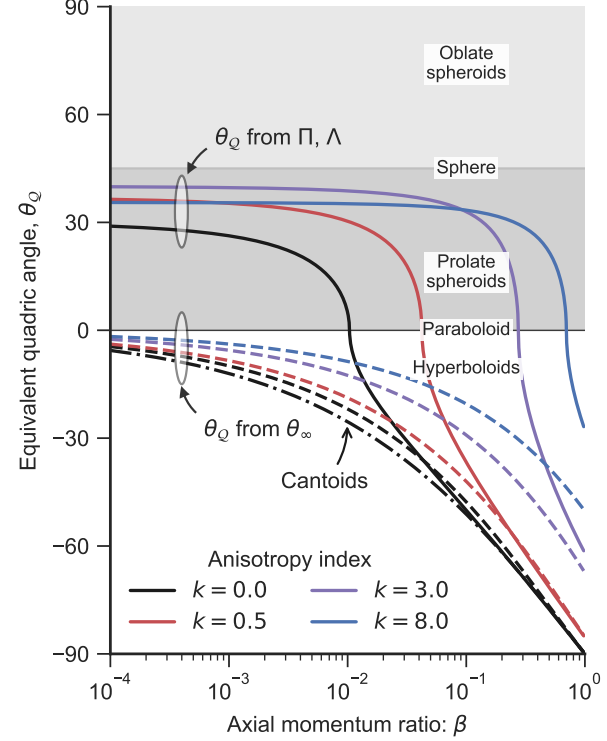


**Figure 16.** Equivalent quadric angles,  $\theta_Q$ , for ancantoids and cantoids. Solid lines show values of  $\theta_Q$  calculated from  $(\Pi, \Lambda)$ , which is representative of the shape of the head, while dashed lines show  $\theta_Q$  calculated from  $\theta_\infty$ , which is representative of the tail. Dot-dashed line shows the result for cantoids, which differ from the  $k = 0$  ancantoids in  $\theta_\infty$ , but not in  $(\Pi, \Lambda)$ . Gray shading and line colors have the same meaning as in Fig. 15.

bow shape,  $R(\theta; \beta, k)/R_0$ , where we now explicitly indicate the dependence of the solution on two parameters: axial momentum ratio,  $\beta$ , and anisotropy index,  $k$ . We refer to the resultant bow shapes as *ancantoids*.

## 5.2 True shapes of cantoids and ancantoids

The shapes of the ancantoid bow shocks are shown in Figure 14 for three different values of  $\beta$ , and are compared with the CRW results for cantoids (dashed curves). The location of these shapes in the planitude–alatitude plane is shown in Figure 15, where the gray background shading indicates the zones of different quadric classes, as in § 4, Figures 11 and 12. Values of  $\Pi$  and  $\Lambda$  are calculated via the analytic expressions derived in Appendix D1 and D2, respectively, which are only approximate in the case of  $\Lambda$ . However, the filled square symbols show the exact results for  $\beta = 0.5$ , which can be seen to lie extremely close to the approximate results, even for the worst case of  $k = 0$ . The leading term in the relative error of equation (D14) scales as  $(\beta/(k+2))^2$ , so the approximation is even better for smaller  $\beta$  and larger  $k$ .

It is apparent from Figure 14 that the  $k = 0$  ancantoid is identical to the cantoid for  $\theta \leq 90^\circ$  ( $z > 0$ , to the right of vertical dotted line

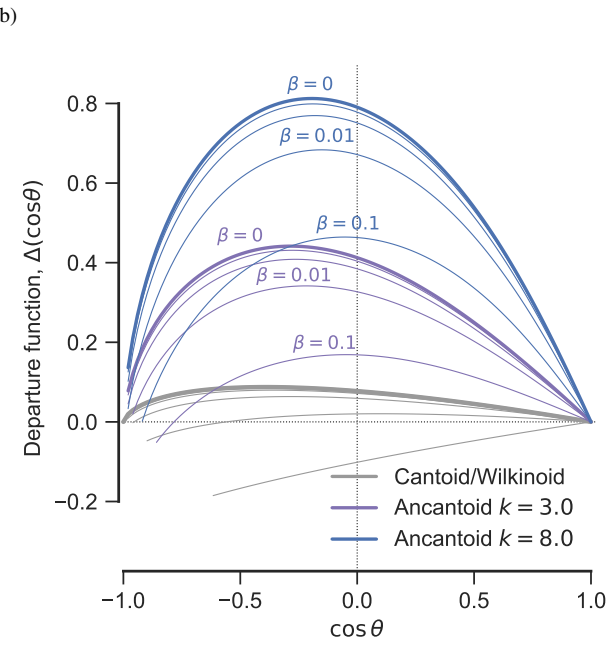
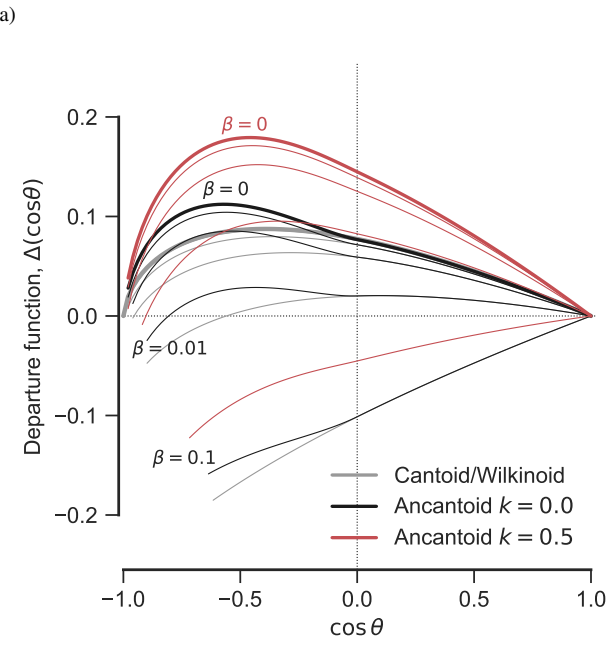


**Figure 17.** Parabolic departure function,  $\Delta(\cos\theta)$ , for ancantoids and cantoids. Heavy lines show the  $\beta = 0$  parallel stream case (Wilkinoid in the isotropic case). Light lines show increasing values of  $\beta = 10^{-4}, 0.001, 0.01, 0.1$ , as marked. (a) Cantoids (gray) and moderately anisotropic ancantoids: hemispheric,  $k = 0$  (black), and proplyd-like,  $k = 0.5$  (red). (b) Cantoids (gray) and extremely anisotropic, jet-like ancantoids:  $k = 3$  (purple) and  $k = 8$  (blue).

in Fig. 14), but is slightly more swept back in the far wings.<sup>9</sup> Since the true planitude and alatitude depend on  $R(\theta)$  only in the range  $\theta = [0, 90^\circ]$ , the cantoid and the  $k = 0$  ancantoid behave identically

<sup>9</sup> Due to the discontinuity in the inner wind density at  $\theta = 90^\circ$  (see Fig. 13), there is a discontinuity in the second derivative of the bow shape.

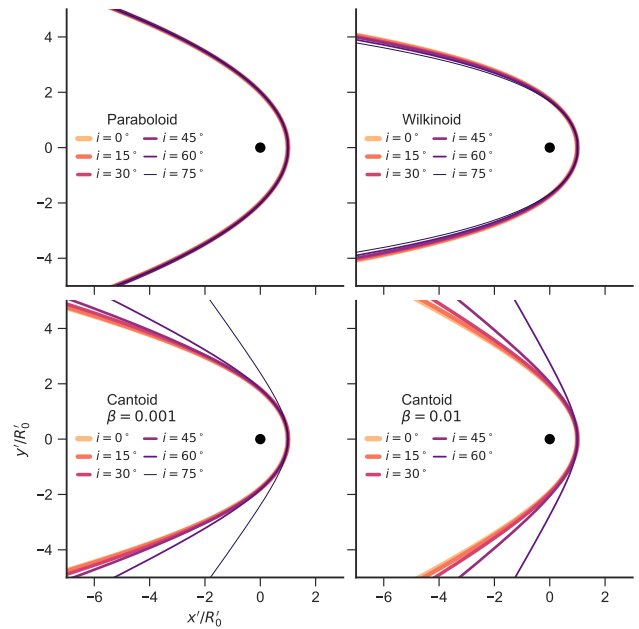


**Figure 18.** Apparent bow shapes as a function of inclination angle for isotropic thin shell models. (a) Confocal paraboloid for comparison (shape independent of inclination). (b) Wilkinoid. (c) Cantoid,  $\beta = 0.001$ . (d) Cantoid,  $\beta = 0.01$ .

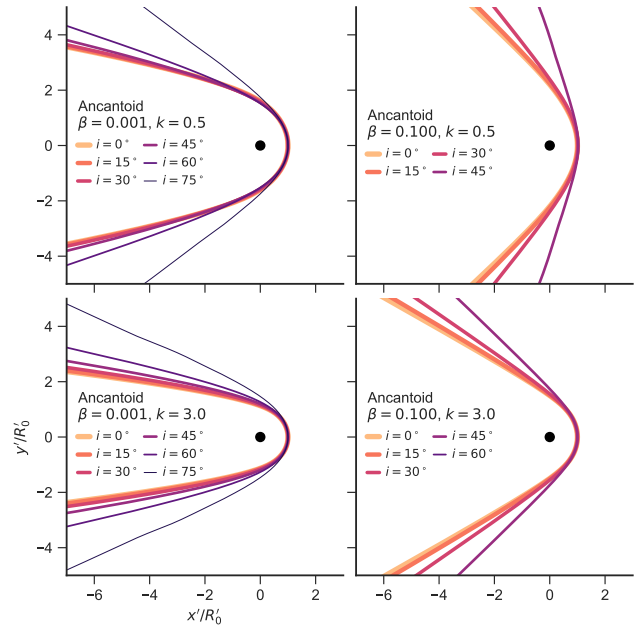


**Figure 19.** Further apparent bow shapes as a function of inclination angle for anisotropic thin shell models (ancantoids). (a)  $\beta = 0.001, k = 0.5$ ; (b) (a)  $\beta = 0.1, k = 0.5$ ; (c)  $\beta = 0.001 k = 3$ ; (d)  $\beta = 0.1 k = 3$ .

in Figure 15. There is a general tendency for the bows to be flatter and more open with increasing  $\beta$  and decreasing  $k$ , with the cantoid being most open at a given  $\beta$ . All the models cluster close to the diagonal  $\Lambda \approx \Pi$  in the planitude–alatitude plane, but with a tendency for  $\Lambda > \Pi$  at higher anisotropy. There is therefore a degeneracy between  $\beta$  and  $k$  for higher values of  $\beta$ . The wilkinoid shape, which

## 14 Tarango-Yong & Henney

5 corresponds to the  $\beta \rightarrow 0$  limit of the cantoids, is marked by a white  
 6 plus symbol in Figure 15, and lies in the prolate spheroid region of  
 7 the plane. Cantoids lie either in the prolate spheroid or hyperboloid  
 8 regions, according to whether  $\beta$  is less than or greater than about  
 9 0.01. For ancantoids of increasing  $k$ , this dividing point moves to  
 10 higher values of  $\beta$ , until almost the entire range of models with  
 11  $k = 8$  are within the prolate spheroid zone.

12 However, the true planitude and alatitude, which are what would  
 13 be observed for a side-on viewing angle ( $i = 0$ ), are not at all  
 14 sensitive to the behavior of the far wings of the bow shock, which  
 15 has a rather different implication as to which variety of quadric  
 16 best approximates each shape. We illustrate this in Figure 16, which  
 17 shows two different ways of estimating the quadric angle,  $\theta_Q$  (see  
 18 § 4). The first is from  $(\Pi, \Lambda)$ , as in Figure 15:

$$\theta_Q^{\text{head}} = \text{sgn}(2\Pi - \Lambda^2) \tan^{-1} |2\Pi - \Lambda^2|^{1/2}, \quad (62)$$

19 which follows from equations (27), (28), and (34). The second is  
 20 from the asymptotic opening angle of the wings,  $\theta_\infty$  (Fig. 4):

$$\theta_Q^{\text{tail}} = \theta_\infty - 180^\circ, \quad (63)$$

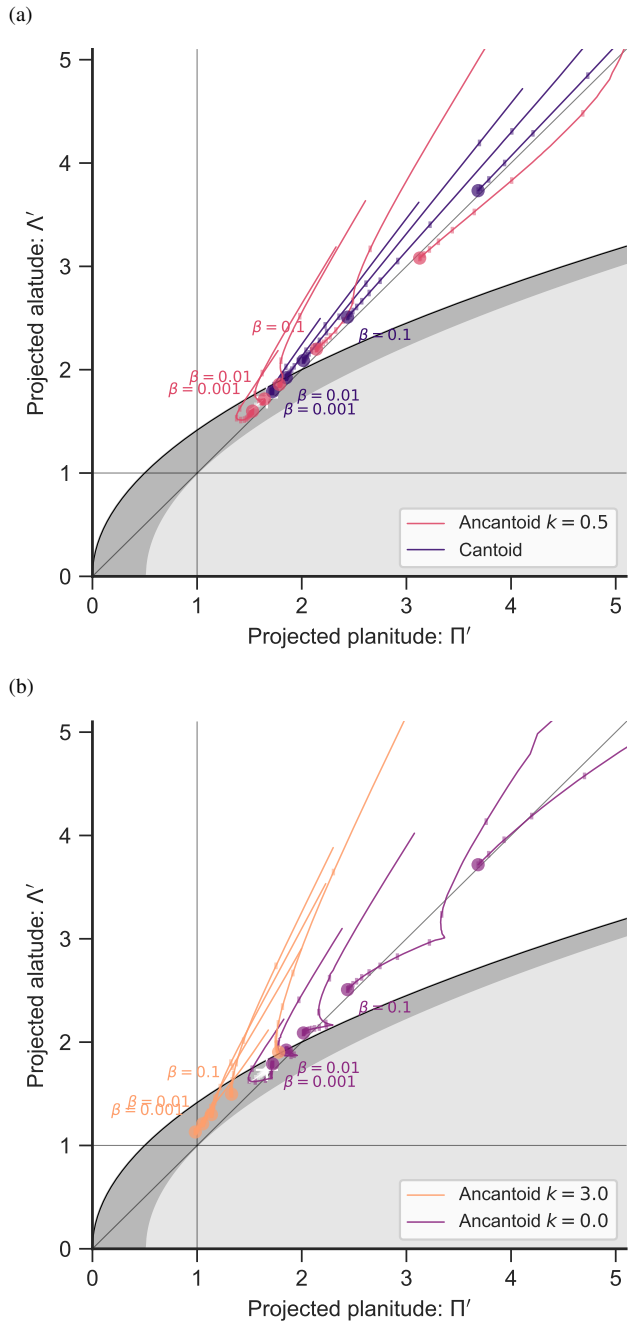
21 where  $\theta_\infty$  is calculated from equation (D17) for ancantoids, or (D19)  
 22 for cantoids. If the bow shock shape were truly a quadric, then these  
 23 two definitions would agree. However, as seen in Figure 16, this is  
 24 not the case for the cantoids and ancantoids. While  $\theta_Q^{\text{head}}$  generally  
 25 corresponds to a prolate spheroid (except for the largest values of  
 26  $\beta$ ),  $\theta_Q^{\text{tail}}$  always corresponds to a hyperbola. This tension between  
 27 the shape of the head and the shape of the far wings has important  
 28 implications for the projected shapes (as we will see in the next  
 29 section), since the far wings influence the projected planitude and  
 30 alatitude when the inclination is large.

31 Figure 17 shows the parabolic departure function (see § 4.1)  
 32 for the thin-shell models. This provides an alternative perspective  
 33 on the resultant bow shapes, with two different types of behavior  
 34 being apparent. Models with high  $\beta$  and low anisotropy behave  
 35 similarly to the hyperboloids, such as the  $(\Pi, \Lambda) = (3/2, 8/3)$ ,  $(2, 8/3)$ ,  
 36  $(8/3, 8/3)$ , and  $(3/2, 2)$  cases from Figure 9. This is the case for the  
 37  $\beta \geq 0.01$  models in Figure 17a, which all show departure functions  
 38 that become negative in the far wings (more open than parabola) and  
 39 terminate at a  $\theta_\infty < 180^\circ$ . The second type of behavior is shown by  
 40 models with low  $\beta$  or high anisotropy, which behave like spheroids  
 41 for positive and mildly negative values of  $\cos \theta$ , but, unlike the  
 42 spheroids, all tend towards  $\Delta = 0$  in the far tail as  $\cos \theta \rightarrow -1$ .

### 46 5.3 Apparent shapes of projected cantoids and ancantoids

47 Figures 18 and 19 show the apparent bow shapes of various thin shell  
 48 models (wilkinoid, cantoids, ancantoids)<sup>10</sup> for different inclination  
 49 angles  $|i|$ . For comparison, Figure 18a shows the confocal paraboloid,  
 50 whose apparent shape is independent of inclination (see Appendix C).  
 51 The wilkinoid (Fig. 18b) shows only subtle changes, with the wings  
 52 becoming slightly more swept back as the inclination increases.  
 53 The cantoids (Fig. 18c and d) behave in the opposite way, with  
 54 the wings becoming markedly more open once  $|i|$  exceeds  $60^\circ$  (for  
 55  $\beta = 0.001$ ), or  $45^\circ$  (for  $\beta = 0.01$ ). The ancantoids (Fig. 19) can show  
 56 more complex behavior. For instance, in the  $k = 0.5$ ,  $\beta = 0.001$   
 57 ancantoid (Fig. 19a) the near wings begin to become more closed

10 See also previous studies of the projected shape of the wilkinoid (Wilkin 1997; Cox et al. 2012; Ng et al. 2017) and the cantoids (Roberto et al. 2005).



58 **Figure 20.** Apparent projected shapes of wilkinoid, cantoids and ancantoids in  
 59 the  $\Pi'$ - $\Lambda'$  plane. Colored symbols indicate the  $|i| = 0$  position for  $\beta = 0.001$ ,  
 60 0.003, 0.01, 0.03, 0.1, 0.3. Thin lines show the inclination-dependent tracks  
 61 of each model, with tick marks along each track for 20 equal-spaced values  
 62 of  $|\sin i|$ . Gray shaded regions are as in Fig. 11a. The wilkinoid track is  
 63 shown in white. (a) Isotropic wind model (cantoid) and proplyd-like model  
 64 (ancantoid,  $k = 0.5$ ). (b) Hemispheric wind model (ancantoid,  $k = 0$ ) and  
 65 jet-like model (ancantoid,  $k = 3$ ).

66 with increasing inclination up to  $|i| = 60^\circ$ , at which point they open  
 67 up again, whereas the opening angle of the far wings increases  
 68 monotonically with  $|i|$ .

69 The inclination-dependent tracks that are traced by the thin-  
 70 shell models in the projected planitude–alatitude plane are shown in  
 71 Figure 20. The behavior is qualitatively different from the quadric

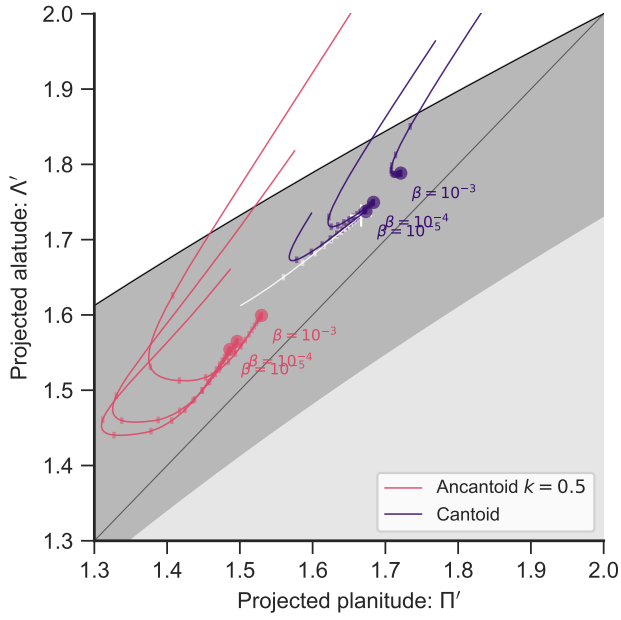


**Figure 21.** As Fig. 20a but zoomed in to show the wilkinoid track (white) and the convergence of the cantoid tracks (purple) to the wilkinoid as  $\beta \rightarrow 0$ .

shapes shown in Figure 11a in that the tracks are no longer confined within the borders of the region of a single type of quadric (hyperboloid or spheroid). At low inclinations, many of the models behave like the prolate spheroids, but then transition to a hyperboloid behavior at higher inclinations, which is due to the tension between the shape of the head and the shape of the far wings, as discussed in the previous section. This can be seen most clearly in the  $\beta = 0.001$ ,  $k = 0.5$  ancantoid (lowest red line in Fig. 20a, see also zoomed version in Fig. 21). The track begins heading towards  $(\Pi', \Gamma') = (1, 1)$ , as expected for a spheroid, but then turns around and crosses the paraboloid line to head out on a hyperboloid-like track.

Ancantoids with different degrees of inner-wind anisotropy are shown in Figure 20b. In all cases, the tracks follow hyperboloid-like behavior at high inclinations, tending to populate the region just above the diagonal  $\Lambda' = \Pi'$ . The  $k = 0$  ancantoids show a kink in their tracks at the point where the projected apex passes through  $\theta = 90^\circ$ , due to the discontinuity in the second derivative of  $R(\theta)$  there (see footnote 9). The wilkinoid has a much less interesting track, most clearly seen in the zoomed Figure 21, simply moving the short distance from  $(5/3, \sqrt{3})$  to  $(3/2, \sqrt{8/3})$ . Despite its location in the ellipsoid region of the plane, the fact that it has  $\theta_\infty = 180^\circ$  means that it behaves more like a parabola at high inclination, but converges on  $(3/2, \sqrt{8/3})$  instead of  $(2, 2)$  since the far wings are asymptotically cubic, rather than quadratic.

The local density of tick marks gives an indication of how likely it would be to observe each portion of the track, assuming an isotropic distribution of viewing angles. It can be seen that the ticks tend to be concentrated towards the beginning of each track, near the  $|i| = 0$  point, so the hyperboloid-like portions of the tracks would be observed for only a relatively narrow range of inclinations. This concentration becomes more marked as  $\beta$  becomes smaller, which helps to resolve the apparent paradox that the wilkinoid corresponds to the  $\beta \rightarrow 0$  limit of the cantoids, and yet follows a qualitatively different track. The detailed behavior of the small- $\beta$  cantoid models is shown in Figure 21, which zooms in on the region around the

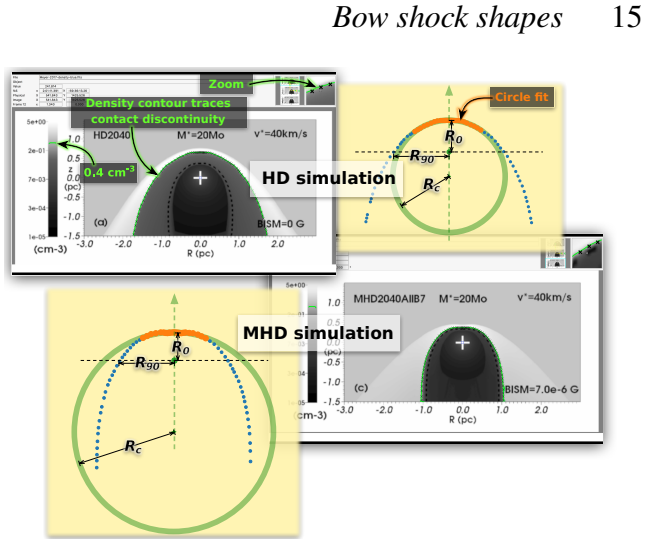


**Figure 22.** Procedure for tracing the contact discontinuity from the Meyer et al. (2017) simulations. The density maps from Meyer et al.'s Fig. 3 are converted to FITS format and displayed using the software SAOImage DS9 (Joye & Mandel 2003). The density contour at  $0.4 \text{ cm}^{-3}$  is displayed (shown in green in the figure) and this is traced by hand by placing “point regions” on the image (shown by black “x” shapes in the figure). The zoom facility of the software allows the points to be placed with any required accuracy. The points are saved to a file in the DS9 region file format, which is then read by Python programs for further processing. For example, the yellow boxes show circle fits and determination of the parameters  $R_0$ ,  $R_c$ , and  $R_{90}$ . In this example, only the points shown in orange (within  $60^\circ$  of axis) are used in the fits.

wilkinoid track. It can be seen that for  $\beta < 0.001$  the cantoid tracks begin to develop a downward hook, similar to the  $k = 0.5$  ancantoids discussed above. For  $\beta < 10^{-4}$  this begins to approach the wilkinoid track and the high inclination, upward portion of the track becomes less and less important as  $\beta$  decreases.

## 6 MORE REALISTIC BOW SHOCK MODELS

The assumptions underlying the models of the previous section may break down in various ways. To test whether the planitude–alatitude analysis is still useful in less “ideal” situations, we here apply it to more realistic simulations of stellar bow shocks. We choose a pair of hydromagnetic (HD) and magnetohydrodynamic (MHD) moving-star simulations from Meyer et al. (2017), in which the only difference is the presence (MHD case) or absence (HD case) of an ambient magnetic field with strength  $B = 7 \mu\text{G}$ , oriented parallel to the stellar velocity. In each case, the inner wind comes from a  $20 M_\odot$  main-sequence star, with mass loss rate and terminal velocity that are roughly constant with time at  $\dot{M}_w \approx 4 \times 10^{-7} M_\odot \text{ yr}^{-1}$  and  $V_w \approx 1200 \text{ km s}^{-1}$ , while the outer wind is a parallel stream due to the star's own motion at  $40 \text{ km s}^{-1}$  through a uniform medium of density  $0.57 \text{ cm}^{-3}$ .

For these parameters, the radiative cooling distance for shocked ambient gas in the bow is a significant fraction ( $\approx 10\%$ ) of the bow shock size,  $R_0$ , tending to increase towards the wings, and the radiative cooling in the shocked stellar wind is even less efficient. This represents a ~~green~~ significant violation of the assumptions behind the thin-shell models, since the total shocked shell thickness is of the same order as  $R_0$ . The parabolic departure function (sec. § 4.1) for the shape of the contact-discontinuity. Nevertheless, the emissivity of several observationally

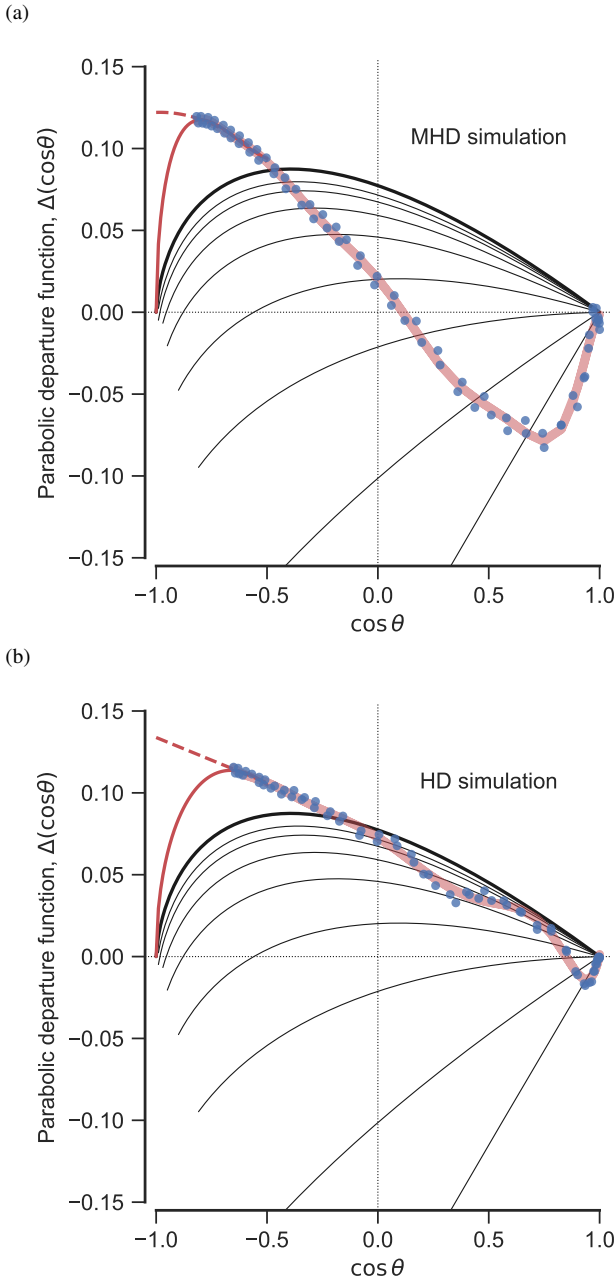


**Figure 23.** Departure function for the shape of the contact discontinuity, measured from two numerical simulations of a  $20 M_{\odot}$  main-sequence star, moving at  $40 \text{ km s}^{-1}$  through a uniform medium of density  $0.57 \text{ cm}^{-3}$  (Meyer et al. 2017). (a) Magnetohydrodynamic simulation with ambient magnetic field of strength  $7 \mu\text{G}$ , oriented parallel to the stellar velocity. (b) Hydrodynamic simulation with zero magnetic field. Blue dots show the measured shape, while the thick, pale-red line shows a 12th-order Chebyshev polynomial fit. The published shapes only extend to  $\theta \approx 130\text{--}150^\circ$ , so we extrapolate the shapes out to  $\theta = 180^\circ$ . Two different extrapolations are shown, corresponding to bows that are asymptotically closed (dashed red line) or open (solid red line). For comparison, black lines show the departure function for wilkinoid (thick line) and cantoids (thin lines).

important emission processes, such as mid-infrared thermal dust emission and the optical H $\alpha$  emission line, is concentrated near the contact discontinuity<sup>11</sup> so it is reasonable to use this surface as a first approximation for the shape of the bow.

We have traced the contact discontinuity in the two models, shown using the procedure outlined in Figure 22, and show results for the parabolic departure function (see § 4.1) as blue symbols in Figure 23. The MHD simulation shows a strongly negative dip in the departure function close to the apex ( $\cos\theta = 1$ ), indicating a very flat shape.<sup>12</sup> The HD simulation shows only a small negative dip in the departure function at the apex, but otherwise approximately follows the wilkinoid curve in the forward hemisphere. In both cases the departure function is more positive than the wilkinoid in the far wings ( $\cos\theta < -0.5$ ), but we do not have data for the full range of  $\theta$ , and so two different extrapolations for  $\theta \rightarrow 180^\circ$  are shown. In the first (dashed red line in figure), we fit a low-order polynomial of  $\cos\theta$  to the points with  $\cos\theta < -0.5$  and extend it to  $\cos\theta = -1$ , which gives an asymptotically closed shape. In the second extrapolation (solid red line in figure), we fit a polynomial that is multiplied by  $(1 + \cos\theta)^{1/2}$ , which forces the departure function to zero at  $\cos\theta = -1$ , giving an asymptotically open shape, as with the wilkinoid. In a true steady state, the far wings should be asymptotically open, but as  $\theta \rightarrow 180^\circ$  the flow times become longer and longer, so that a bow shock with a finite age will be closed.

Using a 12th-order Chebyshev fit to the traced shapes, we show the apparent shape of the contact discontinuity at a series of inclination angles,  $|i|$ , in Figure 24. The four panels show the two simulations for each of the two far-wing extrapolations. Comparison with Figures 18 and 19 shows the general tendency is the same as with the wilkinoid: that the apex becomes less flat and the wings less open as the inclination angle is increased. There is no sign of the sudden increase in openness at high inclination, as seen in the cantoids and ancantoids that are asymptotically hyperbolic. On the other hand, the projected shapes of both simulations vary much more strongly with  $|i|$  than the wilkinoid does. For the HD simulation, this is mainly apparent for  $|i| > 30^\circ$ , but for the MHD simulation it occurs at all inclinations.

The resultant inclination-dependent tracks in the planitude–alatitude plane are shown in Figure 25. These are compared with measurements<sup>13</sup> from post-processed infrared dust continuum maps at  $60 \mu\text{m}$  (§ 4.3 of Meyer et al. 2017), shown by open square symbols

<sup>11</sup> Note that, in the non-magnetic HD models, efficient thermal conduction leads to a thick layer of hot, thermally evaporated ambient material that separates the shocked stellar wind from the cool, dense shell of shocked ambient gas (see § 3.3 of Meyer et al. 2014). In this case, the contact discontinuity is taken to be the boundary between hot and cold ambient gas, as opposed to the *material discontinuity* between shocked ambient gas and shocked wind gas. In the MHD models, the thermal conduction is almost completely suppressed, so that the material and contact discontinuities coincide.

<sup>12</sup> Measured from Figure 3 of Meyer et al. (2017) by tracing the  $0.4 \text{ cm}^{-3}$  density contour.

<sup>13</sup> Meyer et al. (2017) speculate that this flatness may be the signature of the formation of a complex multiple-shock topology at the apex (de Sterck & Poedts 1999). For our purposes, the reason does not matter, merely that the magnetic and non-magnetic models predict markedly different shapes.

<sup>14</sup> The shape measurements were performed by converting to contours the  $60 \mu\text{m}$  images in Meyer et al. (2017)’s Fig. 10 and then tracing the ridge of minimum radius of curvature of the contours. Identical results are found from using the  $100 \mu\text{m}$  maps instead. For the  $25 \mu\text{m}$  maps, although the same results are found for low inclinations, in the maps with  $|i| \geq 45^\circ$  in the HD case it becomes impossible to trace the limb-brightened rim because it becomes fainter than the emission from the true apex of the bow.

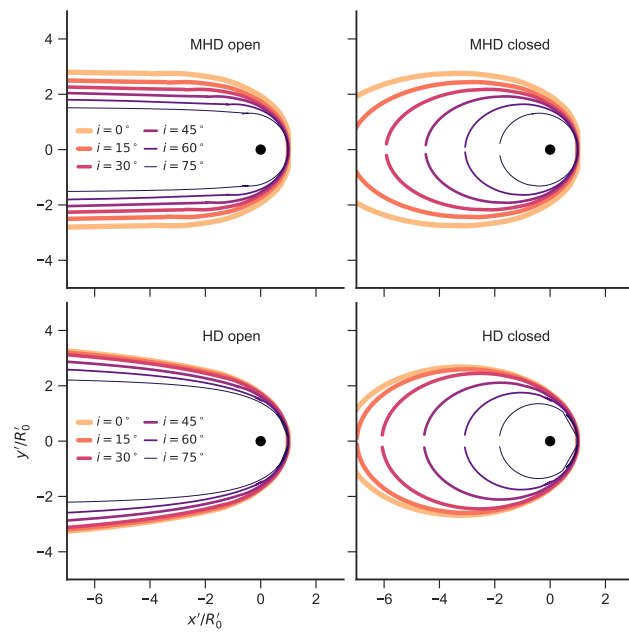


**Figure 24.** Projected shapes of contact discontinuity from simulations at different inclinations  $|i|$  (varying line color and thickness, see key). Top row shows magnetized simulation of Fig. 23a, bottom row shows non-magnetized simulation of Fig. 23b. Left column shows asymptotically open extrapolation, right column shows asymptotically closed extrapolation. All shapes are normalized to the projected apex distance,  $R'_0$

for  $i = 30^\circ, 45^\circ$ , and  $60^\circ$ . The agreement between the two is good. In particular, the  $60\text{ }\mu\text{m}$ -derived shapes are always very close to the tracks derived from the contact discontinuity shape. Also, the ordering of the three inclinations along the tracks corresponds to what is predicted, although quantitatively there are some slight deviations. This close agreement stems from the fact, emphasized by Meyer et al. (2014), that the long-wavelength dust emission from hot-star bow shocks tends to be dominated by material just outside the contact discontinuity. Note that there is almost no difference in the planitude–alatitude tracks between the closed and open extrapolations. This is because  $\Pi'$  and  $\Lambda'$  only depend on the portion of  $R(\theta)$  between  $\theta_0$  (eq. [18]) and  $\theta_{90}$  (eq. [21]), and these are both smaller than the  $\theta$  range where extrapolation is necessary, except for in the HD case at the highest inclinations.

Figure 26 shows the inclination dependence of the projected apex distance,  $R'_0$ . As in the previous figure, the lines show the prediction based on the shape of the contact discontinuity, while the square symbols show the results from the  $60\text{ }\mu\text{m}$  dust continuum maps.<sup>14</sup> In addition, triangle symbols show results from  $\text{H}\alpha$  optical

<sup>14</sup> There is an apparent error in the spatial scales for the HD simulations in Figs. 10 and 11 of Meyer et al. (2017), with the dust emission peaks occurring at radii that are clearly too large. The stated apex distance for the contact discontinuity in this simulation is  $0.69\text{ pc}$  from Table 2 of Meyer et al. (2014), and the position of the peak in dust column density is  $0.70\text{ pc}$  from Fig. 17a of Meyer et al. (2014). These are consistent with Figs. 3, 4, and 7 of Meyer et al. (2017), but not with Figs. 10 and 11. Luckily, the position of the true apex is clearly visible in the  $25\text{ }\mu\text{m}$  maps of Fig. 10 at inclinations of  $45^\circ$  and  $60^\circ$ . The projected separation of the true apex is  $R_0 \cos i$ , independent of the bow shape, which allows a correction factor of 0.65 to be found, assuming that the on-axis peak in the  $25\text{ }\mu\text{m}$  emission coincides with the peak in dust

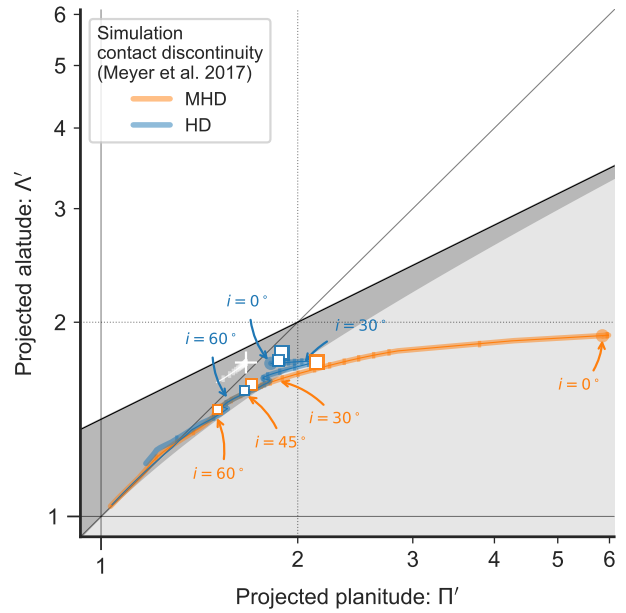


**Figure 25.** Apparent projected shapes of simulations in the  $\Pi'$ – $\Lambda'$  plane. Thick solid lines show the predicted inclination-dependent tracks of the traced contact discontinuity shape for the asymptotically open extrapolation, with tick marks indicating 20 equal intervals in  $|\sin i|$ . Thin solid lines show the same for the asymptotically closed extrapolation, which only deviates from the open case at the high- $|i|$  end of the HD tracks. The true planitude and alatitude are marked by filled circle symbols. Open square symbols show the shapes traced from the dust emission maps at  $60\text{ }\mu\text{m}$  for inclinations of (largest to smallest)  $30^\circ, 45^\circ$ , and  $60^\circ$ . For comparison, the wilkinoid track is shown in white. Note that the scales of both axes are logarithmic in this case.

emission line maps, which are given for  $i = 0$  in Fig. 7 of Meyer et al. (2017). Again, the agreement is good between the values derived from the shape of the contact discontinuity and those derived from the surface brightness maps. The greatest discrepancy is seen with the  $\text{H}\alpha$  maps and the intermediate inclination dust maps, with  $R'_0$  being overestimated by a few percent in both cases. The differences in behavior between the two simulations are much larger than this. The larger true planitude of the MHD simulation means that the relative increase of  $R'_0$  with  $|i|$  is much stronger than in the HD simulation for  $|i| < 45^\circ$ , as expected from Figure 10b.

The probability densities<sup>15</sup> of the apparent shape and size of the simulation bows (measured at the contact discontinuity) are shown in Figure 27, assuming that the viewing direction is uniformly distributed in solid angle. The modal value of the projected planitude is similar at  $\Pi' \approx 1.8$  for both simulations, but the distribution is much broader in the MHD case, which has a low-level wing extending out to  $\Pi' \approx 6$ . The projected alatitude distributions are both narrower than the planitude (note the different scale of the histogram axis), with the MHD case again being the broader of the two and peaking at a slightly lower value ( $\Lambda' \approx 1.7$  as opposed to  $\approx 1.8$  for

column density. This correction has been applied to the blue square symbols shown in our Fig. 26.

<sup>15</sup> The probability density is defined so that its integral over the full range of the histogrammed variable is unity, making it independent of the histogram bin widths. This means that the characteristic width of an approximately unimodal distribution is one over the maximum probability density.

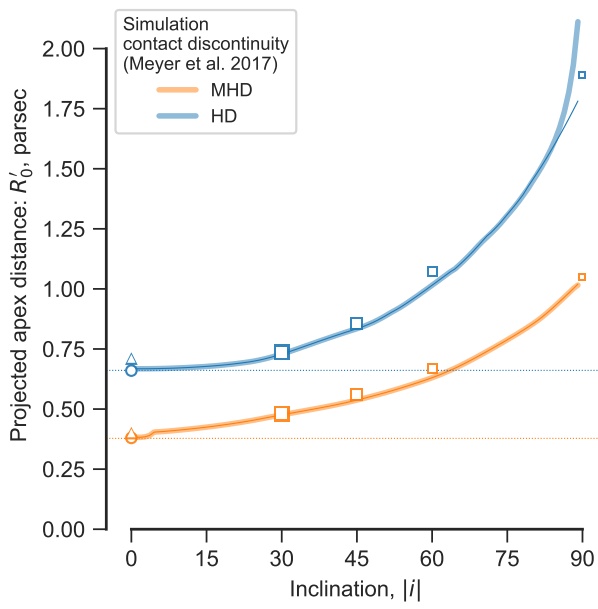


**Figure 26.** Apparent projected apex distance of simulations. Line and symbol meanings are as in Figure 25. In addition, triangle symbols at  $|i| = 0^\circ$  denote radius measured on H $\alpha$  optical emission maps. Note that the distances for the blue square symbols have been adjusted according to the correction factor discussed in footnote 14.

**Table 1.** Fitted planitude and alatitude for M42 bows

Source	Bow	$\Pi'$	$\langle \Lambda' \rangle$	$\Delta\Lambda'$
000-400	Inner	$2.87 \pm 0.19$	$2.40 \pm 0.04$	$0.35 \pm 0.08$
	Ridge	$3.62 \pm 0.38$	$2.73 \pm 0.02$	$0.51 \pm 0.10$
	Outer	$2.51 \pm 0.24$	$2.46 \pm 0.02$	$-0.06 \pm 0.02$
	All	$3.00 \pm 0.54$	$2.53 \pm 0.15$	$0.16 \pm 0.16$
069-601	Inner	$3.81 \pm 0.23$	$2.90 \pm 0.01$	$0.44 \pm 0.05$
	Ridge	$2.43 \pm 0.13$	$2.17 \pm 0.01$	$0.07 \pm 0.02$
	Outer	$2.22 \pm 0.15$	$2.11 \pm 0.01$	$0.01 \pm 0.01$
	All	$2.82 \pm 0.75$	$2.39 \pm 0.37$	$0.17 \pm 0.20$

the HD case). Finally, the distribution of projected-over-true apex distance is also broader for the MHD case.

## 7 EXAMPLE APPLICATION TO OBSERVATIONS

As an example of measuring the projected planitude and alatitude of real bow shocks, we present an analysis of M42 000-400 and M42 069-601, which are two H $\alpha$  emission arcs (Bally et al. 2000; Gutiérrez-Soto 2015) associated with proplyds<sup>16</sup> in the west of the Orion Nebula (M42) at a distance of roughly 0.5 pc from the high-mass Trapezium stars that ionize

<sup>16</sup> The coordinate designation (see O'Dell & Wen 1994 for an explanation of the nomenclature) of 000-400 is very imprecise in right ascension, but we use it here for consistency with previous papers. The associated proplyd is listed with the more correct designation 4596-400 in catalogs such as Ricci et al. (2008).

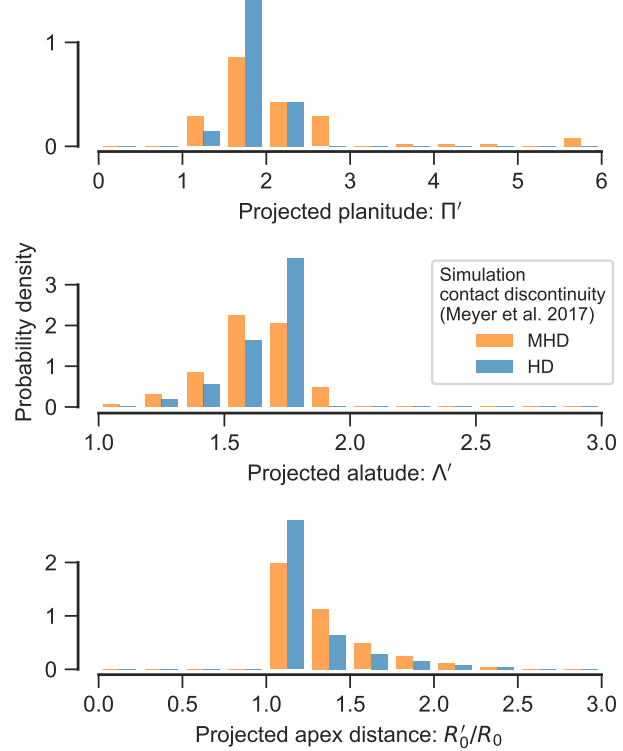


**Figure 27.** Histograms of (top to bottom) projected planitude, alatitude, and bow shock size for the shape of the contact discontinuity in the Meyer et al. (2017) simulations. The y axis gives the probability density (per unit x-axis quantity), assuming a uniform distribution of viewing directions.

the nebula. An image of one of these arcs (M42 069-601) was used in the illustration of bow shock terminology in Figure 1.

### 7.1 Empirical determination of bow shock shape

We consider three different tracings of the bow shape (see Fig. 28): the peak of the emission arc (“ridge”), and its inner and outer edges. In all three cases, we placed by eye the points that define the bow, using SAOImage DS9 (Joye & Mandel 2003) in a similar fashion to in Figure 22, and guided by the image contours.<sup>17</sup>

We determine the planitude and alatitude by fitting a circle to the traced points within  $\pm\Delta\theta = 75^\circ$  of the bow axis, using the iterative algorithm described in Appendix E. The fitted circle, when combined with the position of the central source, yields the orientation of the bow axis, together with the apex distance,  $R_0$ , radius of curvature,  $R_c$ , and two perpendicular radii (one for each wing),  $R_{90+}$  and  $R_{90-}$ . These are all indicated on the panels of Figure 28 by light-colored lines.<sup>18</sup> The projected planitude and alatitude then follow as  $\Pi' = R_c/R_0$ ,  $\Delta'_+ = R_{90+}/R_0$ ,  $\Delta'_- = R_{90-}/R_0$ , which are shown in Figure 29.

<sup>17</sup> In the case of the “ridge” method at least, it is possible to automate this step, which we will discuss in detail in a following paper.

<sup>18</sup> For conciseness, we drop the prime symbol from the radii, both in this section and in Appendix E, even though they are all projected quantities.

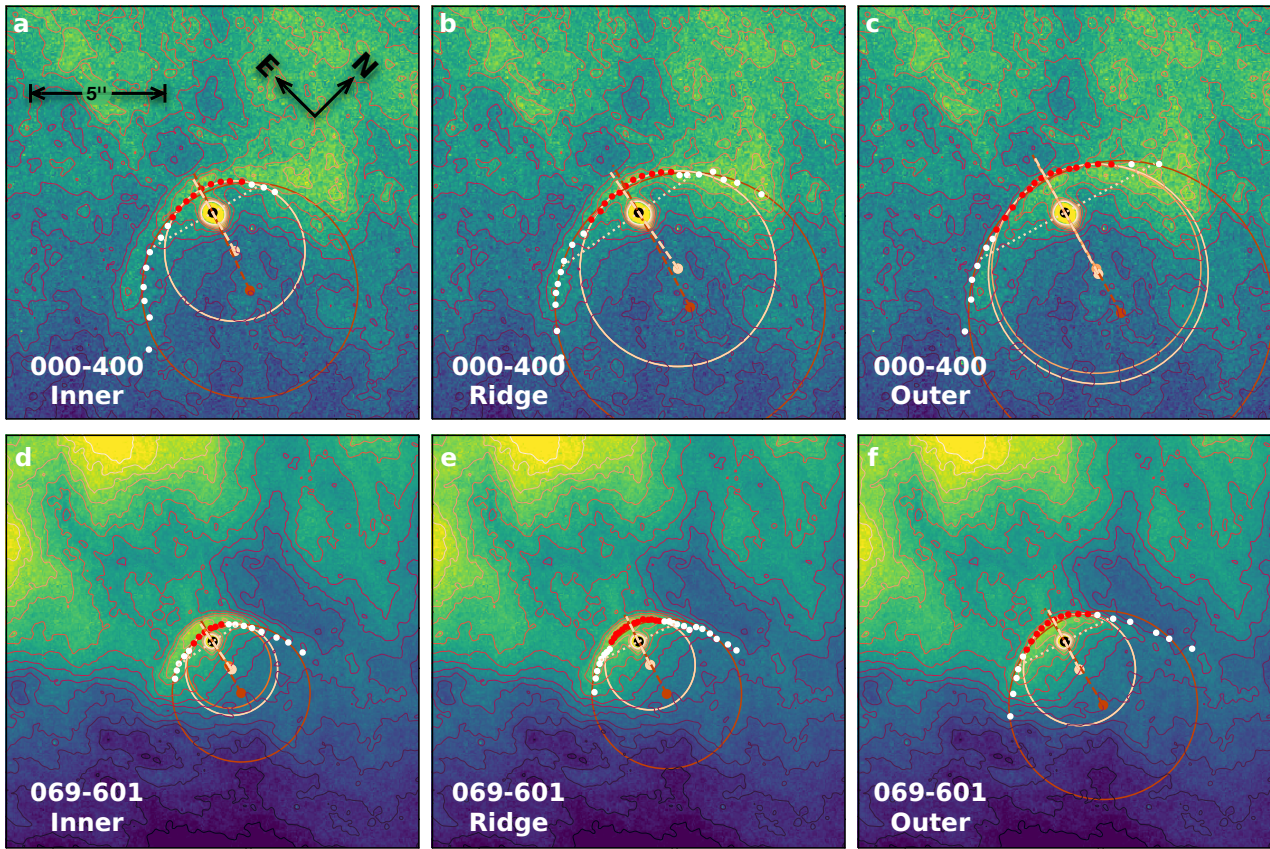


**Figure 28.** Example empirical determination of planitude and alatitude for observed bow shocks associated with proplyds in the outer Orion Nebula (M42). Color scale and contours show an *HST* H $\alpha$  image (ACS F658N filter; Bally et al. 2006) of M42 000-400 (panels *a–c*) and M42 069-601 (panels *d–f*). The image scale and orientation are indicated on panel *a* and are the same for all panels. Three different bows have been traced by eye on each object (red and white filled symbols): (*a, d*) inner edge, (*b, e*) ridge of maximum emission, and (*c, f*) outer edge. For each panel, the dark-colored circle shows the initial fit to the full set of points (white and red), using the algorithm described in Appendix E. The center of curvature and derived axis are shown by a small filled circle and dashed line in the same color. Lighter colored circles show three subsequent iterations where the fit is restricted to points within  $\pm\Delta\theta = 75^\circ$  of the axis. The subset of points used in the final iteration is marked in red. The perpendicular radii for the final iteration are shown by dotted lines. In panels *a, b, d–f* the iterations converge immediately, but in panel *c* the iterations stably oscillate between two slightly different solutions.

## 7.2 Analysis of sources of systematic uncertainty

The planitude is found to have a moderate dependence on the choice of  $\Delta\theta$ , as shown in Figure 30, where it can be seen that, although the values of  $\Pi'$  are relatively stable for  $\Delta\theta \gtrsim 60^\circ$  (light gray shaded region), they can show much larger variations for  $\Delta\theta < 60^\circ$ . The fact that the radius of curvature is defined at a point (the projected apex) might seem to argue for making  $\Delta\theta$  as small as possible, but that would lead to circle fits that were extremely sensitive to the exact positions of the few points included in the fit. A reliable fit requires 4 or more points, ideally spanning a total separation that is a substantial fraction of  $R_c$ , which would argue for  $\Delta\theta$  larger than about  $\Pi'/2$  radians, or  $60^\circ$  to  $90^\circ$ . On the other hand, if  $\Delta\theta \gtrsim 90^\circ$  then the planitude and alatitude would no longer be independent since the bow would be forced to lie on the “sphere” line,  $\Lambda' = (2\Pi' - 1)^{1/2}$  (see § 4). Balancing these two concerns suggests an optimal  $\Delta\theta = 75^\circ$ , which is shown in Figure 28, whereas in Figure 29 we show results for both  $75^\circ$  (thick lines) and  $60^\circ$  (thin lines).

Unlike all the models considered in § 5 and § 6, the observed

bows are not necessarily symmetrical and so the alatitude for the two wings,  $\Lambda'_+$  and  $\Lambda'_-$ , may be different. We therefore calculate an average alatitude,  $\langle\Lambda'\rangle$ , and an alatitude asymmetry,  $\Delta\Lambda'$ :

$$\langle\Lambda'\rangle = \frac{1}{2} (\Lambda'_+ + \Lambda'_-) \quad \Delta\Lambda' = \frac{1}{2} (\Lambda'_+ - \Lambda'_-) \quad (64)$$

The results for these two quantities, together with the planitude, are shown in Table 1. For each object and for each tracing (inner, ridge, outer, see Fig. 28), the mean  $\pm$  standard deviation is listed for circle fits using  $\Delta\theta = 60^\circ$  to  $80^\circ$  (see Fig. 30). Additionally, the row “All” for each object gives the global mean and standard deviation over all three tracings.

It can be seen from Table 1 that the uncertainty in the fitted parameters is dominated by the variations between the different traced shapes. For example, the one-sigma relative variation of planitude,  $\Pi'$ , is  $< 10\%$  within the individual tracings, but  $\approx 20\%$  between tracings. For the mean alatitude,  $\langle\Lambda'\rangle$ , the variation within individual tracings is extremely small<sup>19</sup> at  $\approx 1\%$ , but is  $\approx 10\%$

<sup>19</sup> This is because the only way that variation in the circle fit parameters

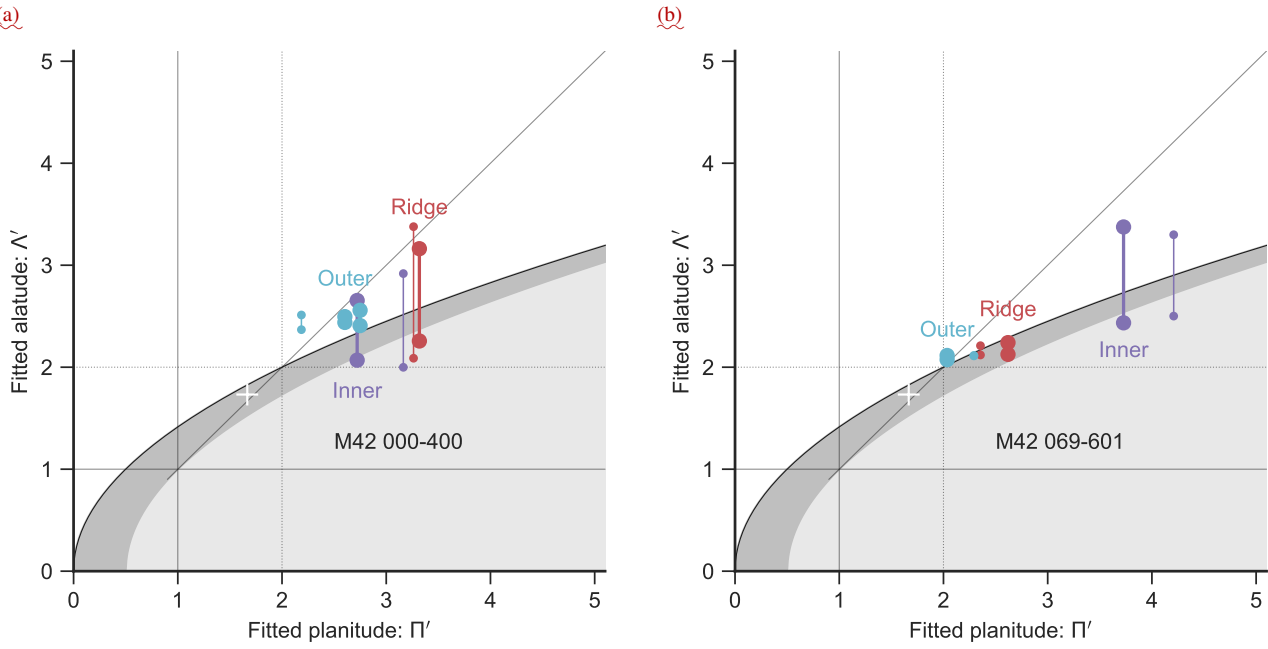


**Figure 29.** Location in the projected planitude–alatitude plane of the converged circle fits to the M42 bows: (a) 000-400, (b) 069-601. For each solution, the two values of the projected alatitude,  $\Lambda'_+$  and  $\Lambda'_-$ , corresponding to  $R_{90+}$  and  $R_{90-}$ , are joined by a vertical line. Large symbols show the results from the fits shown in Figure 28, while small symbols show results for fits using  $\Delta\theta = 60^\circ$  instead of  $75^\circ$ . In panel a, two slightly different  $\Pi'$  values are shown for the outer bow, since the fit does not converge to a single value (see Fig. 28c and App. E).

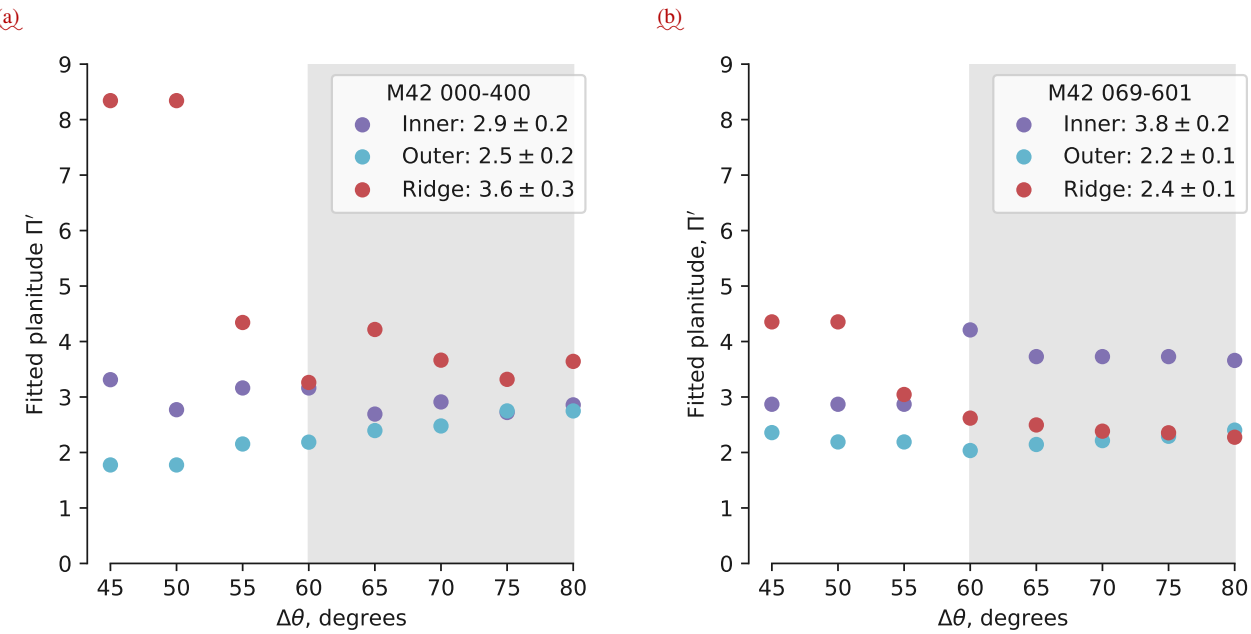


**Figure 30.** Variation of fitted planitude,  $\Pi'$ , as a function of the parameter  $\Delta\theta$ , which controls how close a point must be to the axis in order to be included in the circle fit. (a) M42 000-400, (b) M42 069-601. For the three traced bows (inner, outer, and ridge) of each object, the symbol key lists the mean and standard deviation of  $\Pi'$ , calculated over the “stable” range  $\Delta\theta = 60^\circ$  to  $80^\circ$ , which is indicated by light gray shading.

between tracings. The alatitude asymmetry,  $\Delta\Lambda'$ , is best interpreted as a difference between the symmetry axis of the apex region and the symmetry axis of the wings. In relative terms, this is 0–20%, but with large systematic variations between tracings (for instance, in both objects it is very small for the outer arcs).

*It could be argued that much of the between-tracing variations in  $\Pi'$  and  $\langle\Lambda'\rangle$  are due to real differences between the shapes of the inner and outer boundaries of the emission arc. Although this may be true, in the absence of a robust theory as to exactly what feature of the observed images constitutes the bow shock, such variations nevertheless serve to limit the precision with which the bow shock shape can be measured. We therefore conclude that conservative estimates of 20% precision for  $\Pi'$  and 10% precision for  $\Lambda'$  are appropriate when analyzing observations of a similar or better quality<sup>20</sup> to those presented in Figure 28. This will be an important limitation when comparing the statistics of the shapes of different bow shock populations, as we will present in a following paper.*

### 7.3 Derived shape of the M42 arcs

From a casual inspection of Figure 28, it is apparent that the shapes of the two M42 arcs are closely similar, and this is confirmed by the numbers in Table 1. Both 000–400 and 069–601 are consistent with  $(\Pi', \Lambda') \approx (3.0, 2.5)$ , and if we take the absolute minimum over all the different tracings and reasonable variations in the  $\Delta\theta$  fit parameter, we find unassailable lower limits of  $(\Pi', \Lambda') > (2.1, 2.1)$ . In the rest of this section, we consider only these lower limits, since they are already sufficient for drawing interesting conclusions.

Comparison with Figure 25 shows that both the MHD and HD simulations of Meyer et al. (2016) are inconsistent with the observations. Although  $\Pi' > 2.1$  can be satisfied,<sup>21</sup> the simulations' projected alatitude is  $\Lambda' < 1.9$  for all inclinations, which is significantly less than the observed lower limit of 2.1. This is not particularly surprising since the simulations were not tailored to the situation of these proplyd bow shocks in M42, in which the mildly supersonic photoevaporation flow from an externally irradiated protoplanetary disk interacts with the mildly supersonic champagne flow from the core of the Orion Nebula. The proplyd case has at least four important differences from the runaway O-star case modeled by Meyer et al. (2016): (1) The velocity of the outer wind is  $\lesssim 20 \text{ km s}^{-1}$  instead of  $40 \text{ km s}^{-1}$ ; (2) The outer wind is slightly divergent, rather than plane-parallel; (3) Both inner and outer shocks are strongly radiative, so both shells (see Fig. 2) contribute to the observed emission; (4) The inner wind is not isotropic, but instead corresponds to the  $k = 0.5$  case of equation (53). The ways in which these differences may account for the discrepancy with the observations will be explored in detail in a subsequent paper.

affect the alatitudes is through the axis orientation vector, and changing the orientation induces roughly opposite effects on  $\Lambda'_+$  and  $\Lambda'_-$ , which approximately cancel out in  $\langle\Lambda'\rangle$ .

<sup>20</sup> Since the uncertainties are systematic and due to unavoidably subjective decisions, it is unlikely that better quality observations would improve the situation, although poorer quality observations could make things worse.

<sup>21</sup> Either by the MHD simulations at low inclinations ( $|i| = 0^\circ–20^\circ$ ) or by the HD simulation at intermediate inclinations ( $|i| = 30^\circ–40^\circ$ ).

## 8 SUMMARY AND DISCUSSION

We have shown that the shapes of stellar bow shocks can be usefully characterized by two dimensionless numbers: the *planitude*,  $\Pi$ , or flatness of the bow's apex, and the *alatitude*,  $\Lambda$ , or openness of the bow's wings (§ 2). The planitude and alatitude can be estimated from ratios of lengths that can be straightforwardly measured from observations or theoretical models. We develop a general method (§ 3) for finding the projected shape,  $(\Pi', \Lambda')$ , of a bow shock's limb-brightened edge, or *tangent line*, as a function of inclination angle,  $i$ , where the emission shell is idealized as a cylindrically symmetric surface.

We first apply this method to find inclination-dependent tracks on the projected planitude–alatitude plane for the special case of *quadric* surfaces (§ 4), such as hyperboloids, paraboloids, and spheroids, where the tangent line is a conic section. The spheroids and hyperboloids occupy distinct regions of the plane, with the paraboloids defining the boundary between the two. As the inclination is increased from  $|i| = 0$  (side-on) to  $|i| = 90^\circ$  (end-on), the tracks first tend to approach the diagonal  $\Lambda' = \Pi'$ , corresponding to confocal conics, always remaining within their own region. At the highest inclinations, the spheroids all converge at  $|i| = 90^\circ$  on the point  $(\Pi', \Lambda') = (1, 1)$  and the paraboloids on the point  $(\Pi', \Lambda') = (2, 2)$ . The hyperboloids, on the other hand diverge as  $(\Pi', \Lambda') \rightarrow (\infty, \infty)$  for a finite  $i_{\text{crit}}$ , which depends on the asymptotic opening angle of the tail. For  $|i| > i_{\text{crit}}$ , the tangent line no longer exists for the hyperboloid, and it would no longer appear to be a curved bow shock. We introduce the parabolic departure function (§ 4.1) as tool for visualizing differences in bow shapes,  $R(\theta)$ , over the full range,  $\theta = [0^\circ, 180^\circ]$ .

We then apply the projection method to a set of thin-shell hydrodynamic models of bow shocks (§ 5): the *wilkinoid* from a wind-parallel stream interaction and the *cantoids* from wind-wind interactions. We generalize the latter to the *ancantoids*, where one of the winds is anisotropic. We find that the wilkinoid is confined to a small region of the  $\Pi'-\Lambda'$  plane, with projected planitude and alatitude varying with inclination by  $< 15\%$ . The cantoids and ancantoids with sufficiently small values of  $\beta$ , the wind momentum ratio, have more interesting behavior, with tracks that pass from the spheroid region at low inclinations to the hyperboloid region at high inclinations.

Finally In the following section (§ 6), we test the projected shape analysis methods against the results of computational fluid dynamic simulations of magnetized and non-magnetized bow shocks from Meyer et al. (2017) of a runaway OB main-sequence star. We find that measurements made on maps of infrared dust emission can be accurate diagnostics of the projected shape of the contact discontinuity for this type of bow shock (Fig. 25). The distributions of projected planitude and alatitude for a population of randomly oriented bow shocks shows systematic differences between the different simulations.

Finally (§ 7), we give an example of the application of our methods to observed emission maps of bow shocks, describing a robust algorithm for empirically determining the projected planitude and alatitude from imperfect real data. We investigate the sensitivity of the results to systematic errors due to both observational uncertainties and subjective choices in the application of the algorithm. We find that the projected planitude and alatitude can be determined with precisions of 20% and 10%, respectively. For our illustrative observations, we show that this is more than sufficient to rule out certain models.

This paper is the first of a series that will apply our shape

## 22 Tarango-Yong & Henney

analysis to a wide variety of models and observations of stellar bow shocks. In a second paper, we consider the alternative model of dusty radiation-driven bow wave (Ochsendorf et al. 2014), instead of a hydrodynamic bow shock, and also calculate the signature in the planitude–alatitude plane of oscillations in the bow shape, which may be due to instabilities or a time-varying source. In a third paper, we apply our techniques to observational datasets for three different classes of stellar bow shocks: OB stars (Kobulnicky et al. 2016), cool giants/supergiants (Cox et al. 2012), and young stars in the extended Orion Nebula (Henney et al. 2013). In a fourth paper, we analyze the proplyd bow shocks in the core of the Orion Nebula (García-Arredondo et al. 2001).

## ACKNOWLEDGEMENTS

We are grateful for financial support provided by Dirección General de Asuntos del Personal Académico, Universidad Nacional Autónoma de México, through grant Programa de Apoyo a Proyectos de Investigación e Innovación Tecnológica IN111215. JATY acknowledges support via a research studentship from Consejo Nacional de Ciencias y Tecnología, Mexico. This work has made extensive use of Python language libraries from the SciPy (Jones et al. 2018) and AstroPy (Astropy Collaboration et al. 2013, 2018) projects. We appreciate the thoughtful comments of the anonymous referee, which led us to clarify the presentation of our results and prompted the addition of § 7 and Appendices A and B.

## REFERENCES

- Astropy Collaboration et al., 2013, *A&A*, 558, A33  
 Astropy Collaboration et al., 2018, preprint, (@eprint arXiv 1801.02634)  
 Bally J., O'Dell C. R., McCaughrean M. J., 2000, *AJ*, 119, 2919  
 Bally J., Licht D., Smith N., Walawender J., 2006, *AJ*, 131, 473  
 Canto J., Raga A. C., Wilkin F. P., 1996, *ApJ*, 469, 729  
 Cox N. L. J., et al., 2012, *A&A*, 537, A35  
 García-Arredondo F., Henney W. J., Arthur S. J., 2001, *ApJ*, 561, 830  
 Gayley K. G., 2009, *ApJ*, 703, 89  
 Gfrerrer A., Zsombor-Murray P., 2009, *Journal for Geometry and Graphics*, 13, 131  
 Goldman R., 1983, *IEEE Computer Graphics and Applications*, 3, 68  
 Graham M. F., Meaburn J., Garrington S. T., O'Brien T. J., Henney W. J., O'Dell C. R., 2002, *ApJ*, 570, 222  
 Guggenheim H., 2012, *Differential Geometry*, Dover Books on Mathematics, Dover Publications  
 Gutiérrez-Soto L. A., 2015, Master's thesis, Universidad Nacional Autónoma de México  
 Hartigan P., Raymond J., Hartmann L., 1987, *ApJ*, 316, 323  
 Hayward T. L., Houck J. R., Miles J. W., 1994, *ApJ*, 433, 157  
 Henney W. J., 2002, *Revista Mexicana de Astronomía y Astrofísica*, 38, 71  
 Henney W. J., García-Díaz M. T., O'Dell C. R., Rubin R. H., 2013, *MNRAS*, 428, 691  
 Jones E., Oliphant T., Peterson P., et al., 2001–2018, SciPy: Open source scientific tools for Python, <http://www.scipy.org/>  
 Joye W. A., Mandel E., 2003, in Payne H. E., Jedrzejewski R. I., Hook R. N., eds, *Astronomical Society of the Pacific Conference Series Vol. 295, Astronomical Data Analysis Software and Systems XII*, p. 489  
 Kobulnicky H. A., Gilbert I. J., Kiminki D. C., 2010, *ApJ*, 710, 549  
 Kobulnicky H. A., et al., 2016, *ApJS*, 227, 18  
 Mackey J., Mohamed S., Neilson H. R., Langer N., Meyer D. M.-A., 2012, *ApJ*, 751, L10  
 Mackey J., Gvaramadze V. V., Mohamed S., Langer N., 2015, *A&A*, 573, A10  
 Markevitch M., Gonzalez A. H., David L., Vikhlinin A., Murray S., Forman W., Jones C., Tucker W., 2002, *ApJ*, 567, L27  
 Meaburn J., Boumis P., Akras S., 2013, *MNRAS*, 435, 3462  
 Medina S.-N. X., Arthur S. J., Henney W. J., Mellema G., Gazol A., 2014, *MNRAS*, 445, 1797  
 Meyer D. M.-A., Mackey J., Langer N., Gvaramadze V. V., Mignone A., Izzard R. G., Kaper L., 2014, *MNRAS*, 444, 2754  
 Meyer D. M.-A., van Marle A.-J., Kuiper R., Kley W., 2016, *MNRAS*, 459, 1146  
 Meyer D. M.-A., Mignone A., Kuiper R., Raga A. C., Kley W., 2017, *MNRAS*, 464, 3229  
 Mohr P. J., Phillips W. D., 2015, *Metrologia*, 52, 40  
 Ng C.-Y., Bandiera R., Hunstead R. W., Johnston S., 2017, *ApJ*, 842, 100  
 O'Dell C. R., Wen Z., 1994, *ApJ*, 436, 194  
 Ochsendorf B. B., Verdolini S., Cox N. L. J., Berné O., Kaper L., Tiemens A. G. G. M., 2014, *A&A*, 566, A75  
 Penrose R., 2004, *The road to reality : a complete guide to the laws of the universe*, Jonathan Cape, London  
 Phillips J. P., Cuesta L. C., Ramos-Larios G., 2010, *MNRAS*, 409, 881  
 Quincey P., Brown R. J. C., 2017, *Metrologia*, 54, 454  
 Raga A. C., Binette L., Canto J., Calvet N., 1990, *ApJ*, 364, 601  
 Ricci L., Robberto M., Soderblom D. R., 2008, *AJ*, 136, 2136  
 Robberto M., et al., 2005, *AJ*, 130, 1534  
 Scherer K., Fichtner H., 2014, *ApJ*, 782, 25  
 Schwartz R. D., 1978, *ApJ*, 223, 884  
 Shu F. H., Lizano S., Galli D., Canto J., Laughlin G., 2002, *ApJ*, 580, 969  
 Smith N., Bally J., Shuping R. Y., Morris M., Kassis M., 2005, *AJ*, 130, 1763  
 Stevens I. R., Blondin J. M., Pollock A. M. T., 1992, *ApJ*, 386, 265  
 Tenorio-Tagle G., 1979, *A&A*, 71, 59  
 Weisstein E. W., 1999–2018, *Radius of Curvature*, From MathWorld – A Wolfram Web Resource, <http://mathworld.wolfram.com/RadiusofCurvature.html>  
 Wilkin F. P., 1996, *ApJ*, 459, L31  
 Wilkin F. P., 1997, PhD thesis, University of California, Berkeley  
 Wilkin F. P., 2000, *ApJ*, 532, 400  
 Wilson A. S., Ulvestad J. S., 1987, *ApJ*, 319, 105  
 Zank G. P., 1999, *Space Sci. Rev.*, 89, 413  
 de Sterck H., Poedts S., 1999, *A&A*, 343, 641  
 van Buren D., McCray R., 1988, *ApJ*, 329, L93  
 van Dyke M., 1982, *An album of fluid motion*. Parabolic Press, Stanford, CA  
 van Marle A. J., Meliani Z., Keppens R., Decin L., 2011, *ApJ*, 734, L26

## APPENDIX A: RADIUS OF CURVATURE

The radius of curvature of a general curve can be written (e.g., eq. [2-5] of Guggenheimer 2012):

$$R_c \equiv \frac{1}{|\kappa|} = \left| \frac{ds}{d\alpha} \right|, \quad (\text{A1})$$

where  $\kappa$  is the curvature,  $s$  is the path length along the curve and  $\alpha$  is the tangent angle (see Fig. 6). In spherical polar coordinates, this becomes (Weisstein 2018):

$$R_c = \frac{\left( R^2 + R_\theta^2 \right)^{3/2}}{|R^2 + 2R_\theta^2 - RR_{\theta\theta}|}, \quad (\text{A2})$$

where  $R_\theta = dR/d\theta$  and  $R_{\theta\theta} = d^2R/d\theta^2$ . At the apex,  $R_\theta = 0$  by symmetry, which yields equation (3) of § 2. Note that  $\theta$  is dimensionless and should be measured in radians (Mohr & Phillips 2015; Quincey & Brown 2017).

## APPENDIX B: ROTATION MATRICES AND PLANE OF SKY PROJECTION

The transformation from the body frame (unprimed) to observer-frame (primed) coordinates is a rotation about the  $y$  axis by an angle  $i$ , which is described by the rotation matrix:

$$\mathbf{A}_y(i) = \begin{pmatrix} \cos i & 0 & -\sin i \\ 0 & 1 & 0 \\ \sin i & 0 & \cos i \end{pmatrix}. \quad (\text{B1})$$

This is used in equation (8). A further application is to express the observer-frame Cartesian basis vectors in terms of the body-frame basis:

$$\hat{\mathbf{x}}' = \mathbf{A}_y(-i) \begin{pmatrix} 1 \\ 0 \\ 0 \end{pmatrix} = \begin{pmatrix} \cos i \\ 0 \\ -\sin i \end{pmatrix}, \quad (\text{B2})$$

$$\hat{\mathbf{y}}' = \mathbf{A}_y(-i) \begin{pmatrix} 0 \\ 1 \\ 0 \end{pmatrix} = \begin{pmatrix} 0 \\ 1 \\ 0 \end{pmatrix}, \quad (\text{B3})$$

$$\hat{\mathbf{z}}' = \mathbf{A}_y(-i) \begin{pmatrix} 0 \\ 0 \\ 1 \end{pmatrix} = \begin{pmatrix} \sin i \\ 0 \\ \cos i \end{pmatrix}. \quad (\text{B4})$$

Note that in this case the sign of  $i$  is reversed because it is the inverse operation to that in equation (8)

Since we are considering cylindrically symmetric bows, all azimuths  $\phi$  are equivalent, so it is sufficient to work with two-dimensional curves in the plane  $z = 0$  (which is also  $\phi = 0$ ) and then find the three-dimensional surface by rotating about the  $x$ -axis via the rotation matrix:

$$\mathbf{A}_x(\phi) = \begin{pmatrix} 1 & 0 & 0 \\ 0 & \cos \phi & -\sin \phi \\ 0 & \sin \phi & \cos \phi \end{pmatrix}, \quad (\text{B5})$$

where  $\phi$  takes all values in the interval  $[0, 2\pi]$ .

## APPENDIX C: PARABOLOIDS AND THEIR PLANE-OF-SKY PROJECTION

Equation (25) for the  $xy$  coordinates of a quadric in the  $\phi = 0$  plane cannot be used in the case of a paraboloid ( $Q = 0$ ). Instead, a convenient parametrization is

$$\begin{aligned} x &= R_0 \left(1 - \frac{1}{2}\Pi t^2\right) \\ y &= R_0 \Pi t, \end{aligned} \quad (\text{C1})$$

where we have ‘‘baked in’’ knowledge of the planitude,  $\Pi = R_c/R_0$  (see § 2). The projected plane-of-sky coordinates of the tangent line follow from equation (8) as

$$\begin{aligned} x'_T/R_0 &= \left(1 - \frac{1}{2}\Pi t^2\right) \cos i + \Pi t \sin \phi_T \sin i \\ y'_T/R_0 &= \Pi t \cos \phi_T, \end{aligned} \quad (\text{C2})$$

The azimuth of the tangent line is found from equations (10, 15) as  $\sin \phi_T = -t^{-1} \tan i$ , so that

$$\begin{aligned} x'_T/R_0 &= \cos i \left[1 + \frac{1}{2}\Pi \tan^2 i - \frac{1}{2}\Pi \left(t^2 - \tan^2 i\right)\right] \\ y'_T/R_0 &= \Pi \left(t^2 - \tan^2 i\right)^{1/2}. \end{aligned} \quad (\text{C3})$$

The projected star-apex distance,  $R'_0$ , is the value of  $x'_T$  when  $y'_T = 0$ , yielding

$$R'_0/R_0 = \cos i \left(1 + \frac{1}{2}\Pi \tan^2 i\right). \quad (\text{C4})$$

Note that this same result can be obtained from a Taylor expansion of equation (45) substituted into (49) in the limit  $Q \rightarrow 0$ .

Equation (C3) can be rewritten in the form

$$\begin{aligned} x'_T &= R'_0 \left(1 - \frac{1}{2}\Pi' t'^2\right) \\ y'_T &= R'_0 \Pi' t', \end{aligned} \quad (\text{C5})$$

where

$$\Pi' = \frac{2\Pi}{2 \cos^2 i + \Pi \sin^2 i} \quad (\text{C6})$$

$$t' = \cos i \left(t^2 - \tan^2 i\right)^{1/2}, \quad (\text{C7})$$

which demonstrates that the projected shape is also a parabola. It is apparent from (C6) that the projected planitude obeys

$$\lim_{i \rightarrow 90^\circ} \Pi' = 2,$$

for all values of the true planitude  $\Pi$ , as is shown by the black lines in Figure 10a. The projected alatitude can be found as

$$\Lambda' = (2\Pi')^{1/2}. \quad (\text{C8})$$

For the special case of the confocal paraboloid,  $\Pi = \Lambda = 2$ , we have  $\Pi' = \Pi$  and  $\Lambda' = \Lambda$  by equations (C6) and (C8) for all inclinations, so its shape is unaffected by projection.

## APPENDIX D: ANALYTIC DERIVATION OF THIN-SHELL BOW SHAPE PARAMETERS

In this appendix, we provide analytic calculations of the planitude, alatitude, and asymptotic opening angle for the wilkinoid, cantoids, and ancantoids. We first consider the most general case of the ancantoids, and then show how results for cantoids and the wilkinoid follow as special cases.

### D1 Planitude of ancantoids

From equations (3) and (5), the planitude depends on the apex second derivative,  $R_{\theta\theta,0}$ , as

$$\Pi = \left(1 - R_{\theta\theta,0}/R_0\right)^{-1}. \quad (\text{D1})$$

From equation (4), the second derivative can be found from the coefficient of  $\theta^2$  in the Taylor expansion of  $R(\theta)$ . Since we do not have  $R(\theta)$  in explicit analytic form, we proceed via a Taylor expansion of the implicit equations (60) and (61), retaining terms up to  $\theta^4$  to obtain from equation (61):

$$\theta_1^2 = \beta\theta^2 \left(1 + C_{k\beta}\theta^2\right) + O(\theta^6), \quad (\text{D2})$$

with the coefficient  $C_{k\beta}$  given by

$$C_{k\beta} = \frac{1}{15} - \frac{3k}{20} - \frac{\beta}{15}. \quad (\text{D3})$$

Note that it is necessary to include the  $\theta^4$  term in the expansion of  $\theta_1^2$  so that  $\theta_1/\theta$  is accurate to order  $\theta^2$ . Then, from equation (60) we find

$$\begin{aligned} \frac{R}{D} &= \frac{\sin \theta_1}{\sin(\theta + \theta_1)} \\ &= \frac{\beta^{1/2}}{1 + \beta^{1/2}} \left\{1 + \theta^2 \left[\frac{C_{k\beta}}{2(1 + \beta^{1/2})} + \frac{1}{6}(1 + 2\beta^{1/2})\right]\right\} + O(\theta^4), \end{aligned} \quad (\text{D4})$$

## 24 Tarango-Yong & Henney

where in the second line we have carried out a Taylor expansion of the two sin terms and substituted (D2). Comparing coefficients of unity and  $\theta^2$  between equations (4) and (D4) we find

$$\frac{R_0}{D} = \frac{\beta^{1/2}}{1 + \beta^{1/2}} \quad (\text{D5})$$

$$\frac{R_{\theta\theta,0}}{R_0} = \frac{C_k \beta}{1 + \beta^{1/2}} + \frac{1}{3} (1 + 2\beta^{1/2}), \quad (\text{D6})$$

so that the final result for the planitude, from (D1), is

$$\text{ancantoid } \Pi = \left[ 1 - \frac{C_k \beta}{1 + \beta^{1/2}} - \frac{1}{3} (1 + 2\beta^{1/2}) \right]^{-1}. \quad (\text{D7})$$

### D2 Alatitude of ancantoids

To find the alatitude,  $\Lambda = R_{90}/R_0$ , we use equation (60) at  $\theta = 90^\circ$  to write

$$\Lambda = \frac{D}{R_0} \tan \theta_{1,90}, \quad (\text{D8})$$

where  $\theta_{1,90} = \theta_1(\theta = 90^\circ)$ , which, following equation (61), must satisfy

$$\theta_{1,90} \cot \theta_{1,90} = 1 - \frac{2\beta}{k+2}. \quad (\text{D9})$$

Combining (D8) and (D9) with (D5) yields

$$\Lambda = \frac{(1 + \beta^{1/2}) \theta_{1,90}}{\beta^{1/2} (1 - \xi_k \beta)}, \quad (\text{D10})$$

where

$$\xi_k = \frac{2}{k+2}. \quad (\text{D11})$$

We now take the Taylor expansion of equation (D9) to find

$$\theta_{1,90}^2 + \frac{1}{15} \theta_{1,90}^4 + O(\theta_{1,90}^6) = 3\xi_k \beta, \quad (\text{D12})$$

which, if  $\theta_{1,90}$  is small, has the approximate solution

$$\theta_{1,90} \approx \left( \frac{3\xi_k \beta}{1 + \frac{1}{5}\xi_k \beta} \right)^{1/2}. \quad (\text{D13})$$

Substituting back into equation (D8) yields an approximate value for the alatitude of

$$\text{ancantoid } \Lambda \approx \frac{(3\xi_k)^{1/2} (1 + \beta^{1/2})}{\left(1 + \frac{1}{5}\xi_k \beta\right)^{1/2} (1 - \xi_k \beta)}. \quad (\text{D14})$$

This approximation is surprisingly accurate, with a relative error of order 1% even for  $\beta$  as large as 0.5 with  $k = 0$ .

### D3 Planitude and alatitude of cantoids and wilkinoid

Since  $\Pi$  and  $\Lambda$  depend on only that portion of the inner wind emitted in the forward hemisphere,  $\theta \leq 90^\circ$ , the results for the cantoids can be found by taking  $k = 0$ , in which case equations (D3, D7, D11, D14) yield

$$\text{cantoid } \begin{cases} \Pi = \frac{5}{3(1 - \beta^{1/2})} \\ \Lambda = \frac{\sqrt{3}}{\left(1 + \frac{1}{5}\beta\right)^{1/2} (1 - \beta^{1/2})} \end{cases}. \quad (\text{D15})$$

The wilkinoid shape is equal to the  $\beta \rightarrow 0$  limit of the cantoid, so its planitude and alatitude are given by:

$$\text{wilkinoid } \begin{cases} \Pi = \frac{5}{3} \\ \Lambda = \sqrt{3}. \end{cases} \quad (\text{D16})$$

The wilkinoid results can also be obtained directly from equation (52), and in the case of  $\Lambda$  this has already been noted by several authors (Cox et al. 2012; Meyer et al. 2016).

### D4 Asymptotic opening angle

The asymptotic opening angle of the far wings,  $\theta_\infty$ , can be found from equation (61) for the ancantoids, together with the condition that  $\theta_\infty + \theta_{1\infty} = \pi$ . These yield the implicit equation

$$\theta_\infty - \left( \frac{k + 2(1 - \beta)}{k + 2} \right) \tan \theta_\infty = \pi + 2\beta I_k(\pi/2), \quad (\text{D17})$$

where

$$I_k(\pi/2) = \frac{\sqrt{\pi}}{4} \frac{\Gamma\left(\frac{k+1}{2}\right)}{\Gamma\left(\frac{k+4}{2}\right)} \quad (\text{D18})$$

and  $\Gamma$  is the usual Gamma function. This can be compared with the equivalent result obtained by CRW for the cantoids:

$$\theta_\infty - \tan \theta_\infty = \frac{\pi}{1 - \beta}. \quad (\text{D19})$$

Note that, unlike in the cases of  $\Pi$  and  $\Lambda$ , equation (D17) does not reduce to equation (D19) in the limit  $k \rightarrow 0$ . This is because, for  $\theta > 90^\circ$ , the  $k = 0$  ancantoid differs from the cantoid since the former has no wind in the backward hemisphere (see Figure 13). Therefore there is less inner support for the far wings of the bow, and so  $\theta_\infty$  is smaller than in the cantoid case. The wilkinoid result again follows from  $\beta \rightarrow 0$ , implying that  $\theta_\infty = \pi$ , or, in other words, that the far wings are asymptotically parallel to the symmetry axis, as is the case for the paraboloid (App. C). In the case of the wilkinoid, however, the behavior is cubic in the wings,  $z \sim r^3$ , as opposed to quadratic as in the paraboloid.

## APPENDIX E: EMPIRICAL DETERMINATION OF RADIUS OF CURVATURE FOR A BOW SHOCK OF UNKNOWN ORIENTATION

Consider a set of  $N$  points on the plane of the sky,<sup>22</sup> with Cartesian coordinates  $\mathbf{r}_k = (x_k, y_k)$  for  $k = 1 \dots N$ . We wish to estimate the radius of curvature of the smooth curve that the set of points is presumed to be sampled from. To do this, we fit a circle to the points as follows. The circle is defined by its center,  $\mathbf{r}_c = (x_c, y_c)$ , and radius,  $R_c$ . For a given circle, we define a mean radius of the set of points from the circle center:

$$\bar{R}_c(x_c, y_c) = \frac{1}{N} \sum_{k=1}^N |\mathbf{r}_k - \mathbf{r}_c|. \quad (\text{E1})$$

<sup>22</sup> In the main body of the paper, the prime symbol ('') is used to distinguish projected from “true” quantities. In this Appendix, for simplicity, we omit the primes since all quantities are projected.

We then optimize<sup>23</sup> to find best-fit values  $(x_c^*, y_c^*)$ , which minimize the objective function

$$f(x_c, y_c) = \sum_{k=1}^N (|\mathbf{r}_k - \mathbf{r}_c| - \bar{R}_c(x_c, y_c))^2. \quad (\text{E2})$$

The best-fit radius of curvature is then given by  $R_c^* = \bar{R}(x_c^*, y_c^*)$ .

If we also know the position,  $\mathbf{r}_0 = (x_0, y_0)$ , of the bow's central source, then we can find the unit vector in the direction of the bow's projected axis as

$$\hat{\xi} = \frac{\mathbf{r}_0 - \mathbf{r}_c^*}{|\mathbf{r}_0 - \mathbf{r}_c^*|}, \quad (\text{E3})$$

and the apex distance from the source as<sup>23</sup>

$$R_0 = |\mathbf{r}_c^* + R_c^* \hat{\xi} - \mathbf{r}_0|. \quad (\text{E4})$$

A refinement of the method is then to iteratively repeat the circle fit after restricting the set of points to those lying within a certain angle  $\Delta\theta$  of the bow axis<sup>by requiring</sup>, where we find that best results are obtained with  $\Delta\theta \approx 60^\circ$  to  $75^\circ$ . That is,

$$|\theta_k| < \Delta\theta, \quad (\text{E5})$$

where the signed angle  $\theta_k$  of each point from the axis,<sup>24</sup> measured at the source position  $\mathbf{r}_0$ , can be calculated as

$$\theta_k = \arctan \left[ \frac{(\mathbf{r}_k - \mathbf{r}_0) \cdot \hat{\xi}^\perp}{(\mathbf{r}_k - \mathbf{r}_0) \cdot \hat{\xi}} \right]. \quad (\text{E6})$$

In the preceding equation, the “perpendicular” operator ( $\perp$ ) rotates its vector argument counter-clockwise by  $90^\circ$ , so that  $(x, y)^\perp = (-y, x)$ .

Two or three iterations are sufficient for convergence in most cases, although in some cases it is possible that the process will converge to a stable flip-flop oscillation between two different solutions. This is due to the dependence of the  $\theta_k$ , via  $\hat{\xi}$ , on the  $\mathbf{r}_c^*$  of the previous iteration, which can lead to points entering and leaving the fitted set. We have not found this to be a serious problem in practice, since the two solutions tend to be very close to one another. It could be mitigated by averaging  $\mathbf{r}_c^*$  over two previous iterations. The alternative of measuring the angle with respect to the center of curvature,  $\mathbf{r}_c^*$ , instead of the source,  $\mathbf{r}_0$ , is found to be much less stable.

If quantitative estimates exist for the uncertainties,  $\epsilon_k$ , in the measurements of  $\mathbf{r}_k$ , then it is appropriate to incorporate weights of  $\epsilon_k^{-2}$  in the objective function. However, it is rare for the  $\epsilon_k$  to be objectively quantifiable, since the uncertainties are often systematic and/or subjective. In cases where the bow shape is traced by eye, based on real or synthetic observations, a more practical approach is to maintain uniform weighting but to place a greater density of points  $\mathbf{r}_k$  in regions where the shape is well-determined and to place them more sparsely in regions where the shape is less certain.

Since there is no guarantee of symmetry about the axis  $\hat{\xi}$ , the perpendicular radius will in general be different in the two wings

<sup>23</sup> For example, using a Levenberg–Marquardt algorithm, such as `astropy.modeling.fitting.LevMarLSQFitter` from the `AstroPy` library (Astropy Collaboration et al. 2013).

<sup>24</sup> This is only valid if the resultant  $R_0 < R_c^*$ , otherwise the opposite sign of  $\hat{\xi}$  must be taken.

<sup>24</sup> Although the sign of  $\theta_k$  is not relevant to equation (E5), it is used below in calculating the perpendicular radii.

of the bow, with values  $R_{90+}$  and  $R_{90-}$ . These can be estimated by defining

$$R_k = |\mathbf{r}_k - \mathbf{r}_0| \quad (\text{E7})$$

and linearly interpolating between the points  $(\theta_k, R_k)$  at  $\theta = \pm 90^\circ$ .

Our Python language implementation of this algorithm is freely available at <https://github.com/div-B-equals-0/circle-fit>. An example application to real data is given in § 7 and Figure 28. Note that this method is not necessary if the orientation of the bow axis is known a priori, in which case the Taylor series method described in § 2 is more efficient and accurate.

This paper has been typeset from a `TeX/LaTeX` file prepared by the author.

# True versus apparent shapes of bow shocks

Jorge A. Tarango-Yong<sup>\*</sup> & William J. Henney<sup>†</sup>

*Instituto de Radioastronomía y Astrofísica, Universidad Nacional Autónoma de México, Apartado Postal 3-72, 58090 Morelia, Michoacán, México*

Accepted XXX. Received YYY; in original form ZZZ

## ABSTRACT

Astrophysical bow shocks are a common result of the interaction between two supersonic plasma flows, such as winds or jets from stars or active galaxies, or streams due to the relative motion between a star and the interstellar medium. For cylindrically symmetric bow shocks, we develop a general theory for the effects of inclination angle on the apparent shape. We propose a new two-dimensional classification scheme for bow shapes, which is based on dimensionless geometric ratios that can be estimated from observational images. The two ratios are related to the flatness of the bow’s apex, which we term *planitude* and the openness of its wings, which we term *alatitude*. We calculate the expected distribution in the planitude–atitude plane for a variety of simple geometrical and physical models: quadrics of revolution, wilkinoids, cantoids, and ancantoids. We further test our methods against numerical magnetohydrodynamical simulations of stellar bow shocks and find that the apparent planitude and alatitude measured from infrared dust continuum maps serve as accurate diagnostics of the shape of the contact discontinuity, which can be used to discriminate between different physical models. We present an algorithm that can determine the planitude and alatitude from observed bow shock emission maps with a precision of 10 to 20%.

**Key words:** circumstellar matter – hydrodynamics – stars: winds, outflows

## 1 INTRODUCTION

The archetypal bow shock is formed when a solid body moves supersonically through a compressible fluid. Terrestrial examples include the atmospheric re-entry of a space capsule, or the sonic boom produced by a supersonic jet (van Dyke 1982). In astrophysics the term bow shock is employed more widely, to refer to many different types of curved shocks that have approximate cylindrical symmetry. Instead of a solid body, astrophysical examples usually involve the interaction of *two* supersonic flows, such as the situation of a stellar wind emitted by a star that moves supersonically through the interstellar medium (van Buren & McCray 1988; Kobulnicky et al. 2010; van Marle et al. 2011; Mackey et al. 2012, 2015). In such cases, two shocks are generally produced, one in each flow. Sometimes, especially in heliospheric studies (Zank 1999; Scherer & Fichtner 2014), the term “bow shock” is reserved for the shock in the ambient medium, with the other being called the “wind shock” or “termination shock”. However, in other contexts such as colliding wind binaries (Stevens et al. 1992; Gayley 2009) such a distinction is not so useful.

A further class of astrophysical bow shock is driven by highly collimated, supersonic jets of material, such as the Herbig Haro objects (Schwartz 1978; Hartigan et al. 1987) that are powered by jets from young stars or protostars. Additional examples are seen in planetary nebulae (Phillips et al. 2010; Meaburn et al. 2013),

active galaxies (Wilson & Ulvestad 1987), and in galaxy clusters (Markevitch et al. 2002). In the jet-driven case, the term “working surface” is often applied to the entire structure comprising the two shocks plus the shocked gas in between them, separated by a *contact discontinuity*. The working surface may be due to the interaction of the jet with a relatively quiescent medium, or may be an “internal working surface” within the jet that is due to supersonic temporal variations in the flow velocity (Raga et al. 1990).

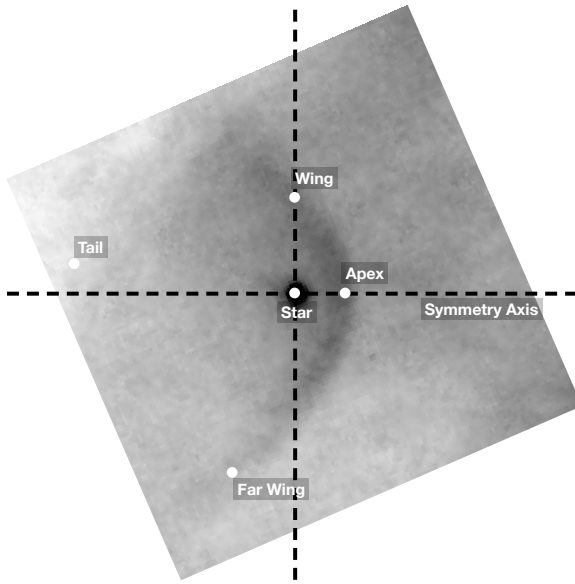
In empirical studies the relationship between these theoretical constructs and the observed emission structures is not always clear. In such cases the term “bow shock” is often used in a more general sense to refer to the entire arc of emission. In this paper, we will concentrate on *stellar bow shocks*, in which the position of the star can serve as a useful reference point for describing the bow shape. The empirical terminology that we will employ is illustrated in Figure 1. The *apex* is the point of closest approach of the bow to the star, which lies on the approximate symmetry axis, and the region around the apex is sometimes referred to as the *head* of the bow. The *wings* are the swept-back sides of the bow, which lie in a direction from the star that is orthogonal to the axis, with the *far wings* being the wing region farthest from the apex. Finally, the *tail* is the region near the axis but in the opposite direction from the apex.

Figure 2 shows an idealized schematic of how a double bow-shock shell is formed from the interaction of two supersonic streams: an *inner wind* and an *outer wind*, with the inner wind being the weaker of the two (in terms of momentum), so that the shell curves back around the inner source. The outer wind may be from another star, or may be a larger scale flow of the interstellar medium, such

\* E-mail: j.tarango@irya.unam.mx

† E-mail: w.henney@irya.unam.mx

## 2 Tarango-Yong &amp; Henney



**Figure 1.** Descriptive terminology for a stellar bow shock. The apex is the closest approach of the bow to the star, while the wings are the parts of the bow that curve back past the star.

as the *champagne flow* produced by the expansion of an H II region away from a molecular cloud (Tenorio-Tagle 1979; Shu et al. 2002; Medina et al. 2014). Alternatively, it may be due to the supersonic motion of the inner source through a relatively static medium, in which case the outer wind will not be divergent as shown in the figure but rather plane-parallel. The thickness of the shocked shells at the apex depends on the Mach number,  $\mathcal{M}$ , of the flows and the efficiency of the post-shock cooling. For sufficiently strong cooling, the post-shock cooling zone thickness is negligible and the shock can be considered isothermal. In this case, the shell thickness is of order  $\mathcal{M}^{-2}$  times the source-apex separation (Henney 2002), which can become very small for high Mach numbers. The shell thickness will tend to increase towards the wings, due to the increasing shock obliqueness, which reduces the perpendicular Mach number.

In the extreme thin-shell limit, the entire bow structure can be treated as a surface. The bow radius measured from the inner source (star) is  $R(\theta, \phi)$ , where  $\theta$  is the polar angle, measured from the star-apex axis, and  $\phi$  is the azimuthal angle, measured around that axis. Assuming cylindrical symmetry about the axis, this reduces to  $R(\theta)$ , which is illustrated in Figure 3, following Canto et al. (1996). The separation between the two sources is  $D$  and the complementary angle, as measured at the position of the outer source, is  $\theta_1$ . The minimum value of  $R(\theta)$  is the stagnation radius,  $R_0$ , which occurs at the apex ( $\theta = 0$ ). In a steady state, ram-pressure balance on the axis implies that

$$\frac{R_0}{D} = \frac{\beta^{1/2}}{1 + \beta^{1/2}}, \quad (1)$$

where  $\beta$  is the momentum ratio between the two winds. If the winds are isotropic, with inner wind mass-loss rate  $\dot{M}_w$  and terminal velocity  $V_w$ , while the outer wind has corresponding values  $\dot{M}_{w1}$  and  $V_{w1}$ , then the momentum ratio is

$$\beta = \frac{\dot{M}_w V_w}{\dot{M}_{w1} V_{w1}}. \quad (2)$$

The case where the outer wind is a parallel stream (Wilkin 1996)

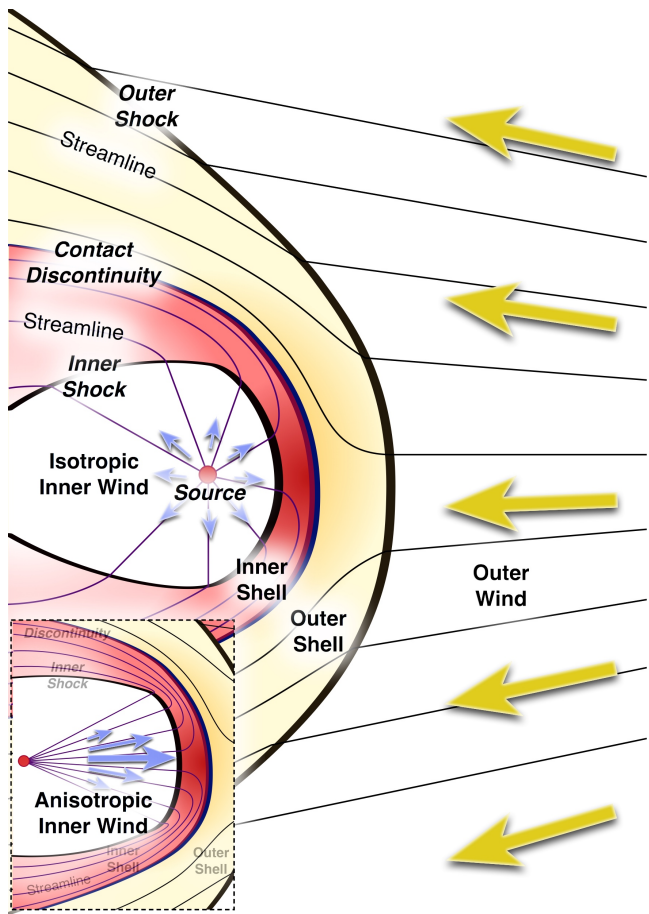


**Figure 2.** Quasi-stationary bow shock structure formed by the interaction of two supersonic winds. Lower-left inset box shows the case where the inner wind is anisotropic. The streamlines (thin lines) are drawn to be qualitatively realistic: they are straight in regions of hypersonic flow, but curved in subsonic regions, responding to pressure gradients in the shocked shells. Streamline slopes are discontinuous across oblique shocks.

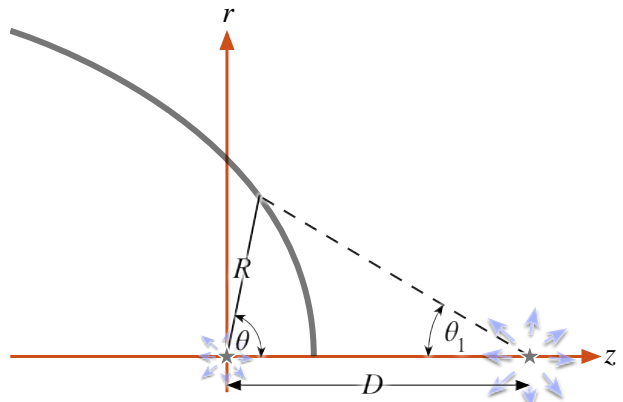


**Figure 3.** Schematic diagram of cylindrically symmetric two-wind interaction problem in the thin-shell limit, following Canto et al. (1996).

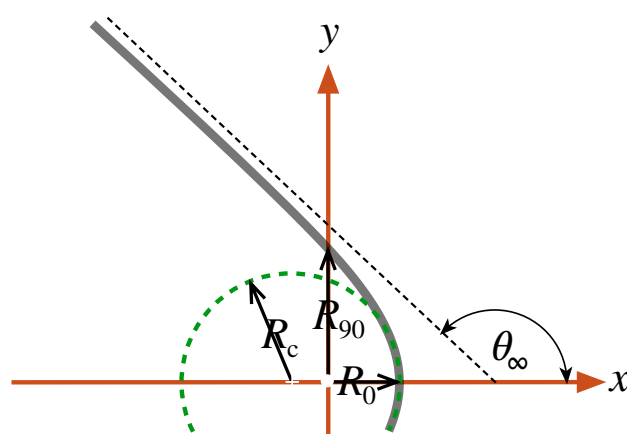


**Figure 4.** Parameters for characterizing a bow shape. Bow radius from the star, measured parallel ( $R_0$ ) and perpendicular ( $R_{90}$ ) to the symmetry axis, together with radius of curvature ( $R_c$ ) at apex and asymptotic opening angle ( $\theta_\infty$ ) of the far wings.

corresponds to the limit  $\beta \rightarrow 0$ , in which case  $D$  is no longer a meaningful parameter.

The paper is organized as follows. In § 2 we outline the geometric parameters that are necessary for describing bow shapes and introduce two dimensionless ratios: planitude and alatitude. In § 3 we derive general results for the projection of bow shapes onto the plane of the sky. In § 4 we apply the results to the simplest possible class of geometric bow models: the quadrics of revolution, which comprise spheroids, paraboloids, and hyperboloids, each of which occupies a distinct region of the planitude–alatitude plane. In § 5 we consider thin-shell hydrodynamic models for the parallel-stream case (wilkinoids) and wind-wind case (cantoids), including extension to an anisotropic inner wind (ancantoids). We calculate the location of the models in the planitude–alatitude plane as a function of the inclination of the bow shock axis to the plane of the sky. In § 6 we test our methods against the results of more realistic numerical simulations of bow shocks, including the derivation of the shape parameters from maps of infrared dust emission. In § 7 we apply our methods to example observations of proplyd bow shocks in the Orion Nebula, paying close attention to the systematic uncertainties that arise when our algorithms are applied to real data. In § 8 we summarise our results and outline how following papers will apply these ideas to a more extensive set of observations, models and numerical simulations.

## 2 PLANITUDE AND ALATITUDE OF BOW SHAPES

The stagnation radius  $R_0$  describes the linear scale of the bow shock, but in order to characterize its shape more parameters are required. To efficiently capture the diversity of bow shapes, we propose the parameters shown in Figure 4. The perpendicular radius  $R_{90}$  is the value of  $R(\theta)$  at  $\theta = 90^\circ$ , whereas  $R_c$  is the radius of curvature of the bow at the apex ( $\theta = 0$ ). For a cylindrically symmetric bow, we show in Appendix A that this is given by

$$R_c = \frac{R_0^2}{R_0 - R_{\theta\theta,0}}, \quad (3)$$

where  $R_{\theta\theta,0}$  is  $d^2R/d\theta^2$  evaluated at  $\theta = 0$ .

A fourth parameter is the asymptotic opening angle of the far wings,  $\theta_\infty$ , which is useful in the case that the wings are asymptotically conical. However, in many bow shocks the wings tend towards the asymptotic angle only slowly, making  $\theta_\infty$  difficult to measure, especially since the emission from the far wings is often weak at best. In contrast, the three radii,  $R_0$ ,  $R_{90}$ , and  $R_c$ , are straightforward to determine from observations. One simple method to estimate the radius of curvature is to make use of the Taylor expansion<sup>1</sup> of  $R(\theta)$  about the apex (with  $\theta$  in radians):

$$R(\theta) = R_0 + \frac{1}{2}R_{\theta\theta,0}\theta^2 + O(\theta^4), \quad (4)$$

so that fitting a polynomial in  $\theta^2$  to  $R(\theta)$  for  $|\theta| < \Delta\theta$  yields  $R_0$  and  $R_{\theta\theta,0}$  from the first two coefficients, and hence  $R_c$  from equation (3). Experience has shown that  $\Delta\theta = 30^\circ$  and three terms in the polynomial are good choices, where the third term is used only as a monitor (if the co-efficient of  $\theta^4$  is not small compared with  $R_0$ , then it may indicate a problem with the fit).

Since we have three radii, we can construct two independent dimensionless parameters:

$$\text{Planitude } \Pi \equiv \frac{R_c}{R_0} \quad (5)$$

$$\text{Alatitude } \Lambda \equiv \frac{R_{90}}{R_0} \quad (6)$$

and these will be the principal shape parameters that we will use in the remainder of the paper. The *planitude*,  $\Pi$ , is a measure of the flatness of the head of the bow around the apex, while the *alatitude*,  $\Lambda$ , is a measure of the openness of the bow wings. Although “planitude” can be found in English dictionaries, “atitude” is a new word that we introduce here, derived from the latin *ala* for “wing”.

Several previous studies have discussed the relation between  $R_{90}$  and  $R_0$  as a diagnostic of bow shape (for example Robberto et al. 2005; Cox et al. 2012; Meyer et al. 2016), but as far as we know, we are the first to include  $R_c$ . Robberto et al. (2005) § 4.2 use the ratios  $R_0/D$  and  $R_{90}/D$  in analyzing proplyd bow shapes in the Trapezium cluster in the center of the Orion Nebula (Hayward et al. 1994; García-Arredondo et al. 2001; Smith et al. 2005). In that case, the source of the outer wind is known, and so  $D$  is well-determined (at least, in projection), but for many bow shocks  $D$  is not known, and is not even defined for the moving-star or parallel-stream case. Cox et al. (2012) § 4.1 compare the observed shapes of bow shocks around cool giant stars with an analytic model, and use  $A$  and  $B$  for the projected values of  $R_0$  and  $R_{90}$ , respectively (see next section for discussion of projection effects). Meyer et al. (2016) § 3.2 analyze the distribution of  $R_0/R_{90}$  (the reciprocal of our  $\Lambda$ ) for hydrodynamic simulations of bow shocks around runaway OB stars.

## 3 PROJECTION ONTO THE PLANE OF THE SKY

In this section we calculate the apparent shape on the plane of the sky of the limb-brightened border of a shock or shell that is idealized as an arbitrary cylindrically symmetric surface.

<sup>1</sup> This method assumes both that  $R(\theta)$  is even (true for a cylindrically symmetric bow) and that the orientation of the axis is already known. Generalization to cases where these assumptions do not hold is discussed in Appendix E.

## 4 Tarango-Yong & Henney

### 3.1 Frames of reference

Consider body-frame cartesian coordinates  $(x, y, z)$ , where  $x$  is the symmetry axis, and spherical polar coordinates  $(R, \theta, \phi)$ , where  $\theta$  is the polar angle and  $\phi$  the azimuthal angle. Since the surface is cylindrically symmetric, it is can be specified as  $R = R(\theta)$ , so that cartesian coordinates on the surface are:

$$\mathbf{r} \equiv \begin{pmatrix} x \\ y \\ z \end{pmatrix} = \begin{pmatrix} R(\theta) \cos \theta \\ R(\theta) \sin \theta \cos \phi \\ R(\theta) \sin \theta \sin \phi \end{pmatrix}. \quad (7)$$

Suppose that the viewing direction makes an angle  $i$  with the  $z$  axis, so that we can define observer-frame coordinates  $(x', y', z')$ , which are found by rotating the body-frame coordinates about the  $y$  axis. The same vector,  $\mathbf{r}$ , expressed in the observer frame is then

$$\mathbf{r} = \begin{pmatrix} x' \\ y' \\ z' \end{pmatrix} = \mathbf{A}_y(i) \begin{pmatrix} x \\ y \\ z \end{pmatrix} = \begin{pmatrix} x \cos i - z \sin i \\ y \\ z \cos i + x \sin i \end{pmatrix}, \quad (8)$$

where the rotation matrix  $\mathbf{A}_y(i)$  is given in Appendix B. The inclination angle  $i$  is defined so that  $i = 0^\circ$  when the surface is viewed perpendicular to its axis (*side on*) and  $i = \pm 90^\circ$  when it is viewed along its axis (*end on*), with positive  $i$  when the apex points towards the observer.

The relationship between the two frames is illustrated in Figure 5. All quantities in the observer's frame are denoted by attaching a prime to the equivalent quantity in the body frame. There are two ways of interpreting the primed coordinates. On the one hand, the 3-vector  $(x', y', z')$  specifies a point in Euclidean space,  $\mathbb{R}^3$ , but an alternative interpretation is to take the 2-vector  $(x', y')$  as specifying a point in a *projective space*,  $\mathbb{P}^2$  (see, for example, § 15.6 of Penrose 2004). Each “point” in  $\mathbb{P}^2$  is equivalent to a line in  $\mathbb{R}^3$ , specifically: a line of sight that passes through the observer. Thus,  $(x', y')$  gives the celestial coordinates on the *plane of the sky*, with  $x'$  being the projected symmetry axis of the surface. We assume that the observer is located at a very large distance, relative to the size of the bow, so that all lines of sight are effectively parallel to the  $z'$  axis, with the observer at  $z' = -\infty$ . But, from the point of view of the plane of the sky, the  $z'$  coordinate is strictly irrelevant since it is a projective plane, and not a Euclidean plane. In the following, we will switch between the  $\mathbb{R}^3$  and  $\mathbb{P}^2$  interpretations as convenient, resolving ambiguity where necessary via the adjectives “Euclidean” for  $\mathbb{R}^3$  and “plane-of-sky” or “projected” for  $\mathbb{P}^2$ .

### 3.2 Unit vectors normal and tangential to the surface

We define unit vectors  $\hat{\mathbf{n}}$ ,  $\hat{\mathbf{t}}$ , such that  $\hat{\mathbf{n}}$  is normal to the surface, while  $\hat{\mathbf{t}}$  is tangent to the surface in a plane of constant  $\phi$ . For  $\phi = 0$  the surface lies in the  $xy$  plane and it is straightforward to show (Fig. 6) that in this case the unit vectors are given by

$$\hat{\mathbf{t}}_0 = \begin{pmatrix} -\cos \alpha \\ \sin \alpha \\ 0 \end{pmatrix} \quad \text{and} \quad \hat{\mathbf{n}}_0 = \begin{pmatrix} \sin \alpha \\ \cos \alpha \\ 0 \end{pmatrix}, \quad (9)$$

where  $\alpha$  is the *slope angle*, given by

$$\tan \alpha = -\frac{dy}{dx} \Big|_{R(\theta)} = \frac{1 + \omega \tan \theta}{\tan \theta - \omega} \quad (10)$$

and  $\omega$  is a dimensionless *local growth factor*:

$$\omega(\theta) = \frac{1}{R} \frac{dR}{d\theta}. \quad (11)$$

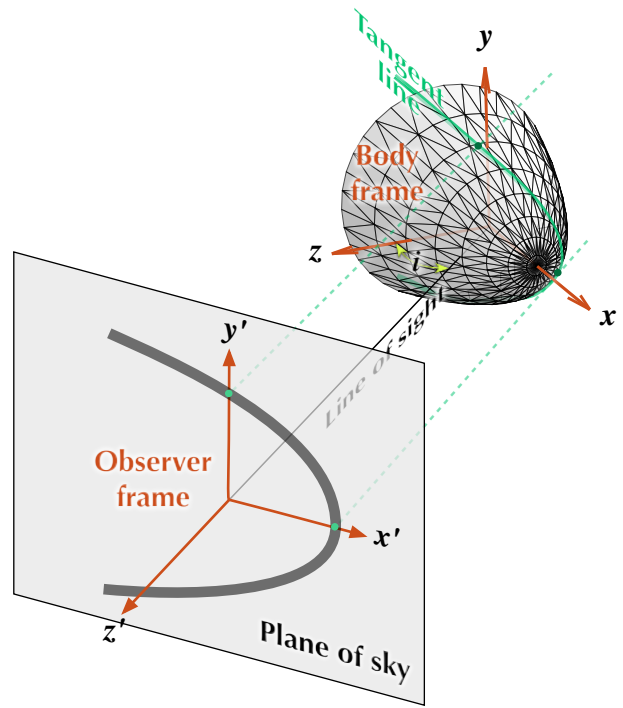


**Figure 5.** Relationship between body frame (unprimed coordinates) and observer frame (primed coordinates). Note that the plane of the sky is a projective plane, not a geometric plane in Euclidean 3-space, see discussion in text.

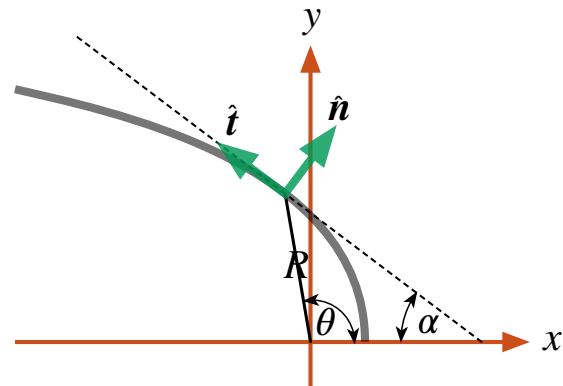


**Figure 6.** Unit vectors in the body frame that are normal and tangential to the surface  $R(\theta)$  in a plane of constant azimuth,  $\phi$ .

For general  $\phi \neq 0$ , we find  $\hat{\mathbf{n}}$  and  $\hat{\mathbf{t}}$  by rotating equations (9) around the  $x$ -axis with the matrix  $\mathbf{A}_x(\phi)$  (eq. [B5]):

$$\hat{\mathbf{n}} = \mathbf{A}_x(\phi) \hat{\mathbf{n}}_0 = \begin{pmatrix} \sin \alpha \\ \cos \alpha \cos \phi \\ \cos \alpha \sin \phi \end{pmatrix} \quad (12)$$

$$\hat{\mathbf{t}} = \mathbf{A}_x(\phi) \hat{\mathbf{t}}_0 = \begin{pmatrix} -\cos \alpha \\ \sin \alpha \cos \phi \\ \sin \alpha \sin \phi \end{pmatrix}. \quad (13)$$

### 3.3 Tangent line

The boundary on the plane of the sky of the projected surface is the locus of those lines of sight that graze the surface tangentially. This corresponds to a curved line on the surface itself, which we denote the *tangent line*, and which is defined by the condition

$$\hat{\mathbf{n}} \cdot \hat{\mathbf{z}}' = 0. \quad (14)$$

We denote by  $\phi_T$  that value of  $\phi$  that satisfies this relation for a given inclination,  $i$ , and polar angle,  $\theta$ . From equations (12, 14, B4, 10) this is

$$\sin \phi_T = -\tan i \tan \alpha = \tan i \frac{1 + \omega \tan \theta}{\omega - \tan \theta}. \quad (15)$$

From equations (7, 8) it follows that the observer-frame coordinates of the tangent line are given by

$$\begin{pmatrix} x'_T \\ y'_T \\ z'_T \end{pmatrix} = R(\theta) \begin{pmatrix} \cos \theta \cos i - \sin \theta \sin \phi_T \sin i \\ \sin \theta (1 - \sin^2 \phi_T)^{1/2} \\ \cos \theta \sin i + \sin \theta \sin \phi_T \cos i \end{pmatrix}. \quad (16)$$

Note that, in general,  $z'_T$  is not a linear function of  $x'_T$  and  $y'_T$ , so that the tangent line  $(x'_T, y'_T, z'_T)$  is not a plane curve in 3-dimensional Euclidean space,  $\mathbb{R}^3$ . However, for the projected shape  $(x'_T, y'_T)$  of the tangent line on the plane of the sky,  $\mathbb{P}^2$ , the value of  $z'_T$  does not matter (see above). The projected shape can also be described in polar form as  $R'(\theta')$ , where

$$R' = (x'^2_T + y'^2_T)^{1/2} \quad \text{and} \quad \tan \theta' = y'_T / x'_T. \quad (17)$$

Equation (15) will not have a solution for arbitrary values of  $\theta$  and  $i$ , but only when  $|\tan i \tan \alpha| < 1$ . In particular, if  $i \neq 0$ , then the tangent line only exists for  $\theta > \theta_0$  where  $\theta_0$  is the value of  $\theta$  on the tangent line's projected symmetry axis ( $\theta' = 0$ ). From equations (16, 17) it follows that  $\sin^2 \phi_T = 1$  at  $\theta = \theta_0$ , which yields the implicit equation

$$\tan \theta_0 = \frac{|\tan i| + \omega(\theta_0)}{1 - \omega(\theta_0)|\tan i|}. \quad (18)$$

In addition, if the surface is sufficiently “open” ( $\alpha \geq \alpha_{\min} > 0$  for all  $\theta$ ), then for those inclinations with  $|i| > (90^\circ - \alpha_{\min})$  the tangent line does not exist for any value of  $\theta$ . In other words, when the viewing angle is sufficiently close to face-on, the projected surface has no “edge” and will no longer look like a bow shock to the observer.

After completing this work, it was brought to our attention that the principal results of this section had already been derived in Appendix B of the PhD thesis Wilkin (1997). For instance, Wilkin's equation (8) is equivalent (apart from differences in notation) to our equation (15).

### 3.4 Characteristic radii on the plane of the sky

In order to compare the shell shape given by  $R(\theta)$  with observations, it is convenient to define the following apparent radii in the observer frame:  $R'_0$  and  $R'_{90}$ . These are projected distances of the shell tangent line from the origin. The first is measured in the direction of the symmetry axis, and the second in a perpendicular direction. More concretely  $R'_0 = x'_T(y'_T = 0)$  and  $R'_{90} = y'_T(x'_T = 0)$ . From equations (15) and (16) we find that:

$$R'_0 = R(\theta_0) \cos(\theta_0 + i) \quad (19)$$

Where  $\theta_0$  is the solution of equation (18), and

$$R'_{90} = R(\theta_{90}) \sin \theta_{90} \left(1 - \sin^2(\phi_T(\theta_{90}))\right)^{1/2} \quad (20)$$

Where  $\theta_{90}$  is the solution of the implicit equation:

$$\cot \theta_{90} = \frac{1 - (1 + \omega(\theta_{90})^2 \sin^2 2i)^{1/2}}{2\omega(\theta_{90}) \cos^2 i} \quad (21)$$

The projected alatitude (see § 2) is then given by  $\Lambda' = R'_{90}/R'_0$ .

Similarly, the projected planitude is  $\Pi' = R'_c/R'_{90}$ , where  $R'_c$  is found by applying the equivalent of equation (3) for primed quantities:

$$R'_c = \frac{(R'_0)^2}{R'_0 - R'_{\theta' \theta', 0}}. \quad (22)$$

### 3.5 Line-of-sight velocities on the tangent line

Motions in a thin shocked shell will be predominantly tangential to the shell surface. In addition, for the particular case of wind-wind bowshocks, the flow in each azimuthal slice can be shown to be independent (Wilkin 2000), which implies that the shell velocity is parallel to  $\hat{\mathbf{t}}$ . The projected line-of-sight shell velocity is therefore

$$v_{\text{los}} = (\hat{\mathbf{t}}' \cdot -\hat{\mathbf{z}}') v_{\parallel}(\theta) = \frac{v_{\parallel}(\theta)(1 + \omega^2)^{1/2} \sin i}{\sin \theta - \omega \cos \theta}, \quad (23)$$

where  $v_{\parallel}(\theta)$  is the gas velocity along the shell and the standard sign convention has been adopted such that velocities away from the observer are deemed positive.

## 4 QUADRICS OF REVOLUTION

For an arbitrary surface of revolution, application of equations (15, 16) to determine the projected shape of the tangent line is not straightforward and in general requires numerical techniques. However, analytical results can be found for the important class of surfaces known as *quadratics of revolution* (Goldman 1983; Gfrerrer & Zsombor-Murray 2009), which are formed by rotating a conic section plane curve about its symmetry axis. Examples are the sphere, spheroids (oblate and prolate), and right circular paraboloids and hyperboloids.<sup>2</sup> We ignore the degenerate cases of cylinders, cones, and pairs of parallel planes. While mathematically simple, these quadratics are sufficiently flexible that they can provide a useful approximation to more complex bow shock shapes.

The shape of the quadric curves in the  $xy$  plane ( $\phi = 0$ ) are shown in Figure 7(a) and (b) for the ellipse and hyperbola case, respectively. The conic section itself is fully described by two lengths,  $a$  and  $b$ , which are the semi-axes.<sup>3</sup> However, the curve can be translated along the  $x$  axis to an arbitrary point with respect to the star, so that the apex distance  $R_0$  has no necessary relation to  $a$  or  $b$  and therefore the star/bow combination requires *three* independent lengths for its specification. The displacement  $x_0$  from the star to the “center” of the conic section is

$$x_0 = R_0 - \sigma a \quad \text{with} \quad \sigma = \begin{cases} +1 & \text{ellipse} \\ -1 & \text{hyperbola} \end{cases}. \quad (24)$$

For hyperbolas the center is “outside” of the bow and  $x_0$  is always

<sup>2</sup> We consider only the case of a single sheet of a 2-sheet hyperboloid or paraboloid, since these are the versions that resemble a bow, whereas the 1-sheet versions resemble the waist of an hourglass.

<sup>3</sup> Note that we do not require that  $a > b$ , so either  $a$  or  $b$  may be the semi-major axis.

## 6 Tarango-Yong &amp; Henney

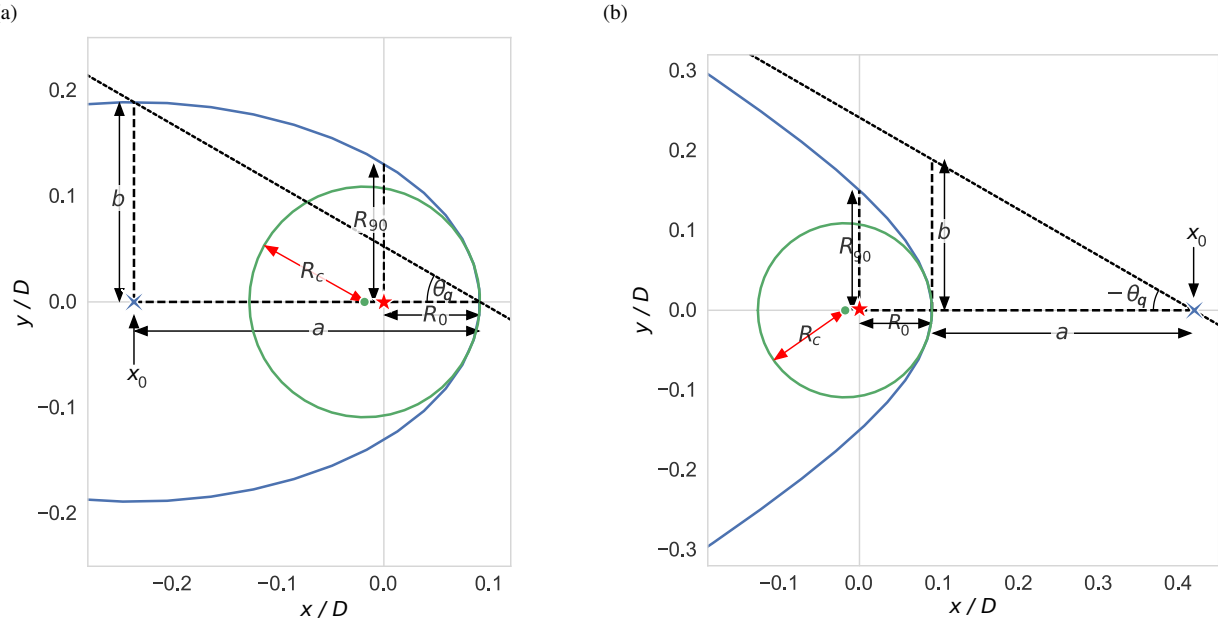


**Figure 7.** Example off-center conic sections that can form quadrics of revolution: (a) ellipse, (b) hyperbola. The relationship is shown between the conic section parameters  $a$ ,  $b$ ,  $\theta_Q$  and the bowshock characteristic radii  $R_0$ ,  $R_{90}$ ,  $R_c$ , as defined in Fig. 4. The origin (center of the weaker flow) is indicated by a red star, the center of curvature of the apex of the bow shock is indicated by a green dot, and the geometric center of the conic section is indicated by a blue cross, which is offset by  $x_0$  from the origin. Note that  $R_0$ ,  $R_{90}$ ,  $R_c$ ,  $a$ , and  $b$  are all lengths and are always positive, whereas  $x_0$  is a displacement and may be positive or negative.

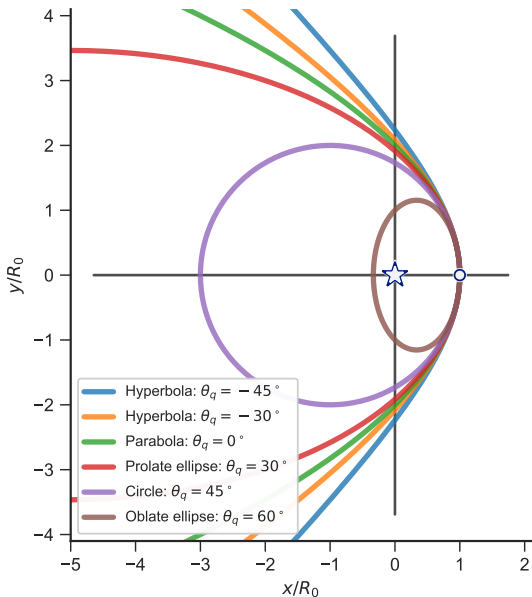


**Figure 8.** Example of a family of conic sections, all with the same planitude (flatness at apex, marked by white dot):  $\Pi = R_c/R_0 = 2$ . The quadric angle,  $\theta_Q$ , varies over the family (see text), with lower values of  $\theta_Q$  giving larger values of the alatitude,  $\Lambda = R_{90}/R_0$ , meaning more open wings. Different values of  $\Pi$  can be achieved for the exact same quadrics by sliding them along the  $x$ -axis, which will also change the axis scales since these are normalized by  $R_0$ .

positive, whereas for ellipses the center is “inside” the bow and  $x_0$  is usually negative, except when  $a < R_0$  (see Figure 7).

A general parametric form<sup>4</sup> for the  $xy$  coordinates of the quadrics (in the  $\phi = 0$  plane, and with the star at the origin) as a function of  $t = [0, \pi]$  is then

$$\begin{aligned} x &= x_0 + \sigma a C(t) \\ y &= b S(t) \end{aligned} \quad (25)$$

where

$$S, C = \begin{cases} \sin, \cos & \text{ellipse} \\ \sinh, \cosh & \text{hyperbola} \end{cases} \quad (26)$$

Except for the circle case ( $\sigma = +1$ ,  $a = b$ ), the parametric variable  $t$  is not actually an angle in physical space. Instead, the polar form of the bow shape  $R(\theta)$  must be found by substituting equations (25) into  $\theta = \tan^{-1} y/x$  and  $R = (x^2 + y^2)^{1/2}$ .

The type of quadric surface can be characterized by the *quadric parameter*:

$$Q \equiv \sigma \frac{b^2}{a^2}, \quad (27)$$

where  $Q < 0$  corresponds to open surfaces (hyperboloids) and  $Q > 0$  corresponds to closed surfaces (oblate spheroids with  $Q > 1$  and prolate spheroids with  $Q < 1$ ). Special cases are the sphere ( $Q = 1$ ) and the paraboloid ( $Q = 0$ ). Alternatively, one can define a *quadric angle*:

$$\theta_Q = \sigma \tan^{-1}(b/a), \quad (28)$$

which is marked in Figure 7. In the case of hyperboloids, the

<sup>4</sup> The special case of the parabola needs to be treated differently, see Appendix C.

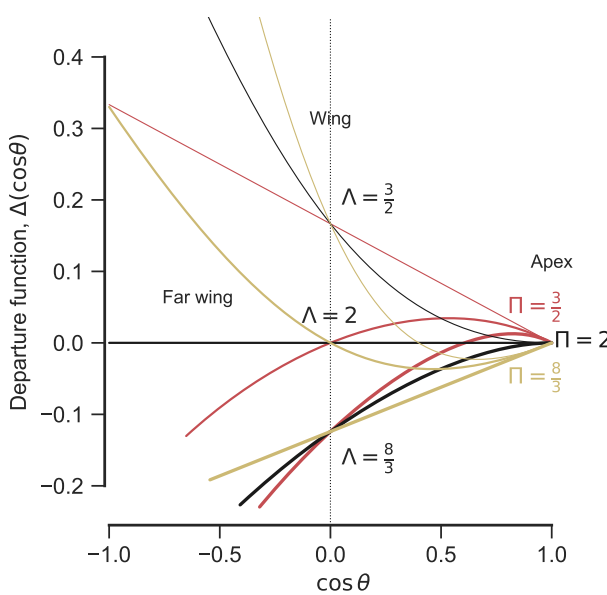


**Figure 9.** Parabolic departure function,  $\Delta(\cos \theta)$ , for conic sections with different planitude and alatitude, centered on that of the confocal parabola,  $(\Pi, \Lambda) = (2, 2)$ , which has  $\Delta(\cos \theta) = 0$ . Planitude (shown by different line colors) determines the slope of  $\Delta$  at the apex,  $\cos \theta = 1$ . Alatitude (shown by different line widths) determines the value of  $\Delta$  at  $\cos \theta = 0$ . All conics with  $\Pi = \Lambda$  have departure functions that are straight lines.

asymptotic opening angle of the wings (§ 2 and Fig. 4) is  $\theta_\infty = \pi + \theta_Q$  (note that  $\theta_Q < 0$  in this case), and the minimum slope angle is  $\alpha_{\min} = |\theta_Q|$ , see discussion following equation (18).

The set of parameters  $(Q, a, x_0)$  are then sufficient to characterize the star/bow combination, where  $a$  is the quadric scale and  $x_0$  is its center displacement from the star. However, we can also characterize the star/bow by  $(R_0, \Pi, \Lambda)$ , where  $R_0$  is the star-apex distance, and  $\Pi$  and  $\Lambda$  are the planitude and alatitude, see § 2. We now derive the equivalences between these two descriptions. The apex radius of curvature for a conic section is

$$R_c = \frac{b^2}{a} = a|Q|, \quad (29)$$

whereas the perpendicular radius,  $R_{90}$ , is the value of  $y$  when  $x = 0$ , which can be found from equations (24, 25) as

$$R_{90}^2 = Q(a^2 - x_0^2). \quad (30)$$

Combining equations (5, 6, 24, 27–30) yields

$$R_0 = x_0 + \sigma a \quad (31)$$

$$\Pi = \frac{aQ}{a + \sigma x_0} \quad (32)$$

$$\Lambda = \left( Q \frac{a - \sigma x_0}{a + \sigma x_0} \right)^{1/2} \quad (33)$$

with  $\sigma = \text{sgn } Q$ . It also follows that the quadric parameter in terms of the planitude and alatitude is

$$Q = 2\Pi - \Lambda^2 \quad (34)$$

Hence, it is the sign of  $2\Pi - \Lambda^2$  that determines  $\sigma$  and whether a quadric is a spheroid or a hyperboloid. For example, for a constant

planitude,  $\Pi$ , we can have a family of different quadric types, with varying alatitude,  $\Lambda$ , that increases from oblate, through prolate and paraboloid, to hyperboloid, as illustrated in Figure 8.

#### 4.1 Parabolic departure function

The special case of confocal conic sections ( $\Lambda = \Pi$ ) can be written in polar form as

$$R(\theta) = R_0 \frac{1 + e}{1 + e \cos \theta} \quad (35)$$

where  $e = (1 - Q)^{1/2}$  is the *conic eccentricity*. For the confocal parabola ( $e = 1$ ), the dimensionless reciprocal radius is therefore  $R_0/R(\theta) = \frac{1}{2}(1 + \cos \theta)$ , which suggests the following form for a *departure function* that measures the difference between a given shape  $R(\theta)$  and the parabola:

$$\Delta(\cos \theta) = \frac{R_0}{R(\theta)} - \frac{1}{2}(1 + \cos \theta). \quad (36)$$

From equations (35) and (36) it is clear that  $\Delta$  is a linear function of  $\cos \theta$  for other confocal conics, being positive for ellipses ( $e < 1$ ) and negative for hyperbolae ( $e > 1$ ). Examples are shown in Figure 9 for a grid of 9 conics centered on the confocal parabola, with  $(\Pi, \Lambda)$  ranging from  $3/4$  to  $4/3$  of  $(2, 2)$ . The hyperbolae have negative values of  $\Delta$  in the far wings, with tracks that end at  $\cos \theta_\infty$ .

Strictly speaking, the departure function is redundant if one is interested in only conic sections, since they are fully determined by  $\Pi$  and  $\Lambda$ . Nonetheless, as we will show in following sections, it is a useful tool for studying general  $R(\theta)$ , being very sensitive to small variations in the shape.

#### 4.2 Plane-of-sky projection of quadric surfaces

We now apply the machinery of § 3 to find the projected shape of a quadric bow on the plane of the sky. The intrinsic 3D shape of the shell is given by rotating equations (25) about the  $x$ -axis, but it is more convenient to first transform to a reference frame where the origin is at the center of the conic section:

$$(X, Y, Z) = (x - x_0, y, z). \quad (37)$$

In this new frame, the quadric shape is

$$\begin{aligned} X &= a C(t) \\ Y &= b S(t) \cos \phi \\ Z &= b S(t) \sin \phi \end{aligned} \quad (38)$$

The azimuth of the tangent line as a function of inclination and parametric variable is then found from equations (10, 15) to be

$$\sin \phi_T = \frac{b C(t)}{a S(t)} \tan i. \quad (39)$$

Combining equations (8, 38, 39) gives the observer-frame cartesian plane-of-sky coordinates of the tangent line:

$$\begin{aligned} X'_T &= \frac{C(t)}{a \cos i} (a^2 \cos^2 i + \sigma b^2 \sin^2 i) \\ Y'_T &= b S(t) \left( 1 - \frac{b^2 C^2(t)}{a^2 S^2(t)} \tan^2 i \right)^{1/2} \end{aligned} \quad (40)$$

We wish to show that this projected shape is a conic section of the same variety (ellipse or hyperbola) as the one that generated the

## 8 Tarango-Yong &amp; Henney

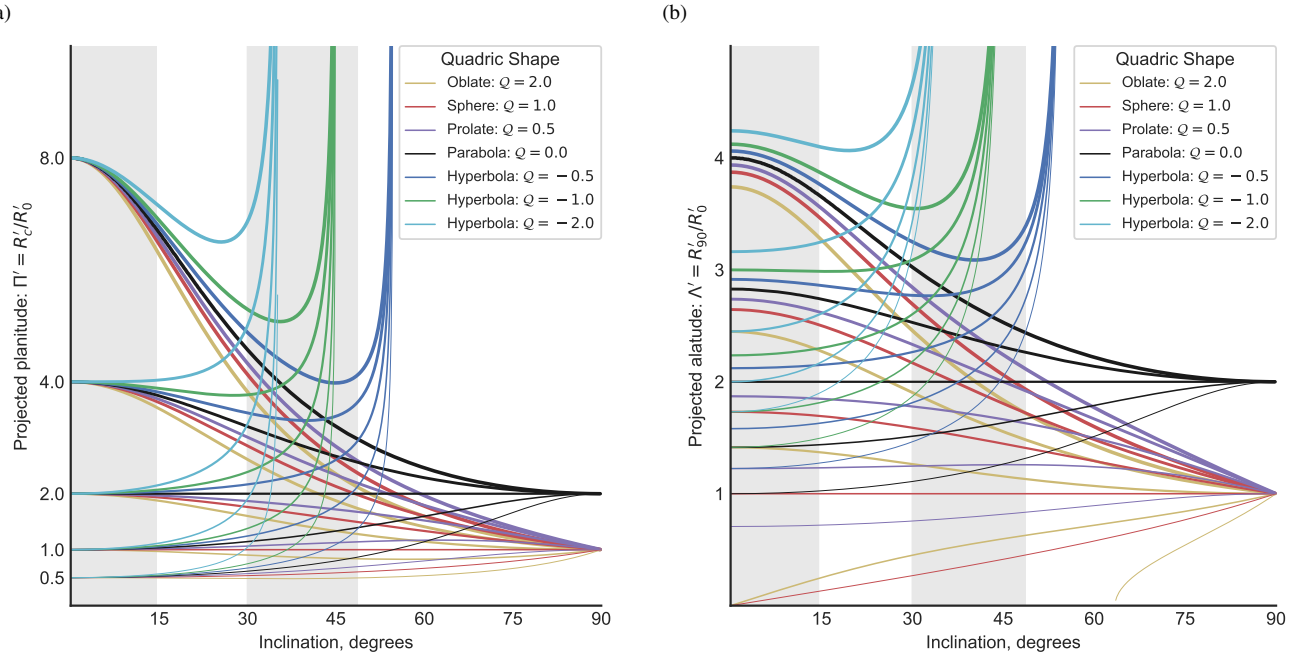


**Figure 10.** Effects of projection on quadrics of revolution: variation with inclination,  $|i|$ , of bow size and shape. Different line colors correspond to varying quadric parameter,  $Q$ , (see key), while variation in line width corresponds to variation in the ‘true’ planitude,  $\Pi$ , or apex radius of curvature. Vertical gray rectangles show quartiles of  $|\sin i|$ , which will be equally populated for an isotropic distribution of orientations. (a) Projected planitude:  $\Pi'$ . (b) Projected alatitude,  $\Lambda'$ .

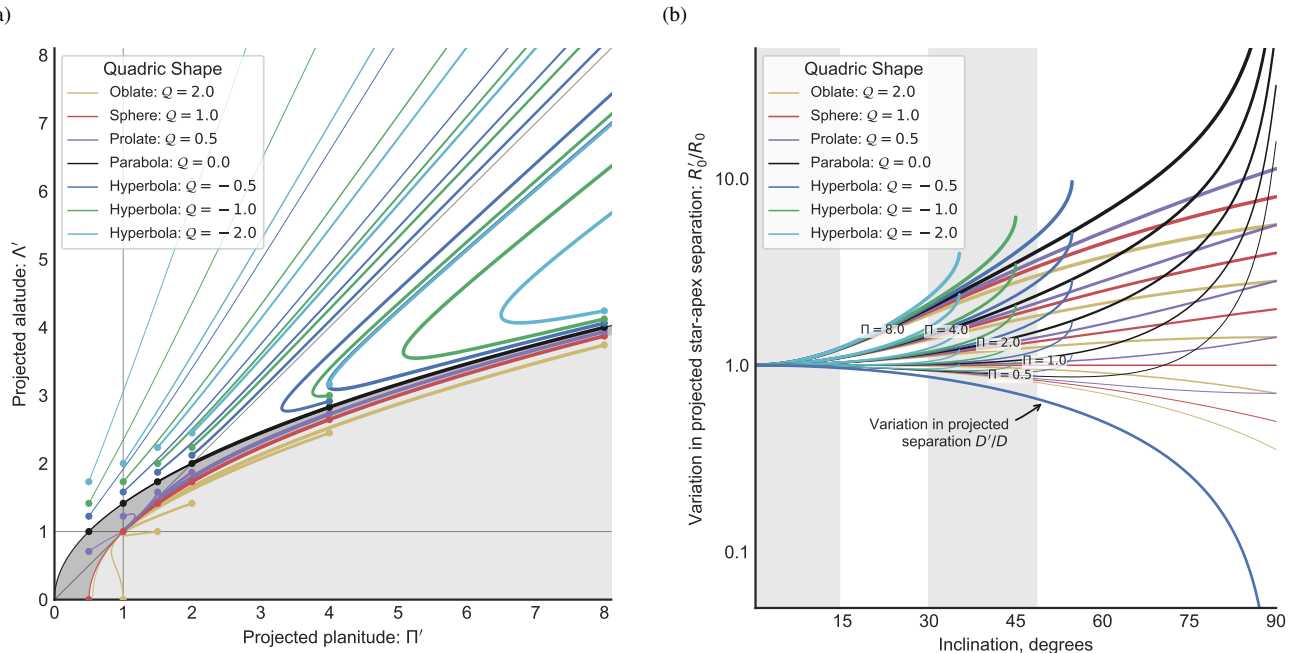


**Figure 11.** As Figure 10, but (a) diagnostic planitude–alatitude diagram:  $\Lambda'$  versus  $\Pi'$ , and (b) projected/true star-apex distance:  $R'_0/R_0$  versus  $|i|$ . In (a), shading indicates different classes of quadrics: hyperboloids (white), prolate spheroids (dark gray), and oblate spheroids (light gray), with the limiting case of paraboloids shown by the thin black line.

original quadric. If this *were* true, then it would be possible to write the plane-of-sky coordinates as

$$\begin{aligned} X'_T &= a' C(t') \\ Y'_T &= b' S(t'). \end{aligned} \quad (41)$$

Comparing equations (40) and (41), we find after some algebra that the two forms for  $(X'_T, Y'_T)$  are indeed consistent, with the equivalences:

$$a' = a f_{Q,i} \cos i \quad (42)$$

$$b' = b \quad (43)$$

$$t' = C^{-1} [f_{Q,i} C(t)], \quad (44)$$

where for convenience we define the quadric projection factor:

$$f_{Q,i} = (1 + Q \tan^2 i)^{1/2}. \quad (45)$$

This demonstrates the original claim that the projected shape is also a conic section, which means that we can re-use the previous equations (31–34) with primed quantities substituted for unprimed ones. From equations (27, 42, 43) it follows that the quadric parameter of the projected shape is

$$Q' = \frac{Q}{f_{Q,i}^2 \cos^2 i}. \quad (46)$$

Finally, we transform the projected reference frame back to be centered on the star again:

$$(x'_T, y'_T) = (X'_T + x'_0, Y'_T), \quad (47)$$

where the projected quadric displacement  $x'_0$  follows from simple foreshortening:

$$x'_0 = x_0 \cos i. \quad (48)$$

The projection of the apex distance then follows from the primed version of equation (31) as

$$\frac{R'_0}{R_0} = \cos i \left[ 1 + \frac{\Pi}{Q} (f_{Q,i} - 1) \right] \quad (49)$$

and the projected planitude and alatitude can be calculated from equations (32, 34, 42, 46) as

$$\Pi' = \frac{\Pi}{(R'_0/R_0) f_{Q,i} \cos i} \quad (50)$$

$$\Lambda' = (2\Pi' - Q')^{1/2}. \quad (51)$$

These are all shown in Figures 10 and 11 for a variety of quadric parameter  $Q$  (line color) and true planitude  $\Pi$  (line thickness). The projected planitude and alatitude (Fig. 10) behave in a qualitatively similar fashion. Whatever the true values of  $\Pi$  and  $\Lambda$ , all spheroids ( $Q > 0$ ) tend towards  $\Pi' = 1$  and  $\Lambda' = 1$  as the inclination increases towards  $90^\circ$ . This is because when the spheroid is oriented edge-on, we see its circular cross-section. Hyperboloids behave differently: although  $\Pi'$  and  $\Lambda'$  initially decrease with increasing inclination (for true  $\Pi > 2$ ), they turn around and increase again as  $|i|$  approaches the critical value  $i_{\text{crit}} = 90^\circ - |\theta_Q|$ . For  $|i| > i_{\text{crit}}$  the tangent line does not exist (see § 3.3) because the line of sight is “inside” the asymptotic cone of the far wings (with opening half angle  $\alpha_{\min} = |\theta_Q|$ ), and so no limb-brightened shell would be visible.<sup>5</sup> For paraboloids and

<sup>5</sup> As illustrated in Figure 8 of Graham et al. (2002), the isophotal emission contours are elliptical in such a case (assuming cylindrical symmetry) and no curved bow shape is apparent. Deviations from cylindrical symmetry *can* result in a curved emission arc, even for this no-tangent case (Graham et al.’s Fig. 9), but that is beyond the scope of this paper.

spheroids,  $\alpha_{\min} = 0$ , which means that the tangent line exists for all viewing angles.

In Figure 11a, we show the inclination-dependent tracks of the quadrics in the diagnostic  $\Pi' - \Lambda'$  plane of projected alatitude versus projected planitude. The true planitude and alatitude, which are seen for an edge-on viewing angle  $i = 0^\circ$ , are marked by filled circles. The zones corresponding to each class of quadric (oblate spheroid, prolate spheroid, or hyperboloid) are marked by gray shading, and it can be seen that the tracks never cross from one zone to another. The convergence of all the spheroid tracks on the point  $(\Pi', \Lambda') = (1, 1)$  is apparent, as is the divergence of the hyperboloid tracks towards  $(\Pi', \Lambda') = (+\infty, +\infty)$ , whereas the paraboloids, by contrast, converge on the point  $(\Pi', \Lambda') = (2, 2)$ . Two special cases are the confocal paraboloid and the concentric sphere,<sup>6</sup> with true planitude and alatitude  $(\Pi, \Lambda) = (2, 2)$  and  $(1, 1)$ , respectively, which are the only quadrics whose apparent shape remains identical for all inclination angles.

Figure 11b shows how the apparent star-apex separation varies with inclination. For moderate inclinations,  $|i| < 30^\circ$ , this depends primarily on the true planitude  $\Pi$ , with very little influence of the quadric parameter  $Q$ . For  $\Pi > 1$ , the separation increases with  $|i|$ , whereas for  $\Pi < 1$  it decreases slightly. Note, however, that for cases where the projected distance to the source of the external flow,  $D'$ , can be measured, then  $R'_0/D'$  is always an increasing function of  $|i|$ . For larger inclinations,  $|i| > 30^\circ$ , the strands for different  $Q$  begin to separate, with hyperbolae showing the strongest increase of  $R'_0$  with  $|i|$ .

A complementary view of the effects of projection is shown in Figure 12, which shows “snapshots” of  $(\Pi', \Lambda')$  for a sequence of 6 values of the inclination, equally spaced in  $|\sin i|$ , so that each panel is equally likely for an isotropic distribution of orientations. The distribution of the true  $\Pi$  and  $\Lambda$  are each assumed to be uniform on the range  $[0.5, 4.5]$ , giving a uniformly filled square of values for  $|i| = 0$ , which becomes increasingly distorted as  $|i|$  increases. The color scale represents  $Q$  and the symbol size is proportional to  $R'_0/R_0$ . It can be seen that the points tend to cluster closer and closer to the diagonal,  $\Lambda' = \Pi'$ , as the inclination increases, and that the points just below this line tend to have the largest values of  $R'_0/R_0$ . The green shaded region shows the zone of true  $\Lambda, \Pi$  for hyperboloids where the tangent lines still exists for that value of  $|i|$ . This becomes smaller and smaller as  $|i|$  increases, which explains why the hyperboloid zone becomes increasingly depopulated: all quadrics that lay above this region when  $i = 0^\circ$  will no longer be visible as a bow for this value of  $|i|$ . Note that this figure is merely illustrative of the qualitative effects of projection, since in reality there is no particular reason to expect a uniform distribution in true  $\Pi$  and  $\Lambda$ .

## 5 THIN-SHELL BOW SHOCK MODELS

More physically realistic examples of bow shapes are provided by steady-state hydrodynamic models for the interaction of hypersonic flows in the thin-shell limit. The classic examples are the solutions for the wind-parallel stream and wind-wind problems (see § 1) of Canto et al. (1996, hereafter CRW), where it is assumed that the two shocks are highly radiative and that the post-shock flows are perfectly mixed to form a single shell of negligible thickness. In this

<sup>6</sup> So named because the star is at the focus of the parabola, or the center of the sphere.

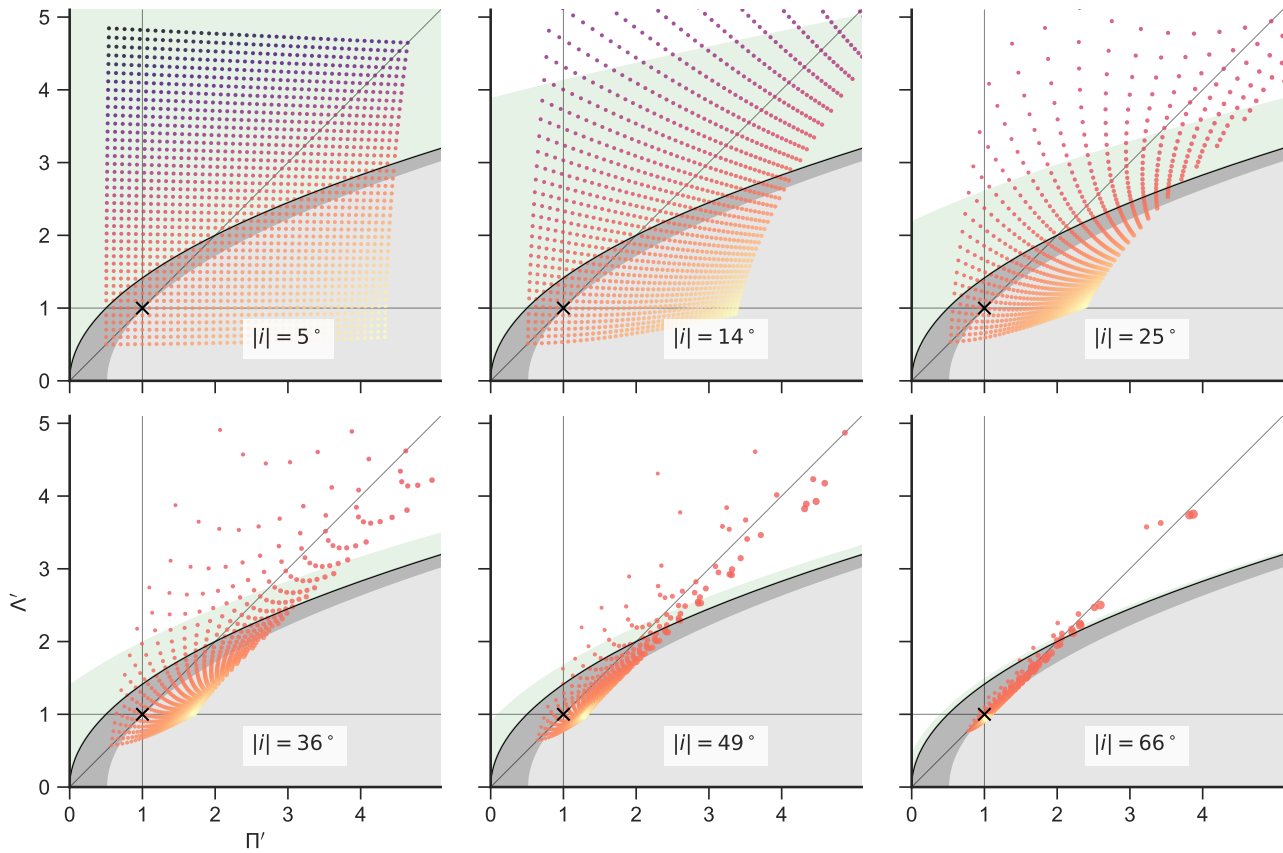


**Figure 12.** Variation with inclination angle of the apparent shape of quadric bows with true planitude and alatitude that are uniformly distributed over the ranges  $\Pi = [0.5, 4.5]$ ,  $\Lambda = [0.5, 4.5]$ . Panels show the apparent  $(\Pi', \Lambda')$  as the inclination is increased through uniform intervals in  $|sin i|$ . Symbol color represents the quadric parameter,  $Q$ , increasing from dark blue, through orange, to yellow. Symbol size is proportional to the increase in apparent star-apex distance,  $R'_0/R_0$ .

approximation, the shape of the shell is found algebraically by CRW from conservation of linear and angular momentum, following an approach first outlined in Wilkin (1996). For the wind–stream case, the resulting bow shape was dubbed *wilkinoid* by Cox et al. (2012) and has the form:

$$R(\theta) = R_0 \csc \theta (3(1 - \theta \cot \theta))^{1/2}. \quad (52)$$

For the wind–wind case, a family of solutions are found that depend on the value of  $\beta$ , the wind momentum ratio,<sup>7</sup> see Figure 3, equations (1, 2), and surrounding discussion in § 1. We propose that these shapes be called *cantoids*. The exact solution for the cantoid shapes (eqs. [23, 24] of CRW) is only obtainable in implicit form, but an approximate explicit solution (eq. [26] of CRW) is very accurate for  $\beta \leq 0.1$ . The wilkinoid shape corresponds to the  $\beta \rightarrow 0$  limit of the cantoids. Note that CRW employ cylindrical polar coordinates,  $z$  and  $r$ , see our Figure 3, and we follow this usage for the thin-shell models discussed in this section. CRW’s  $z$  axis corresponds to the cartesian  $x$  axis used in sections 3 and 4 of the current paper, while the  $r$  axis corresponds to  $y$  when  $\phi = 0$ .

A generalization of the cantoids to the case of an anisotropic<sup>8</sup>

inner wind is developed next, giving rise to what we call *ancantoids*, which depend on an anisotropy index,  $k$ , in addition to  $\beta$ .

### 5.1 Bow shocks from anisotropic wind–wind interactions

We wish to generalize the results of Canto et al. (1996, CRW) to the case where the inner wind is no longer isotropic, but instead has a density that falls off with angle,  $\theta$ , away from the symmetry axis. Specifically, at some fiducial spherical radius,  $R_0$ , from the origin, the wind mass density is given by

$$\rho(R_0, \theta) = \begin{cases} \rho_0 \cos^k \theta & \text{for } \theta \leq 90^\circ \\ 0 & \text{for } \theta > 90^\circ \end{cases}, \quad (53)$$

where  $\rho_0$  is the density on the symmetry axis and  $k \geq 0$  is an *anisotropy index*. The wind velocity is still assumed to be constant and the wind streamlines to be radial, so the radial variation of density at each angle is  $\rho(R, \theta) = \rho(R_0, \theta)(R/R_0)^{-2}$  and the wind mass loss rate and momentum loss rate per solid angle both have the same  $\cos^k \theta$  dependence as the density. Examples are shown in Figure 13 for a variety of different values of  $k$ . As  $k$  increases, the wind becomes increasingly jet-like.

Our primary motivation for considering such an anisotropic wind is the case of the Orion Nebula proplyds and their interaction with the stellar wind of the massive star  $\theta^1$  Ori C (García-Arredondo

<sup>7</sup> By always placing the weaker of the two winds at the origin, it is only necessary to consider  $\beta \leq 1$ .

<sup>8</sup> Note that the wind anisotropy axis must be aligned with the star–star axis to maintain cylindrical symmetry.

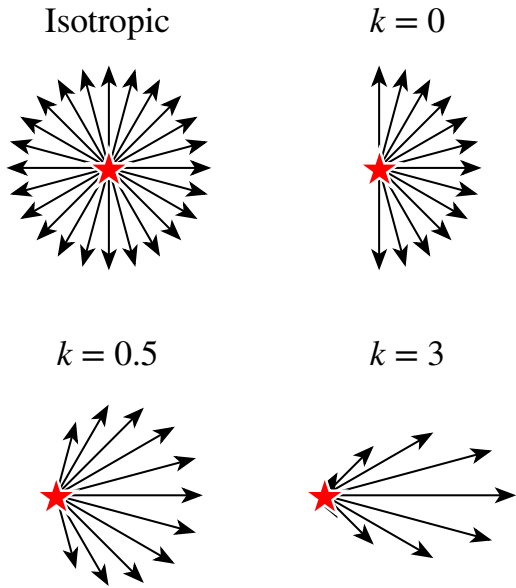


**Figure 13.** Schematic diagram of wind flow patterns in isotropic and non-isotropic cases for different values of the anisotropy index,  $k$ . Arrow length represents the wind momentum loss rate per solid angle.

et al. 2001). The inner “wind” in this case is the transonic photoevaporation flow away from a roughly hemispherical ionization front, where photoionization equilibrium, together with monodirectional illumination of the front, implies that the ionized hydrogen density,  $n$ , satisfies  $n^2 \propto \cos \theta$ , which is equivalent to  $k = 0.5$  in equation (53). Since the primary source of ionizing photons is the same star that is the source of the outer wind, it is natural that the inner wind’s axis should be aligned with the star–star axis in this case. For other potential causes of wind anisotropy (for instance, bipolar flow from an accretion disk), there is no particular reason for the axes to be aligned, so cylindrical symmetry would be broken. Nevertheless, we calculate results for general  $k$  with aligned axes, so as to provide a richer variety of cylindrically symmetric bow shock shapes than are seen in the cantoids.

The general solution for the bow shock shape,  $R(\theta)$ , in the CRW formalism is

$$R(\theta) = \frac{j_w + j_{w1}}{(\dot{\Pi}_{wr} + \dot{\Pi}_{wr1}) \cos \theta - (\dot{\Pi}_{wz} + \dot{\Pi}_{wz1}) \sin \theta} \quad (54)$$

where  $\dot{\Pi}_{wr}$ ,  $\dot{\Pi}_{wz}$ ,  $j_w$  are the accumulated linear radial momentum, linear axial momentum, and angular momentum, respectively, due to the inner wind emitted between the axis and  $\theta$ . The equivalent quantities for the outer wind have subscripts appended with “1”. The inner wind momenta for our anisotropic case (replacing CRW’s eqs. [9, 10]) are:

$$\begin{aligned} \dot{\Pi}_{wz} &= \frac{k+1}{2(k+2)} \dot{M}_w^0 V_w \max \left[ (1 - \cos^{k+2} \theta), 1 \right] \\ \dot{\Pi}_{wr} &= (k+1) \dot{M}_w^0 V_w I_k(\theta) \end{aligned} \quad (55)$$

where

$$\dot{M}_w^0 = \frac{2\pi}{k+1} r_0^2 \rho_0 V_w \quad (56)$$

## Bow shock shapes 11

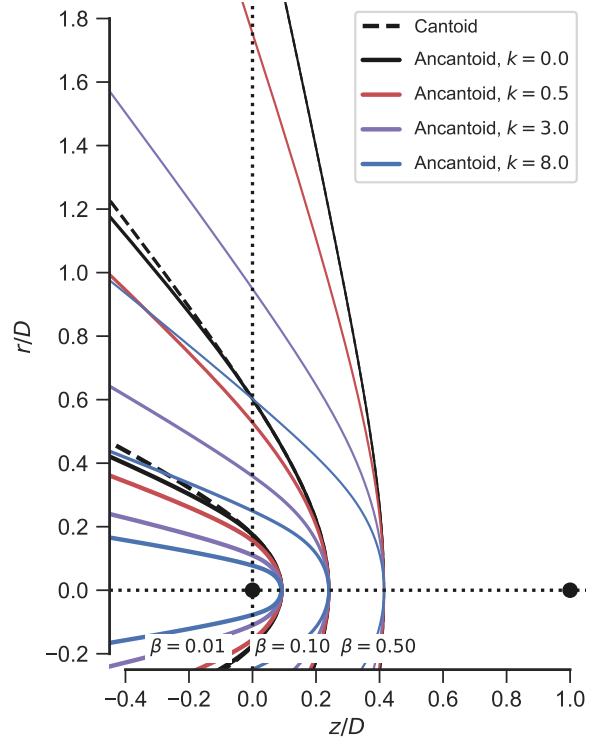


**Figure 14.** Bow shock shapes for interacting winds in the thin-shell approximation: cantoids and ancantoids. Coordinates are normalized by  $D$ , the distance between the two wind sources, which are indicated by black dots on the axis. The weaker source is at  $(0, 0, 0)$  and the stronger source is at  $(1, 0, 0)$ . Results are shown for different values of the wind momentum ratio,  $\beta$  (different line widths), and for the case where the weaker wind is isotropic (black lines) or anisotropic (colored lines).

is the total mass-loss rate of the inner wind. The integral

$$I_k(\theta) = \int_0^{\max(\theta, \pi/2)} \cos^k \theta \sin^2 \theta d\theta \quad (57)$$

has an analytic solution in terms of the hypergeometric function,  ${}_2F_1(-\frac{1}{2}; \frac{1+k}{2}; \frac{3+k}{2}; \cos^2 \theta)$ , but is more straightforwardly calculated by numerical quadrature. The angular momentum of the inner wind about the origin is  $\dot{J}_w = 0$  because it is purely radial. The outer wind momenta are unchanged from the CRW case, but are given here for completeness:

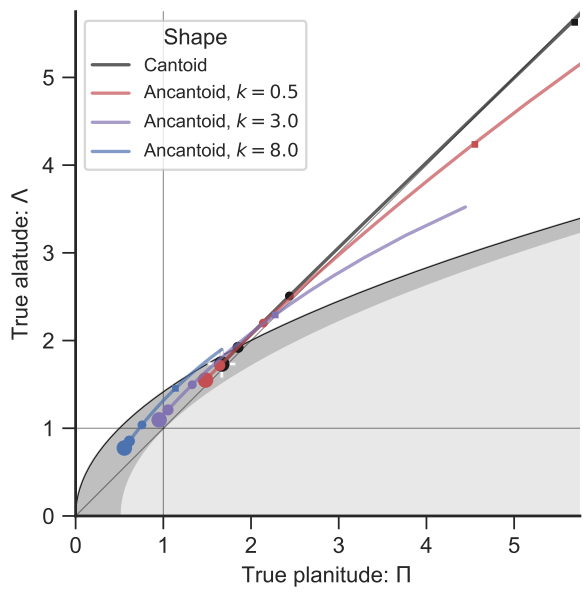
$$\begin{aligned} \dot{\Pi}_{wz1} &= -\frac{\dot{M}_w^0 V_w}{4} \sin^2 \theta_1 \\ \dot{\Pi}_{wr1} &= \frac{\dot{M}_w^0 V_w}{4} (\theta_1 - \sin \theta_1 \cos \theta_1) \\ \dot{J}_{w1} &= \frac{\dot{M}_w^0 V_w}{4} (\theta_1 - \sin \theta_1 \cos \theta_1) D . \end{aligned} \quad (58)$$

We define  $\beta$  in this case as the momentum ratio *on the symmetry axis*, which means that

$$\dot{M}_w^0 V_{w1} = 2(k+1) \beta \dot{M}_w^0 V_w . \quad (59)$$

Substituting equations (55–59) into equation (54) and making use of the geometric relation between the interior angles of the triangle shown in Figure 3:

$$R \sin(\theta + \theta_1) = D \sin \theta_1 , \quad (60)$$

12 *Tarango-Yong & Henney*

**Figure 15.** True shapes of cantoids and ancantoids in the  $\Pi-\Lambda$  plane, calculated according to results of App. D. For each line,  $\beta$  varies over the range  $[0, 1]$  from lower left to upper right (although the black and red lines are truncated on the upper right), and line colors correspond to different anisotropy indices, matching those used in Fig. 14. Circle symbols mark particular  $\beta$  values: 0, 0.01, 0.1, from largest to smallest circle. Square symbols mark  $\beta = 0.5$ , but with  $\Lambda$  calculated exactly, instead of using the approximation of equation (D14). The white plus symbol marks the result for the wilkinoid:  $(\Pi, \Lambda) = (\frac{5}{3}, \sqrt{3})$ . Background shading indicates the domains of different quadric classes: hyperboloids (white), prolate spheroids (dark gray), and oblate spheroids (light gray).

yields

$$\theta_1 \cot \theta_1 = 1 + 2\beta \left( I_k(\theta) \cot \theta - \frac{1 - \cos^{k+2} \theta}{k+2} \right), \quad (61)$$

which is the generalization of CRW's equation (24) to the anisotropic case. Equation (61) is solved numerically to give  $\theta_1(\theta)$ , which is then combined with equations (60) and (1) to give the dimensionless bow shape,  $R(\theta; \beta, k)/R_0$ , where we now explicitly indicate the dependence of the solution on two parameters: axial momentum ratio,  $\beta$ , and anisotropy index,  $k$ . We refer to the resultant bow shapes as *ancantoids*.

## 5.2 True shapes of cantoids and ancantoids

The shapes of the ancantoid bow shocks are shown in Figure 14 for three different values of  $\beta$ , and are compared with the CRW results for cantoids (dashed curves). The location of these shapes in the planitude–alatitude plane is shown in Figure 15, where the gray background shading indicates the zones of different quadric classes, as in § 4, Figures 11 and 12. Values of  $\Pi$  and  $\Lambda$  are calculated via the analytic expressions derived in Appendix D1 and D2, respectively, which are only approximate in the case of  $\Lambda$ . However, the filled square symbols show the exact results for  $\beta = 0.5$ , which can be seen to lie extremely close to the approximate results, even for the worst case of  $k = 0$ . The leading term in the relative error of equation (D14) scales as  $(\beta/(k+2))^2$ , so the approximation is even better for smaller  $\beta$  and larger  $k$ .

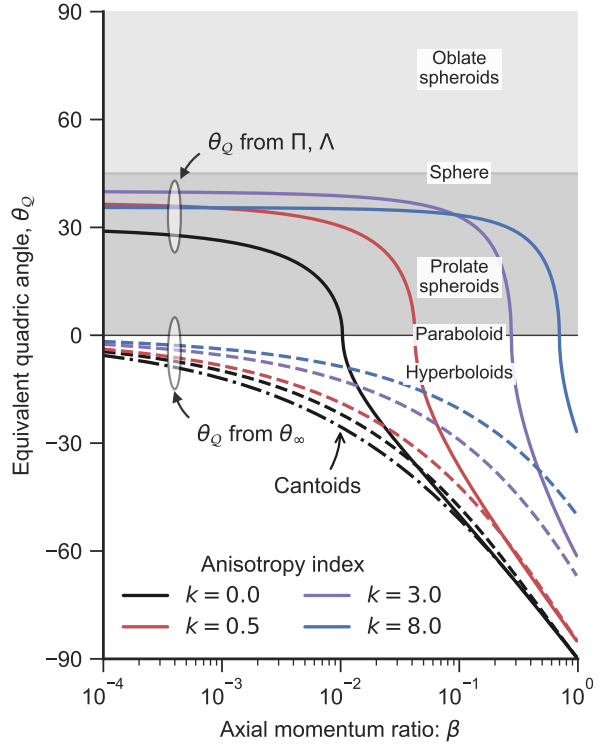


**Figure 16.** Equivalent quadric angles,  $\theta_Q$ , for ancantoids and cantoids. Solid lines show values of  $\theta_Q$  calculated from  $(\Pi, \Lambda)$ , which is representative of the shape of the head, while dashed lines show  $\theta_Q$  calculated from  $\theta_\infty$ , which is representative of the tail. Dot-dashed line shows the result for cantoids, which differ from the  $k = 0$  ancantoids in  $\theta_\infty$ , but not in  $(\Pi, \Lambda)$ . Gray shading and line colors have the same meaning as in Fig. 15.

It is apparent from Figure 14 that the  $k = 0$  ancantoid is identical to the cantoid for  $\theta \leq 90^\circ$  ( $z > 0$ , to the right of vertical dotted line in Fig. 14), but is slightly more swept back in the far wings.<sup>9</sup> Since the true planitude and alatitude depend on  $R(\theta)$  only in the range  $\theta = [0, 90^\circ]$ , the cantoid and the  $k = 0$  ancantoid behave identically in Figure 15. There is a general tendency for the bows to be flatter and more open with increasing  $\beta$  and decreasing  $k$ , with the cantoid being most open at a given  $\beta$ . All the models cluster close to the diagonal  $\Lambda \approx \Pi$  in the planitude–alatitude plane, but with a tendency for  $\Lambda > \Pi$  at higher anisotropy. There is therefore a degeneracy between  $\beta$  and  $k$  for higher values of  $\beta$ . The wilkinoid shape, which corresponds to the  $\beta \rightarrow 0$  limit of the cantoids, is marked by a white plus symbol in Figure 15, and lies in the prolate spheroid region of the plane. Cantoids lie either in the prolate spheroid or hyperboloid regions, according to whether  $\beta$  is less than or greater than about 0.01. For ancantoids of increasing  $k$ , this dividing point moves to higher values of  $\beta$ , until almost the entire range of models with  $k = 8$  are within the prolate spheroid zone.

However, the true planitude and alatitude, which are what would be observed for a side-on viewing angle ( $i = 0$ ), are not at all sensitive to the behavior of the far wings of the bow shock, which has a rather different implication as to which variety of quadric

<sup>9</sup> Due to the discontinuity in the inner wind density at  $\theta = 90^\circ$  (see Fig. 13), there is a discontinuity in the second derivative of the bow shape.

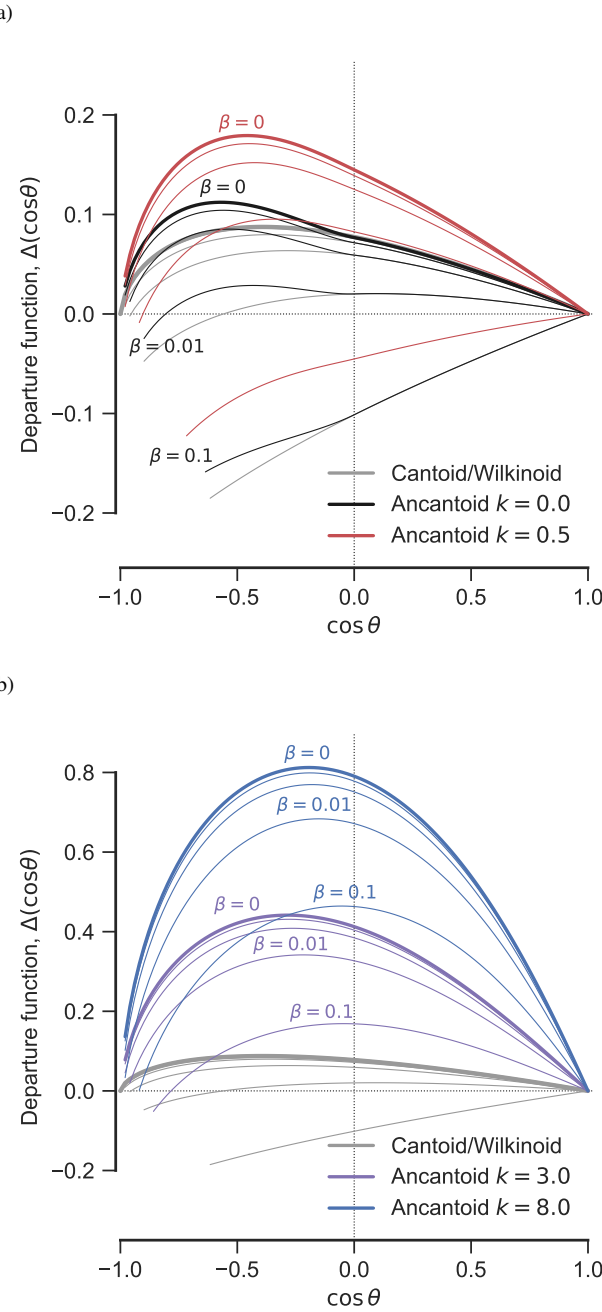


**Figure 17.** Parabolic departure function,  $\Delta(\cos \theta)$ , for ancantoids and cantoids. Heavy lines show the  $\beta = 0$  parallel stream case (Wilkinoid in the isotropic case). Light lines show increasing values of  $\beta = 10^{-4}, 0.001, 0.01, 0.1$ , as marked. (a) Cantoids (gray) and moderately anisotropic ancantoids: hemispheric,  $k = 0$  (black), and propllyd-like,  $k = 0.5$  (red). (b) Cantoids (gray) and extremely anisotropic, jet-like ancantoids:  $k = 3$  (purple) and  $k = 8$  (blue).

best approximates each shape. We illustrate this in Figure 16, which shows two different ways of estimating the quadric angle,  $\theta_Q$  (see § 4). The first is from  $(\Pi, \Lambda)$ , as in Figure 15:

$$\theta_Q^{\text{head}} = \text{sgn}(2\Pi - \Lambda^2) \tan^{-1} |2\Pi - \Lambda^2|^{1/2}, \quad (62)$$

which follows from equations (27), (28), and (34). The second is

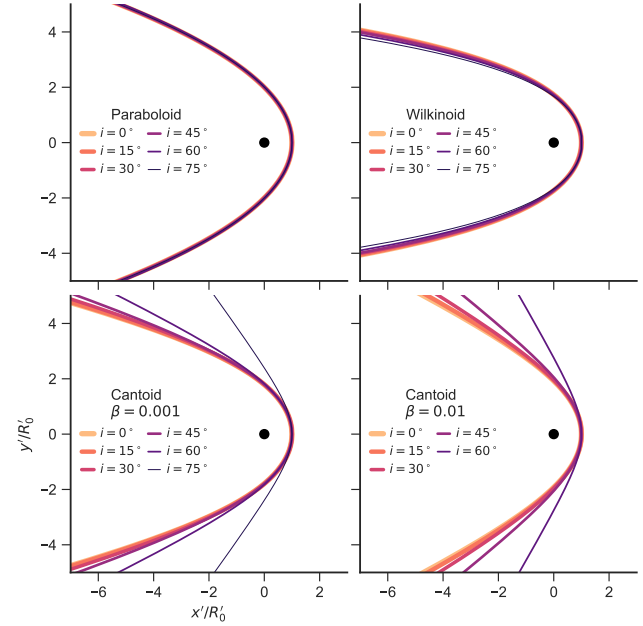


**Figure 18.** Apparent bow shapes as a function of inclination angle for isotropic thin shell models. (a) Confocal paraboloid for comparison (shape independent of inclination). (b) Wilkinoid. (c) Cantoid,  $\beta = 0.001$ . (d) Cantoid,  $\beta = 0.01$ .

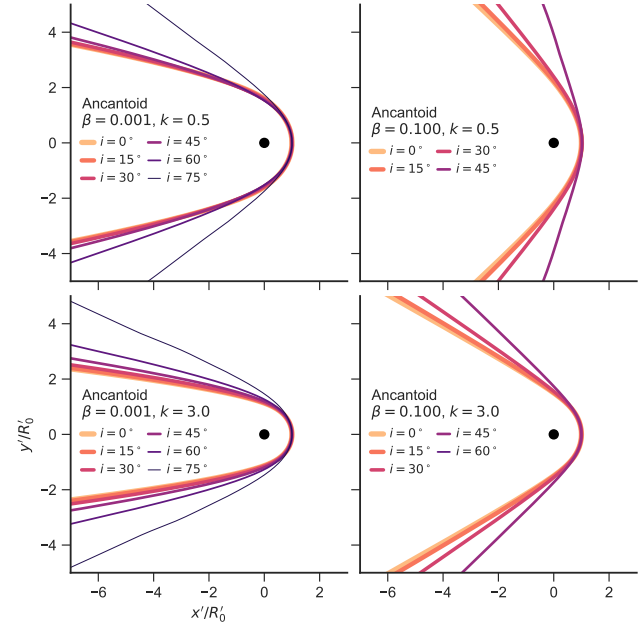


**Figure 19.** Further apparent bow shapes as a function of inclination angle for anisotropic thin shell models (ancantoids). (a)  $\beta = 0.001, k = 0.5$ ; (b) (a)  $\beta = 0.1, k = 0.5$ ; (c)  $\beta = 0.001 k = 3$ ; (d)  $\beta = 0.1 k = 3$ .

from the asymptotic opening angle of the wings,  $\theta_\infty$  (Fig. 4):

$$\theta_Q^{\text{tail}} = \theta_\infty - 180^\circ, \quad (63)$$

where  $\theta_\infty$  is calculated from equation (D17) for ancantoids, or (D19) for cantoids. If the bow shock shape were truly a quadric, then these two definitions would agree. However, as seen in Figure 16, this is

## 14 Tarango-Yong & Henney

not the case for the cantoids and ancantoids. While  $\theta_Q^{\text{head}}$  generally corresponds to a prolate spheroid (except for the largest values of  $\beta$ ),  $\theta_Q^{\text{tail}}$  always corresponds to a hyperbola. This tension between the shape of the head and the shape of the far wings has important implications for the projected shapes (as we will see in the next section), since the far wings influence the projected planitude and alatitude when the inclination is large.

Figure 17 shows the parabolic departure function (see § 4.1) for the thin-shell models. This provides an alternative perspective on the resultant bow shapes, with two different types of behavior being apparent. Models with high  $\beta$  and low anisotropy behave similarly to the hyperboloids, such as the  $(\Pi, \Lambda) = (3/2, 8/3), (2, 8/3), (8/3, 8/3)$ , and  $(3/2, 2)$  cases from Figure 9. This is the case for the  $\beta \geq 0.01$  models in Figure 17a, which all show departure functions that become negative in the far wings (more open than parabola) and terminate at a  $\theta_\infty < 180^\circ$ . The second type of behavior is shown by models with low  $\beta$  or high anisotropy, which behave like spheroids for positive and mildly negative values of  $\cos \theta$ , but, unlike the spheroids, all tend towards  $\Delta = 0$  in the far tail as  $\cos \theta \rightarrow -1$ .

### 25 5.3 Apparent shapes of projected cantoids and ancantoids

Figures 18 and 19 show the apparent bow shapes of various thin shell models (wilkinoid, cantoids, ancantoids)<sup>10</sup> for different inclination angles  $|i|$ . For comparison, Figure 18a shows the confocal paraboloid, whose apparent shape is independent of inclination (see Appendix C). The wilkinoid (Fig. 18b) shows only subtle changes, with the wings becoming slightly more swept back as the inclination increases. The cantoids (Fig. 18c and d) behave in the opposite way, with the wings becoming markedly more open once  $|i|$  exceeds  $60^\circ$  (for  $\beta = 0.001$ ), or  $45^\circ$  (for  $\beta = 0.01$ ). The ancantoids (Fig. 19) can show more complex behavior. For instance, in the  $k = 0.5, \beta = 0.001$  ancantoid (Fig. 19a) the near wings begin to become more closed with increasing inclination up to  $|i| = 60^\circ$ , at which point they open up again, whereas the opening angle of the far wings increases monotonically with  $|i|$ .

The inclination-dependent tracks that are traced by the thin-shell models in the projected planitude–alatitude plane are shown in Figure 20. The behavior is qualitatively different from the quadric shapes shown in Figure 11a in that the tracks are no longer confined within the borders of the region of a single type of quadric (hyperboloid or spheroid). At low inclinations, many of the models behave like the prolate spheroids, but then transition to a hyperboloid behavior at higher inclinations, which is due to the tension between the shape of the head and the shape of the far wings, as discussed in the previous section. This can be seen most clearly in the  $\beta = 0.001, k = 0.5$  ancantoid (lowest red line in Fig. 20a, see also zoomed version in Fig. 21). The track begins heading towards  $(\Pi', \Lambda') = (1, 1)$ , as expected for a spheroid, but then turns around and crosses the paraboloid line to head out on a hyperboloid-like track.

Ancantoids with different degrees of inner-wind anisotropy are shown in Figure 20b. In all cases, the tracks follow hyperboloid-like behavior at high inclinations, tending to populate the region just above the diagonal  $\Lambda' = \Pi'$ . The  $k = 0$  ancantoids show a kink in their tracks at the point where the projected apex passes through  $\theta = 90^\circ$ , due to the discontinuity in the second derivative of  $R(\theta)$  there (see footnote 9). The wilkinoid has a much less interesting track, most clearly seen in the zoomed Figure 21, simply moving the

<sup>10</sup> See also previous studies of the projected shape of the wilkinoid (Wilkin 1997; Cox et al. 2012; Ng et al. 2017) and the cantoids (Roberto et al. 2005).

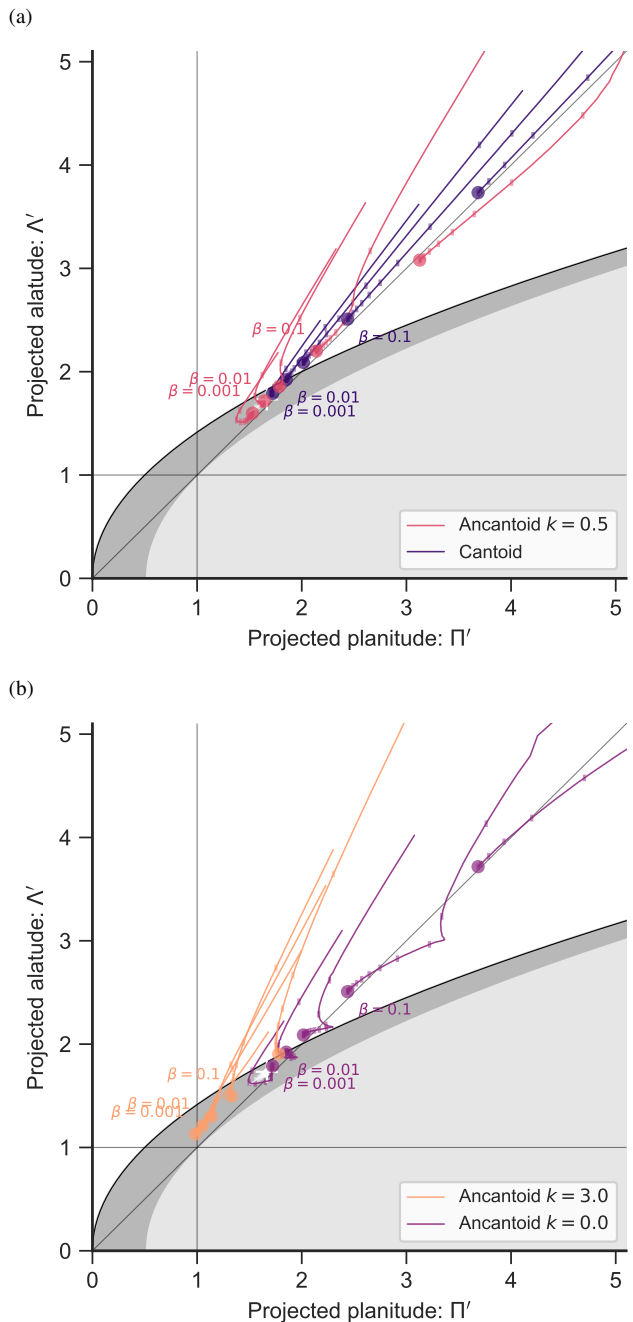


**Figure 20.** Apparent projected shapes of wilkinoid, cantoids and ancantoids in the  $\Pi' - \Lambda'$  plane. Colored symbols indicate the  $|i| = 0$  position for  $\beta = 0.001, 0.003, 0.01, 0.03, 0.1, 0.3$ . Thin lines show the inclination-dependent tracks of each model, with tick marks along each track for 20 equal-spaced values of  $|\sin i|$ . Gray shaded regions are as in Fig. 11a. The wilkinoid track is shown in white. (a) Isotropic wind model (cantoid) and proplyd-like model (ancantoid,  $k = 0.5$ ). (b) Hemispheric wind model (ancantoid,  $k = 0$ ) and jet-like model (ancantoid,  $k = 3$ ).

short distance from  $(5/3, \sqrt{3})$  to  $(3/2, \sqrt{8/3})$ . Despite its location in the ellipsoid region of the plane, the fact that it has  $\theta_\infty = 180^\circ$  means that it behaves more like a parabola at high inclination, but converges on  $(3/2, \sqrt{8/3})$  instead of  $(2, 2)$  since the far wings are asymptotically cubic, rather than quadratic.

The local density of tick marks gives an indication of how

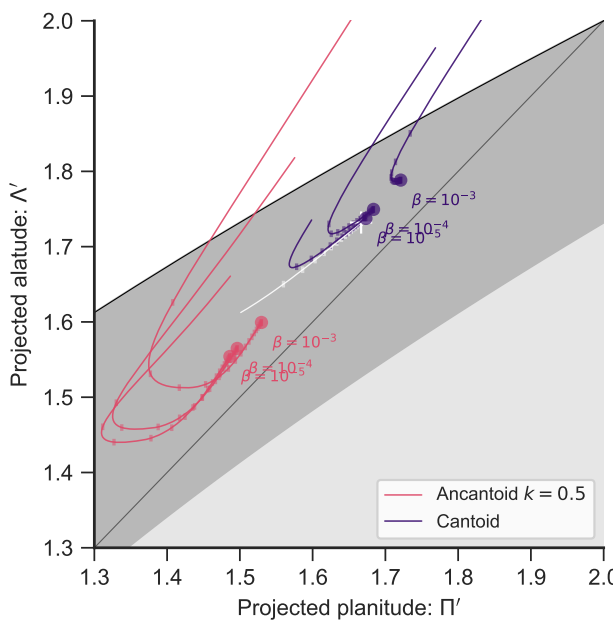


**Figure 21.** As Fig. 20a but zoomed in to show the wilkinoid track (white) and the convergence of the cantoid tracks (purple) to the wilkinoid as  $\beta \rightarrow 0$ .

likely it would be to observe each portion of the track, assuming an isotropic distribution of viewing angles. It can be seen that the ticks tend to be concentrated towards the beginning of each track, near the  $|i| = 0$  point, so the hyperboloid-like portions of the tracks would be observed for only a relatively narrow range of inclinations. This concentration becomes more marked as  $\beta$  becomes smaller, which helps to resolve the apparent paradox that the wilkinoid corresponds to the  $\beta \rightarrow 0$  limit of the cantoids, and yet follows a qualitatively different track. The detailed behavior of the small- $\beta$  cantoid models is shown in Figure 21, which zooms in on the region around the wilkinoid track. It can be seen that for  $\beta < 0.001$  the cantoid tracks begin to develop a downward hook, similar to the  $k = 0.5$  ancantoids discussed above. For  $\beta < 10^{-4}$  this begins to approach the wilkinoid track and the high inclination, upward portion of the track becomes less and less important as  $\beta$  decreases.

## 6 MORE REALISTIC BOW SHOCK MODELS

The assumptions underlying the models of the previous section may break down in various ways. To test whether the planitude–alatitude analysis is still useful in less “ideal” situations, we here apply it to more realistic simulations of stellar bow shocks. We choose a pair of hydromagnetic (HD) and magnetohydrodynamic (MHD) moving-star simulations from Meyer et al. (2017), in which the only difference is the presence (MHD case) or absence (HD case) of an ambient magnetic field with strength  $B = 7 \mu\text{G}$ , oriented parallel to the stellar velocity. In each case, the inner wind comes from a  $20 M_\odot$  main-sequence star, with mass loss rate and terminal velocity that are roughly constant with time at  $\dot{M}_w \approx 4 \times 10^{-7} M_\odot \text{ yr}^{-1}$  and  $V_w \approx 1200 \text{ km s}^{-1}$ , while the outer wind is a parallel stream due to the star’s own motion at  $40 \text{ km s}^{-1}$  through a uniform medium of density  $0.57 \text{ cm}^{-3}$ .

For these parameters, the radiative cooling distance for shocked ambient gas in the bow is a significant fraction ( $\approx 10\%$ ) of the

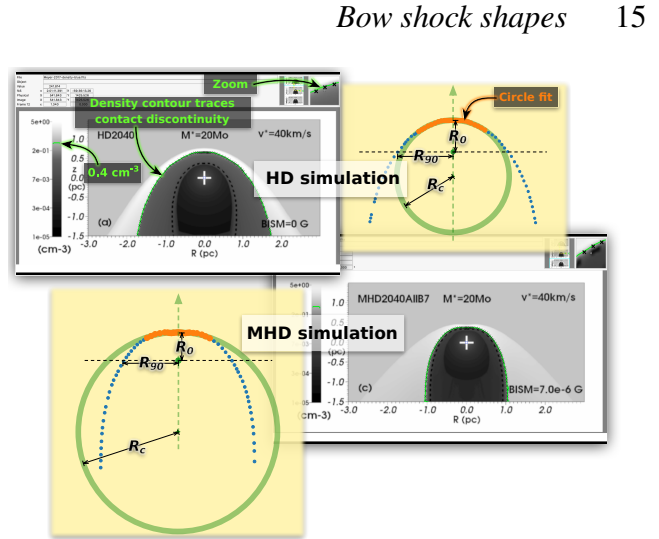


**Figure 22.** Procedure for tracing the contact discontinuity from the Meyer et al. (2017) simulations. The density maps from Meyer et al.’s Fig. 3 are converted to FITS format and displayed using the software SAOImage DS9 (Joye & Mandel 2003). The density contour at  $0.4 \text{ cm}^{-3}$  is displayed (shown in green in the figure) and this is traced by hand by placing “point regions” on the image (shown by black “x” shapes in the figure). The zoom facility of the software allows the points to be placed with any required accuracy. The points are saved to a file in the DS9 region file format, which is then read by Python programs for further processing. For example, the yellow boxes show circle fits and determination of the parameters  $R_0$ ,  $R_c$ , and  $R_{90}$ . In this example, only the points shown in orange (within  $60^\circ$  of axis) are used in the fits.

bow shock size,  $R_0$ , tending to increase towards the wings, and the radiative cooling in the shocked stellar wind is even less efficient. This represents a significant violation of the assumptions behind the thin-shell models, since the total shocked shell thickness is of the same order as  $R_0$ . Nevertheless, the emissivity of several observationally important emission processes, such as mid-infrared thermal dust emission and the optical H $\alpha$  emission line, is concentrated near the contact discontinuity,<sup>11</sup> so it is reasonable to use this surface as a first approximation for the shape of the bow.

We have traced the contact discontinuity in the two models, using the procedure outlined in Figure 22, and show results for the parabolic departure function (see § 4.1) as blue symbols in Figure 23. The MHD simulation shows a strongly negative dip in the departure function close to the apex ( $\cos \theta = 1$ ), indicating a very flat shape.<sup>12</sup> The HD simulation shows only a small negative dip in the departure function at the apex, but otherwise approximately follows the wilkinoid curve in the forward hemisphere. In both

<sup>11</sup> Note that, in the non-magnetic HD models, efficient thermal conduction leads to a thick layer of hot, thermally evaporated ambient material that separates the shocked stellar wind from the cool, dense shell of shocked ambient gas (see § 3.3 of Meyer et al. 2014). In this case, the contact discontinuity is taken to be the boundary between hot and cold ambient gas, as opposed to the *material discontinuity* between shocked ambient gas and shocked wind gas. In the MHD models, the thermal conduction is almost completely suppressed, so that the material and contact discontinuities coincide.

<sup>12</sup> Meyer et al. (2017) speculate that this flatness may be the signature of the formation of a complex multiple-shock topology at the apex (de Sterck & Poedts 1999). For our purposes, the reason does not matter, merely that the magnetic and non-magnetic models predict markedly different shapes.

## 16 Tarango-Yong &amp; Henney

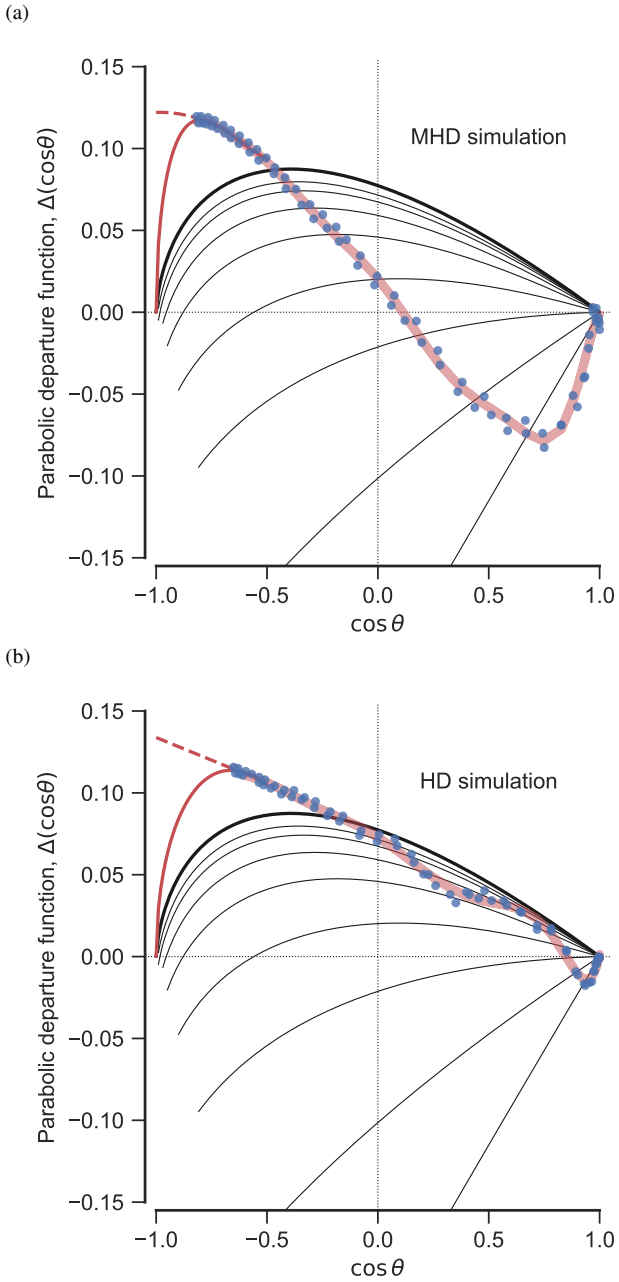


**Figure 23.** Departure function for the shape of the contact discontinuity, measured from two numerical simulations of a  $20 M_{\odot}$  main-sequence star, moving at  $40 \text{ km s}^{-1}$  through a uniform medium of density  $0.57 \text{ cm}^{-3}$  (Meyer et al. 2017). (a) Magnetohydrodynamic simulation with ambient magnetic field of strength  $7 \mu\text{G}$ , oriented parallel to the stellar velocity. (b) Hydrodynamic simulation with zero magnetic field. Blue dots show the measured shape, while the thick, pale-red line shows a 12th-order Chebyshev polynomial fit. The published shapes only extend to  $\theta \approx 130\text{--}150^\circ$ , so we extrapolate the shapes out to  $\theta = 180^\circ$ . Two different extrapolations are shown, corresponding to bows that are asymptotically closed (dashed red line) or open (solid red line). For comparison, black lines show the departure function for wilkinoid (thick line) and cantoids (thin lines).

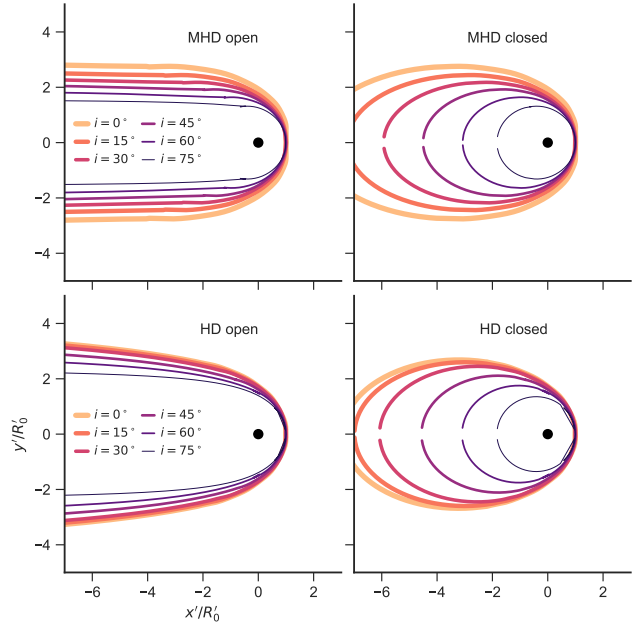


**Figure 24.** Projected shapes of contact discontinuity from simulations at different inclinations  $|i|$  (varying line color and thickness, see key). Top row shows magnetized simulation of Fig. 23a, bottom row shows non-magnetized simulation of Fig. 23b. Left column shows asymptotically open extrapolation, right column shows asymptotically closed extrapolation. All shapes are normalized to the projected apex distance,  $R'_0$

cases the departure function is more positive than the wilkinoid in the far wings ( $\cos\theta < -0.5$ ), but we do not have data for the full range of  $\theta$ , and so two different extrapolations for  $\theta \rightarrow 180^\circ$  are shown. In the first (dashed red line in figure), we fit a low-order polynomial of  $\cos\theta$  to the points with  $\cos\theta < -0.5$  and extend it to  $\cos\theta = -1$ , which gives an asymptotically closed shape. In the second extrapolation (solid red line in figure), we fit a polynomial that is multiplied by  $(1 + \cos\theta)^{1/2}$ , which forces the departure function to zero at  $\cos\theta = -1$ , giving an asymptotically open shape, as with the wilkinoid. In a true steady state, the far wings should be asymptotically open, but as  $\theta \rightarrow 180^\circ$  the flow times become longer and longer, so that a bow shock with a finite age will be closed.

Using a 12th-order Chebyshev fit to the traced shapes, we show the apparent shape of the contact discontinuity at a series of inclination angles,  $|i|$ , in Figure 24. The four panels show the two simulations for each of the two far-wing extrapolations. Comparison with Figures 18 and 19 shows the general tendency is the same as with the wilkinoid: that the apex becomes less flat and the wings less open as the inclination angle is increased. There is no sign of the sudden increase in openness at high inclination, as seen in the cantoids and ancantoids that are asymptotically hyperbolic. On the other hand, the projected shapes of both simulations vary much more strongly with  $|i|$  than the wilkinoid does. For the HD simulation, this is mainly apparent for  $|i| > 30^\circ$ , but for the MHD simulation it occurs at all inclinations.

The resultant inclination-dependent tracks in the planitude–alatitude plane are shown in Figure 25. These are compared with measurements<sup>13</sup> from post-processed infrared dust continuum maps

<sup>13</sup> The shape measurements were performed by converting to contours the  $60 \mu\text{m}$  images in Meyer et al. (2017)'s Fig. 10 and then tracing the ridge of

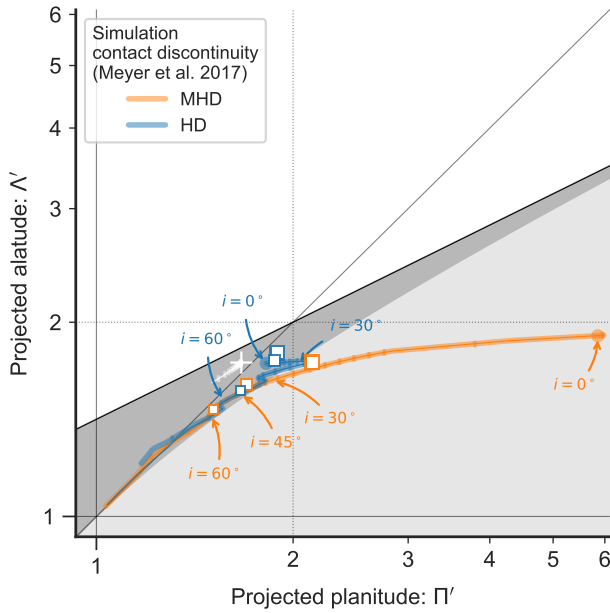


**Figure 25.** Apparent projected shapes of simulations in the  $\Pi'$ – $\Lambda'$  plane. Thick solid lines show the predicted inclination-dependent tracks of the traced contact discontinuity shape for the asymptotically open extrapolation, with tick marks indicating 20 equal intervals in  $|\sin i|$ . Thin solid lines show the same for the asymptotically closed extrapolation, which only deviates from the open case at the high- $|i|$  end of the HD tracks. The true planitude and alatitude are marked by filled circle symbols. Open square symbols show the shapes traced from the dust emission maps at 60  $\mu\text{m}$  for inclinations of (largest to smallest) 30°, 45°, and 60°. For comparison, the wilkinoid track is shown in white. Note that the scales of both axes are logarithmic in this case.

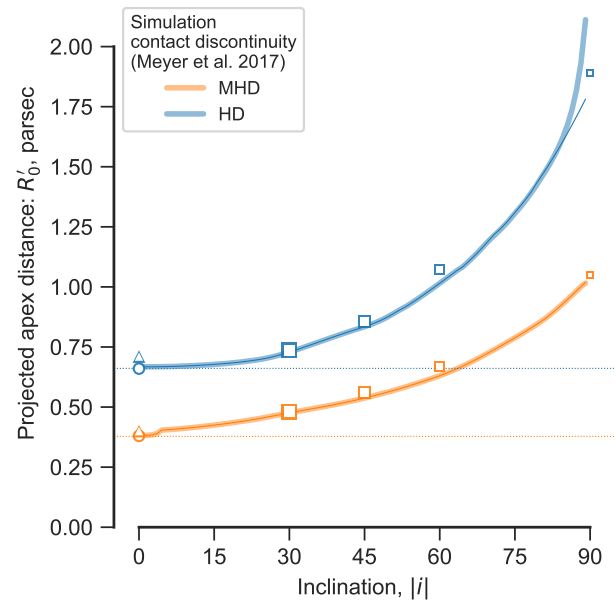
at 60  $\mu\text{m}$  (§ 4.3 of Meyer et al. 2017), shown by open square symbols for  $i = 30^\circ, 45^\circ$ , and  $60^\circ$ . The agreement between the two is good. In particular, the 60  $\mu\text{m}$ -derived shapes are always very close to the tracks derived from the contact discontinuity shape. Also, the ordering of the three inclinations along the tracks corresponds to what is predicted, although quantitatively there are some slight deviations. This close agreement stems from the fact, emphasized by Meyer et al. (2014), that the long-wavelength dust emission from hot-star bow shocks tends to be dominated by material just outside the contact discontinuity. Note that there is almost no difference in the planitude–alatitude tracks between the closed and open extrapolations. This is because  $\Pi'$  and  $\Lambda'$  only depend on the portion of  $R(\theta)$  between  $\theta_0$  (eq. [18]) and  $\theta_{90}$  (eq. [21]), and these are both smaller than the  $\theta$  range where extrapolation is necessary, except for in the HD case at the highest inclinations.

Figure 26 shows the inclination dependence of the projected apex distance,  $R'_0$ . As in the previous figure, the lines show the prediction based on the shape of the contact discontinuity, while the square symbols show the results from the 60  $\mu\text{m}$  dust continuum maps.<sup>14</sup> In addition, triangle symbols show results from H $\alpha$  optical

minimum radius of curvature of the contours. Identical results are found from using the 100  $\mu\text{m}$  maps instead. For the 25  $\mu\text{m}$  maps, although the same results are found for low inclinations, in the maps with  $|i| \geq 45^\circ$  in the HD case it becomes impossible to trace the limb-brightened rim because it becomes fainter than the emission from the true apex of the bow.

<sup>14</sup> There is an apparent error in the spatial scales for the HD simulations in Figs. 10 and 11 of Meyer et al. (2017), with the dust emission peaks occurring

## Bow shock shapes 17



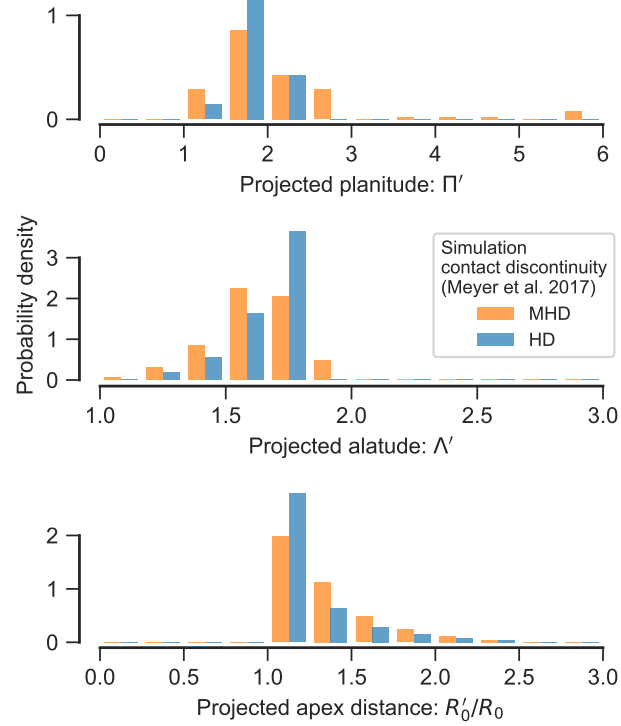
**Figure 26.** Apparent projected apex distance of simulations. Line and symbol meanings are as in Figure 25. In addition, triangle symbols at  $|i| = 0^\circ$  denote radius measured on H $\alpha$  optical emission maps. Note that the distances for the blue square symbols have been adjusted according to the correction factor discussed in footnote 14.

emission line maps, which are given for  $i = 0$  in Fig. 7 of Meyer et al. (2017). Again, the agreement is good between the values derived from the shape of the contact discontinuity and those derived from the surface brightness maps. The greatest discrepancy is seen with the H $\alpha$  maps and the intermediate inclination dust maps, with  $R'_0$  being overestimated by a few percent in both cases. The differences in behavior between the two simulations are much larger than this. The larger true planitude of the MHD simulation means that the relative increase of  $R'_0$  with  $|i|$  is much stronger than in the HD simulation for  $|i| < 45^\circ$ , as expected from Figure 10b.

The probability densities<sup>15</sup> of the apparent shape and size of the simulation bows (measured at the contact discontinuity) are shown in Figure 27, assuming that the viewing direction is uniformly distributed in solid angle. The modal value of the projected planitude is similar at  $\Pi' \approx 1.8$  for both simulations, but the distribution is much broader in the MHD case, which has a low-level wing extending out to  $\Pi' \approx 6$ . The projected alatitude distributions are both

at radii that are clearly too large. The stated apex distance for the contact discontinuity in this simulation is 0.69 pc from Table 2 of Meyer et al. (2014), and the position of the peak in dust column density is 0.70 pc from Fig. 17a of Meyer et al. (2014). These are consistent with Figs. 3, 4, and 7 of Meyer et al. (2017), but not with Figs. 10 and 11. Luckily, the position of the true apex is clearly visible in the 25  $\mu\text{m}$  maps of Fig. 10 at inclinations of 45° and 60°. The projected separation of the true apex is  $R_0 \cos i$ , independent of the bow shape, which allows a correction factor of 0.65 to be found, assuming that the on-axis peak in the 25  $\mu\text{m}$  emission coincides with the peak in dust column density. This correction has been applied to the blue square symbols shown in our Fig. 26.

<sup>15</sup> The probability density is defined so that its integral over the full range of the histogrammed variable is unity, making it independent of the histogram bin widths. This means that the characteristic width of an approximately unimodal distribution is one over the maximum probability density.

18 *Tarango-Yong & Henney*

**Figure 27.** Histograms of (top to bottom) projected planitude, alatitude, and bow shock size for the shape of the contact discontinuity in the Meyer et al. (2017) simulations. The y axis gives the probability density (per unit x-axis quantity), assuming a uniform distribution of viewing directions.

**Table 1.** Fitted planitude and alatitude for M42 bows

Source	Bow	$\Pi'$	$\langle \Lambda' \rangle$	$\Delta \Lambda'$
000-400	Inner	$2.87 \pm 0.19$	$2.40 \pm 0.04$	$0.35 \pm 0.08$
	Ridge	$3.62 \pm 0.38$	$2.73 \pm 0.02$	$0.51 \pm 0.10$
	Outer	$2.51 \pm 0.24$	$2.46 \pm 0.02$	$-0.06 \pm 0.02$
	All	$3.00 \pm 0.54$	$2.53 \pm 0.15$	$0.16 \pm 0.16$
069-601	Inner	$3.81 \pm 0.23$	$2.90 \pm 0.01$	$0.44 \pm 0.05$
	Ridge	$2.43 \pm 0.13$	$2.17 \pm 0.01$	$0.07 \pm 0.02$
	Outer	$2.22 \pm 0.15$	$2.11 \pm 0.01$	$0.01 \pm 0.01$
	All	$2.82 \pm 0.75$	$2.39 \pm 0.37$	$0.17 \pm 0.20$

narrower than the planitude (note the different scale of the histogram axis), with the MHD case again being the broader of the two and peaking at a slightly lower value ( $\Lambda' \approx 1.7$  as opposed to  $\approx 1.8$  for the HD case). Finally, the distribution of projected-over-true apex distance is also broader for the MHD case.

## 7 EXAMPLE APPLICATION TO OBSERVATIONS

As an example of measuring the projected planitude and alatitude of real bow shocks, we present an analysis of M42 000-400 and M42 069-601, which are two H $\alpha$  emission arcs (Bally et al. 2000;

Gutiérrez-Soto 2015) associated with proplyds<sup>16</sup> in the west of the Orion Nebula (M42) at a distance of roughly 0.5 pc from the high-mass Trapezium stars that ionize the nebula. An image of one of these arcs (M42 069-601) was used in the illustration of bow shock terminology in Figure 1.

### 7.1 Empirical determination of bow shock shape

We consider three different tracings of the bow shape (see Fig. 28): the peak of the emission arc (“ridge”), and its inner and outer edges. In all three cases, we placed by eye the points that define the bow, using SAOImage DS9 (Joye & Mandel 2003) in a similar fashion to in Figure 22, and guided by the image contours.<sup>17</sup>

We determine the planitude and alatitude by fitting a circle to the traced points within  $\pm \Delta\theta = 75^\circ$  of the bow axis, using the iterative algorithm described in Appendix E. The fitted circle, when combined with the position of the central source, yields the orientation of the bow axis, together with the apex distance,  $R_0$ , radius of curvature,  $R_c$ , and two perpendicular radii (one for each wing),  $R_{90+}$  and  $R_{90-}$ . These are all indicated on the panels of Figure 28 by light-colored lines.<sup>18</sup> The projected planitude and alatitude then follow as  $\Pi' = R_c/R_0$ ,  $\Lambda'_+ = R_{90+}/R_0$ ,  $\Lambda'_- = R_{90-}/R_0$ , which are shown in Figure 29.

### 7.2 Analysis of sources of systematic uncertainty

The planitude is found to have a moderate dependence on the choice of  $\Delta\theta$ , as shown in Figure 30, where it can be seen that, although the values of  $\Pi'$  are relatively stable for  $\Delta\theta \geq 60^\circ$  (light gray shaded region), they can show much larger variations for  $\Delta\theta < 60^\circ$ . The fact that the radius of curvature is defined at a point (the projected apex) might seem to argue for making  $\Delta\theta$  as small as possible, but that would lead to circle fits that were extremely sensitive to the exact positions of the few points included in the fit. A reliable fit requires 4 or more points, ideally spanning a total separation that is a substantial fraction of  $R_c$ , which would argue for  $\Delta\theta$  larger than about  $\Pi'/2$  radians, or  $60^\circ$  to  $90^\circ$ . On the other hand, if  $\Delta\theta \geq 90^\circ$  then the planitude and alatitude would no longer be independent since the bow would be forced to lie on the “sphere” line,  $\Lambda' = (2\Pi' - 1)^{1/2}$  (see § 4). Balancing these two concerns suggests an optimal  $\Delta\theta = 75^\circ$ , which is shown in Figure 28, whereas in Figure 29 we show results for both  $75^\circ$  (thick lines) and  $60^\circ$  (thin lines).

Unlike all the models considered in § 5 and § 6, the observed bows are not necessarily symmetrical and so the alatitude for the two wings,  $\Lambda'_+$  and  $\Lambda'_-$ , may be different. We therefore calculate an average alatitude,  $\langle \Lambda' \rangle$ , and an alatitude asymmetry,  $\Delta \Lambda'$ :

$$\langle \Lambda' \rangle = \frac{1}{2} (\Lambda'_+ + \Lambda'_-) \quad \Delta \Lambda' = \frac{1}{2} (\Lambda'_+ - \Lambda'_-) \quad (64)$$

The results for these two quantities, together with the planitude, are shown in Table 1. For each object and for each tracing (inner, ridge, outer, see Fig. 28), the mean  $\pm$  standard deviation is listed for circle

<sup>16</sup> The coordinate designation (see O’Dell & Wen 1994 for an explanation of the nomenclature) of 000-400 is very imprecise in right ascension, but we use it here for consistency with previous papers. The associated proplyd is listed with the more correct designation 4596-400 in catalogs such as Ricci et al. (2008).

<sup>17</sup> In the case of the “ridge” method at least, it is possible to automate this step, which we will discuss in detail in a following paper.

<sup>18</sup> For conciseness, we drop the prime symbol from the radii, both in this section and in Appendix E, even though they are all projected quantities.

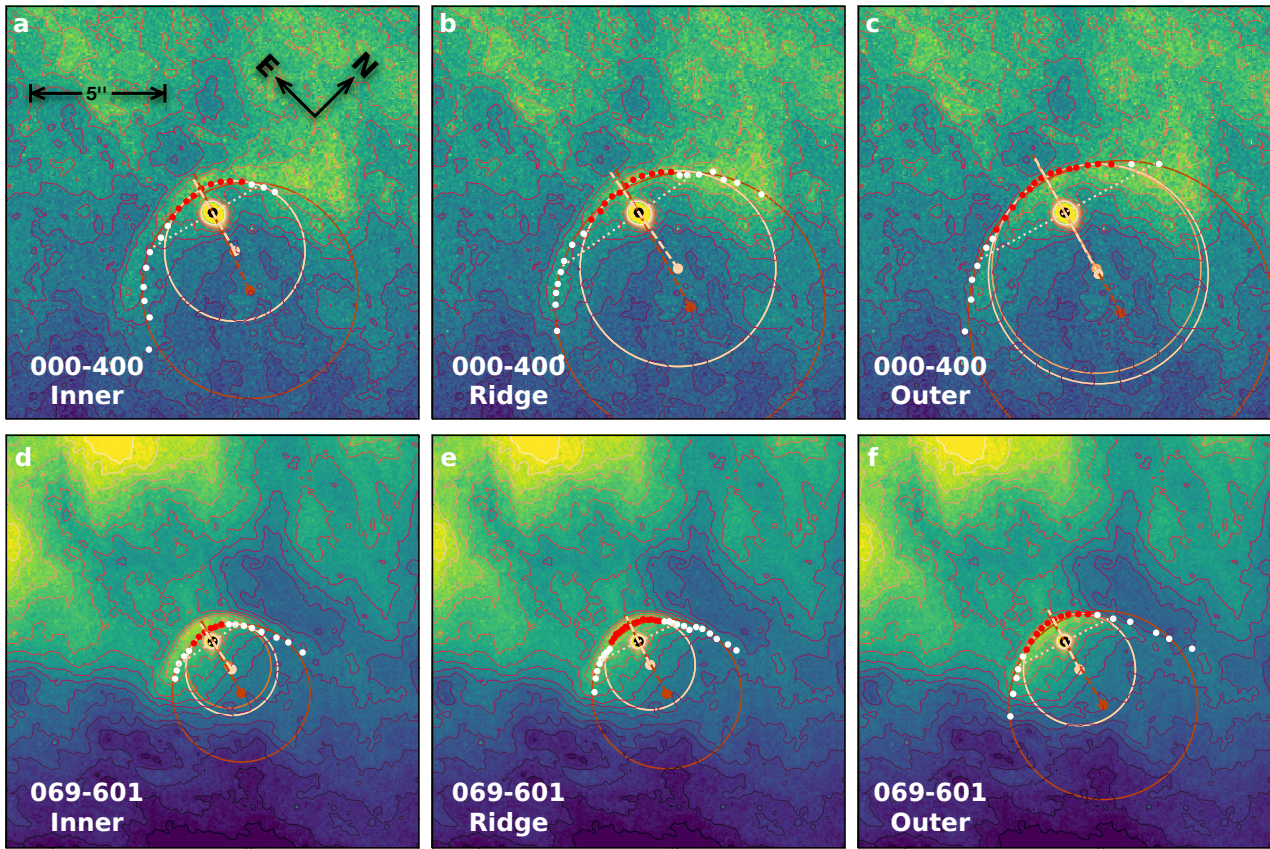


**Figure 28.** Example empirical determination of planitude and alatitude for observed bow shocks associated with proplyds in the outer Orion Nebula (M42). Color scale and contours show an *HST* H $\alpha$  image (ACS F658N filter, Bally et al. 2006) of M42 000-400 (panels *a–c*) and M42 069-601 (panels *d–f*). The image scale and orientation are indicated on panel *a* and are the same for all panels. Three different bows have been traced by eye on each object (red and white filled symbols): (*a, d*) inner edge, (*b, e*) ridge of maximum emission, and (*c, f*) outer edge. For each panel, the dark-colored circle shows the initial fit to the full set of points (white and red), using the algorithm described in Appendix E. The center of curvature and derived axis are shown by a small filled circle and dashed line in the same color. Lighter colored circles show three subsequent iterations where the fit is restricted to points within  $\pm\Delta\theta = 75^\circ$  of the axis. The subset of points used in the final iteration is marked in red. The perpendicular radii for the final iteration are shown by dotted lines. In panels *a, b, d–f* the iterations converge immediately, but in panel *c* the iterations stably oscillate between two slightly different solutions.

fits using  $\Delta\theta = 60^\circ$  to  $80^\circ$  (see Fig. 30). Additionally, the row ‘‘All’’ for each object gives the global mean and standard deviation over all three tracings.

It can be seen from Table 1 that the uncertainty in the fitted parameters is dominated by the variations between the different traced shapes. For example, the one-sigma relative variation of planitude,  $\Pi'$ , is  $< 10\%$  within the individual tracings, but  $\approx 20\%$  between tracings. For the mean alatitude,  $\langle\Lambda'\rangle$ , the variation within individual tracings is extremely small<sup>19</sup> at  $\approx 1\%$ , but is  $\approx 10\%$  between tracings. The alatitude asymmetry,  $\Delta\Lambda'$ , is best interpreted as a difference between the symmetry axis of the apex region and the symmetry axis of the wings. In relative terms, this is 0–20%, but with large systematic variations between tracings (for instance, in both objects it is very small for the outer arcs).

It could be argued that much of the between-tracing variations

in  $\Pi'$  and  $\langle\Lambda'\rangle$  are due to real differences between the shapes of the inner and outer boundaries of the emission arc. Although this may be true, in the absence of a robust theory as to exactly what feature of the observed images constitutes *the* bow shock, such variations nevertheless serve to limit the precision with which the bow shock shape can be measured. We therefore conclude that conservative estimates of 20% precision for  $\Pi'$  and 10% precision for  $\Lambda'$  are appropriate when analyzing observations of a similar or better quality<sup>20</sup> to those presented in Figure 28. This will be an important limitation when comparing the statistics of the shapes of different bow shock populations, as we will present in a following paper.

<sup>19</sup> This is because the only way that variation in the circle fit parameters affect the alatitudes is through the axis orientation vector, and changing the orientation induces roughly opposite effects on  $\Lambda'_+$  and  $\Lambda'_-$ , which approximately cancel out in  $\langle\Lambda'\rangle$ .

<sup>20</sup> Since the uncertainties are systematic and due to unavoidably subjective decisions, it is unlikely that better quality observations would improve the situation, although poorer quality observations could make things worse.

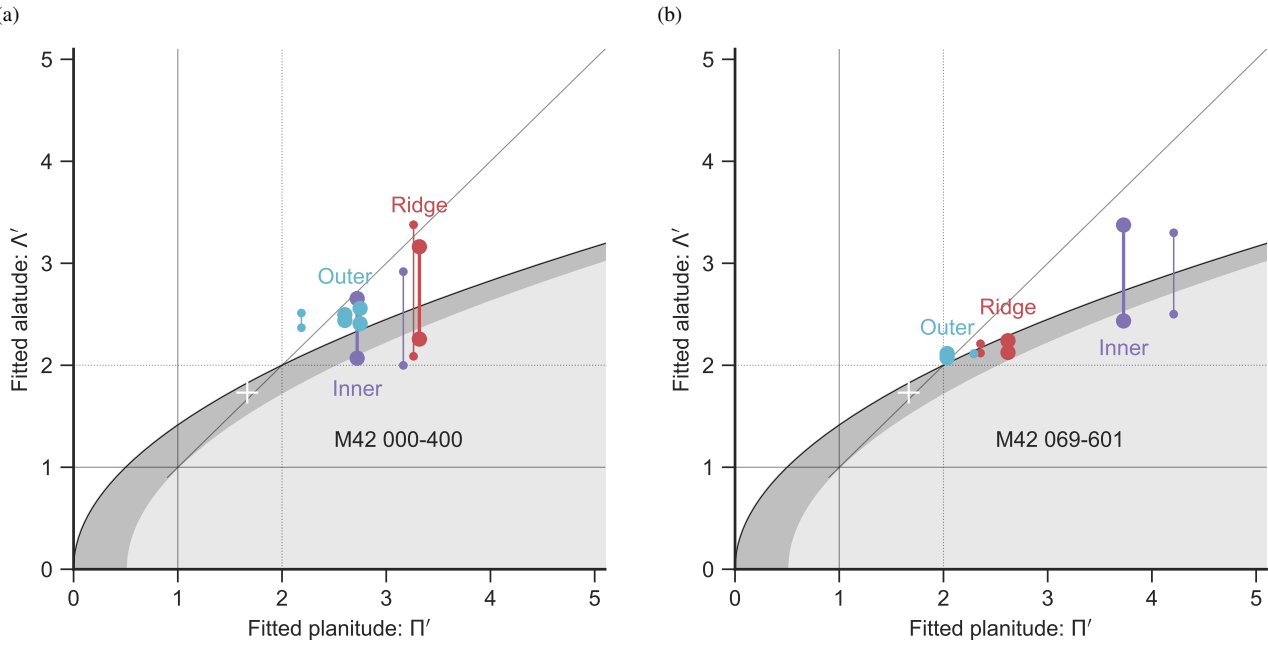


**Figure 29.** Location in the projected planitude–alatitude plane of the converged circle fits to the M42 bows: (a) 000-400, (b) 069-601. For each solution, the two values of the projected alatitude,  $\Lambda'_+$  and  $\Lambda'_-$ , corresponding to  $R_{90+}$  and  $R_{90-}$ , are joined by a vertical line. Large symbols show the results from the fits shown in Figure 28, while small symbols show results for fits using  $\Delta\theta = 60^\circ$  instead of  $75^\circ$ . In panel *a*, two slightly different  $\Pi'$  values are shown for the outer bow, since the fit does not converge to a single value (see Fig. 28c and App. E).

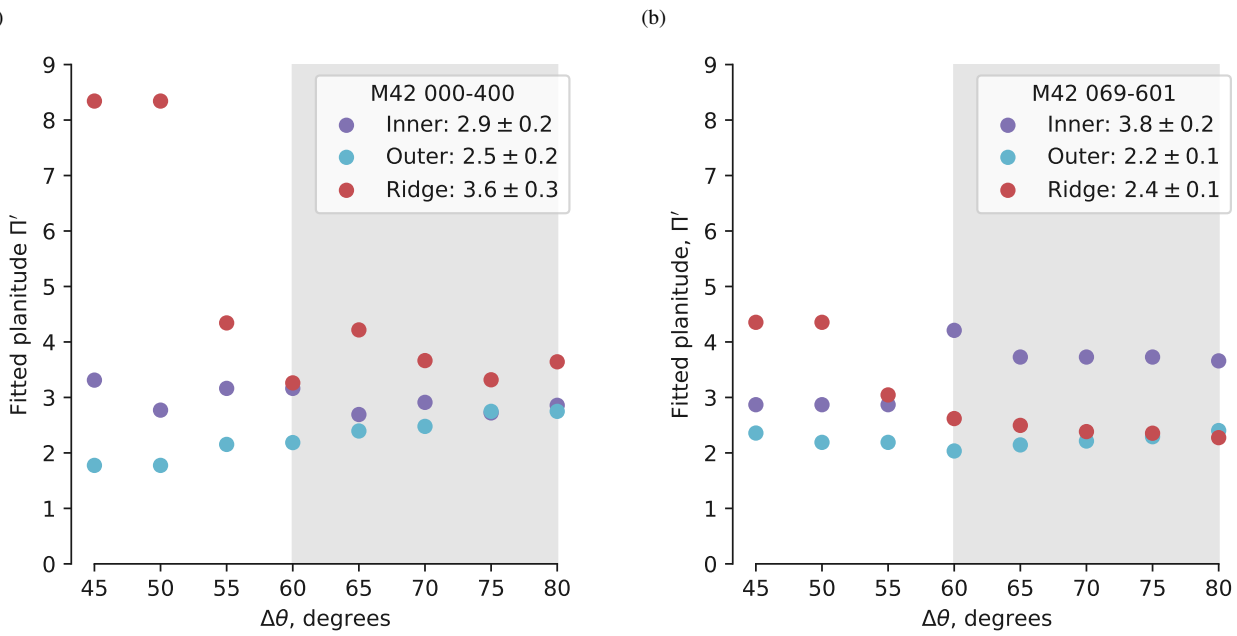


**Figure 30.** Variation of fitted planitude,  $\Pi'$ , as a function of the parameter  $\Delta\theta$ , which controls how close a point must be to the axis in order to be included in the circle fit. (a) M42 000-400, (b) M42 069-601. For the three traced bows (inner, outer, and ridge) of each object, the symbol key lists the mean and standard deviation of  $\Pi'$ , calculated over the “stable” range  $\Delta\theta = 60^\circ$  to  $80^\circ$ , which is indicated by light gray shading.

### 7.3 Derived shape of the M42 arcs

From a casual inspection of Figure 28, it is apparent that the shapes of the two M42 arcs are closely similar, and this is confirmed by the numbers in Table 1. Both 000-400 and 069-601 are consistent with  $(\Pi', \Lambda') \approx (3.0, 2.5)$ , and if we take the absolute minimum

over all the different tracings and reasonable variations in the  $\Delta\theta$  fit parameter, we find unassailable lower limits of  $(\Pi', \Lambda') > (2.1, 2.1)$ . In the rest of this section, we consider only these lower limits, since they are already sufficient for drawing interesting conclusions.

Comparison with Figure 25 shows that both the MHD and HD simulations of Meyer et al. (2016) are inconsistent with the

observations. Although  $\Pi' > 2.1$  can be satisfied,<sup>21</sup> the simulations' projected alatitude is  $\Lambda' < 1.9$  for all inclinations, which is significantly less than the observed lower limit of 2.1. This is not particularly surprising since the simulations were not tailored to the situation of these proplyd bow shocks in M42, in which the mildly supersonic photoevaporation flow from an externally irradiated protoplanetary disk interacts with the mildly supersonic champagne flow from the core of the Orion Nebula. The proplyd case has at least four important differences from the runaway O-star case modeled by Meyer et al. (2016): (1) The velocity of the outer wind is  $\leq 20 \text{ km s}^{-1}$  instead of  $40 \text{ km s}^{-1}$ ; (2) The outer wind is slightly divergent, rather than plane-parallel; (3) Both inner and outer shocks are strongly radiative, so both shells (see Fig. 2) contribute to the observed emission; (4) The inner wind is not isotropic, but instead corresponds to the  $k = 0.5$  case of equation (53). The ways in which these differences may account for the discrepancy with the observations will be explored in detail in a subsequent paper.

## 8 SUMMARY AND DISCUSSION

We have shown that the shapes of stellar bow shocks can be usefully characterized by two dimensionless numbers: the *planitude*,  $\Pi$ , or flatness of the bow's apex, and the *alatitude*,  $\Lambda$ , or openness of the bow's wings (§ 2). The planitude and alatitude can be estimated from ratios of lengths that can be straightforwardly measured from observations or theoretical models. We develop a general method (§ 3) for finding the projected shape,  $(\Pi', \Lambda')$ , of a bow shock's limb-brightened edge, or *tangent line*, as a function of inclination angle,  $i$ , where the emission shell is idealized as a cylindrically symmetric surface.

We first apply this method to find inclination-dependent tracks on the projected planitude–alatitude plane for the special case of *quadric* surfaces (§ 4), such as hyperboloids, paraboloids, and spheroids, where the tangent line is a conic section. The spheroids and hyperboloids occupy distinct regions of the plane, with the paraboloids defining the boundary between the two. As the inclination is increased from  $|i| = 0$  (side-on) to  $|i| = 90^\circ$  (end-on), the tracks first tend to approach the diagonal  $\Lambda' = \Pi'$ , corresponding to confocal conics, always remaining within their own region. At the highest inclinations, the spheroids all converge at  $|i| = 90^\circ$  on the point  $(\Pi', \Lambda') = (1, 1)$  and the paraboloids on the point  $(\Pi', \Lambda') = (2, 2)$ . The hyperboloids, on the other hand diverge as  $(\Pi', \Lambda') \rightarrow (\infty, \infty)$  for a finite  $i_{\text{crit}}$ , which depends on the asymptotic opening angle of the tail. For  $|i| > i_{\text{crit}}$ , the tangent line no longer exists for the hyperboloid, and it would no longer appear to be a curved bow shock. We introduce the parabolic departure function (§ 4.1) as tool for visualizing differences in bow shapes,  $R(\theta)$ , over the full range,  $\theta = [0^\circ, 180^\circ]$ .

We then apply the projection method to a set of thin-shell hydrodynamic models of bow shocks (§ 5): the *wilkinoid* from a wind-parallel stream interaction and the *cantoids* from wind-wind interactions. We generalize the latter to the *ancantoids*, where one of the winds is anisotropic. We find that the wilkinoid is confined to a small region of the  $\Pi'-\Lambda'$  plane, with projected planitude and alatitude varying with inclination by  $< 15\%$ . The cantoids and ancantoids with sufficiently small values of  $\beta$ , the wind momentum ratio, have more interesting behavior, with tracks that pass from the

<sup>21</sup> Either by the MHD simulations at low inclinations ( $|i| = 0^\circ\text{--}20^\circ$ ) or by the HD simulation at intermediate inclinations ( $|i| = 30^\circ\text{--}40^\circ$ ).

spheroid region at low inclinations to the hyperboloid region at high inclinations.

In the following section (§ 6), we test the projected shape analysis methods against the results of computational fluid dynamic simulations of magnetized and non-magnetized bow shocks from Meyer et al. (2017) of a runaway OB main-sequence star. We find that measurements made on maps of infrared dust emission can be accurate diagnostics of the projected shape of the contact discontinuity for this type of bow shock (Fig. 25). The distributions of projected planitude and alatitude for a population of randomly oriented bow shocks shows systematic differences between the different simulations.

Finally (§ 7), we give an example of the application of our methods to observed emission maps of bow shocks, describing a robust algorithm for empirically determining the projected planitude and alatitude from imperfect real data. We investigate the sensitivity of the results to systematic errors due to both observational uncertainties and subjective choices in the application of the algorithm. We find that the projected planitude and alatitude can be determined with precisions of 20% and 10%, respectively. For our illustrative observations, we show that this is more than sufficient to rule out certain models.

This paper is the first of a series that will apply our shape analysis to a wide variety of models and observations of stellar bow shocks. In a second paper, we consider the alternative model of dusty radiation-driven bow wave (Ochsendorf et al. 2014), instead of a hydrodynamic bow shock, and also calculate the signature in the planitude–alatitude plane of oscillations in the bow shape, which may be due to instabilities or a time-varying source. In a third paper, we apply our techniques to observational datasets for three different classes of stellar bow shocks: OB stars (Kobulnicky et al. 2016), cool giants/supergiants (Cox et al. 2012), and young stars in the extended Orion Nebula (Henney et al. 2013). In a fourth paper, we analyze the proplyd bow shocks in the core of the Orion Nebula (García-Arredondo et al. 2001).

## ACKNOWLEDGEMENTS

We are grateful for financial support provided by Dirección General de Asuntos del Personal Académico, Universidad Nacional Autónoma de México, through grant Programa de Apoyo a Proyectos de Investigación e Innovación Tecnológica IN111215. JATY acknowledges support via a research studentship from Consejo Nacional de Ciencias y Tecnología, Mexico. This work has made extensive use of Python language libraries from the SciPy (Jones et al. 2018) and AstroPy (Astropy Collaboration et al. 2013, 2018) projects. We appreciate the thoughtful comments of the anonymous referee, which led us to clarify the presentation of our results and prompted the addition of § 7 and Appendices A and B.

## REFERENCES

- Astropy Collaboration et al., 2013, A&A, 558, A33
- Astropy Collaboration et al., 2018, preprint, ([arXiv:1801.02634](https://arxiv.org/abs/1801.02634))
- Bally J., O'Dell C. R., McCaughrean M. J., 2000, AJ, 119, 2919
- Bally J., Licht D., Smith N., Walawender J., 2006, AJ, 131, 473
- Canto J., Raga A. C., Wilkin F. P., 1996, ApJ, 469, 729
- Cox N. L. J., et al., 2012, A&A, 537, A35
- García-Arredondo F., Henney W. J., Arthur S. J., 2001, ApJ, 561, 830
- Gayley K. G., 2009, ApJ, 703, 89
- Gfrerrer A., Zsombor-Murray P., 2009, Journal for Geometry and Graphics, 13, 131

22 *Tarango-Yong & Henney*

- Goldman R., 1983, *IEEE Computer Graphics and Applications*, 3, 68
- Graham M. F., Meaburn J., Garrington S. T., O'Brien T. J., Henney W. J., O'Dell C. R., 2002, *ApJ*, 570, 222
- Guggenheimer H., 2012, Differential Geometry. Dover Books on Mathematics, Dover Publications
- Gutiérrez-Soto L. Á., 2015, Master's thesis, Universidad Nacional Autónoma de México
- Hartigan P., Raymond J., Hartmann L., 1987, *ApJ*, 316, 323
- Hayward T. L., Houck J. R., Miles J. W., 1994, *ApJ*, 433, 157
- Henney W. J., 2002, *Revista Mexicana de Astronomía y Astrofísica*, 38, 71
- Henney W. J., García-Díaz M. T., O'Dell C. R., Rubin R. H., 2013, *MNRAS*, 428, 691
- Jones E., Oliphant T., Peterson P., et al., 2001–2018, SciPy: Open source scientific tools for Python, <http://www.scipy.org/>
- Joye W. A., Mandel E., 2003, in Payne H. E., Jedrzejewski R. I., Hook R. N., eds, *Astronomical Society of the Pacific Conference Series* Vol. 295, Astronomical Data Analysis Software and Systems XII. p. 489
- Kobulnicky H. A., Gilbert I. J., Kiminki D. C., 2010, *ApJ*, 710, 549
- Kobulnicky H. A., et al., 2016, *ApJS*, 227, 18
- Mackey J., Mohamed S., Neilson H. R., Langer N., Meyer D. M.-A., 2012, *ApJ*, 751, L10
- Mackey J., Gvaramadze V. V., Mohamed S., Langer N., 2015, *A&A*, 573, A10
- Markevitch M., Gonzalez A. H., David L., Vikhlinin A., Murray S., Forman W., Jones C., Tucker W., 2002, *ApJ*, 567, L27
- Meaburn J., Boumis P., Akras S., 2013, *MNRAS*, 435, 3462
- Medina S.-N. X., Arthur S. J., Henney W. J., Mellema G., Gazol A., 2014, *MNRAS*, 445, 1797
- Meyer D. M.-A., Mackey J., Langer N., Gvaramadze V. V., Mignone A., Izzard R. G., Kaper L., 2014, *MNRAS*, 444, 2754
- Meyer D. M.-A., van Marle A.-J., Kuiper R., Kley W., 2016, *MNRAS*, 459, 1146
- Meyer D. M.-A., Mignone A., Kuiper R., Raga A. C., Kley W., 2017, *MNRAS*, 464, 3229
- Mohr P. J., Phillips W. D., 2015, *Metrologia*, 52, 40
- Ng C.-Y., Bandiera R., Hunstead R. W., Johnston S., 2017, *ApJ*, 842, 100
- O'Dell C. R., Wen Z., 1994, *ApJ*, 436, 194
- Ochsendorf B. B., Verdolini S., Cox N. L. J., Berné O., Kaper L., Tielens A. G. G. M., 2014, *A&A*, 566, A75
- Penrose R., 2004, *The road to reality : a complete guide to the laws of the universe*. Jonathan Cape, London
- Phillips J. P., Cuesta L. C., Ramos-Larios G., 2010, *MNRAS*, 409, 881
- Quincey P., Brown R. J. C., 2017, *Metrologia*, 54, 454
- Raga A. C., Binette L., Canto J., Calvet N., 1990, *ApJ*, 364, 601
- Ricci L., Robberto M., Soderblom D. R., 2008, *AJ*, 136, 2136
- Robberto M., et al., 2005, *AJ*, 129, 1534
- Scherer K., Fichtner H., 2014, *ApJ*, 782, 25
- Schwartz R. D., 1978, *ApJ*, 223, 884
- Shu F. H., Lizano S., Galli D., Cantó J., Laughlin G., 2002, *ApJ*, 580, 969
- Smith N., Bally J., Shuping R. Y., Morris M., Kassis M., 2005, *AJ*, 130, 1763
- Stevens I. R., Blondin J. M., Pollock A. M. T., 1992, *ApJ*, 386, 265
- Tenorio-Tagle G., 1979, *A&A*, 71, 59
- Weisstein E. W., 1999–2018, Radius of Curvature, From MathWorld – A Wolfram Web Resource., <http://mathworld.wolfram.com/RadiusofCurvature.html>
- Wilkin F. P., 1996, *ApJ*, 459, L31
- Wilkin F. P., 1997, PhD thesis, University of California, Berkeley
- Wilkin F. P., 2000, *ApJ*, 532, 400
- Wilson A. S., Ulvestad J. S., 1987, *ApJ*, 319, 105
- Zank G. P., 1999, *Space Sci. Rev.*, 89, 413
- de Sterck H., Poedts S., 1999, *A&A*, 343, 641
- van Buren D., McCray R., 1988, *ApJ*, 329, L93
- van Dyke M., 1982, An album of fluid motion. Parabolic Press, Stanford, CA
- van Marle A. J., Meliani Z., Keppens R., Decin L., 2011, *ApJ*, 734, L26

**APPENDIX A: RADIUS OF CURVATURE**

The radius of curvature of a general curve can be written (e.g., eq. [2-5] of Guggenheimer 2012):

$$R_c \equiv \frac{1}{|\kappa|} = \left| \frac{ds}{d\alpha} \right|, \quad (\text{A1})$$

where  $\kappa$  is the *curvature*,  $s$  is the path length along the curve and  $\alpha$  is the tangent angle (see Fig. 6). In spherical polar coordinates, this becomes (Weisstein 2018):

$$R_c = \frac{\left( R^2 + R_\theta^2 \right)^{3/2}}{|R^2 + 2R_\theta^2 - RR_{\theta\theta}|}, \quad (\text{A2})$$

where  $R_\theta = dR/d\theta$  and  $R_{\theta\theta} = d^2R/d\theta^2$ . At the apex,  $R_\theta = 0$  by symmetry, which yields equation (3) of § 2. Note that  $\theta$  is dimensionless and should be measured in radians (Mohr & Phillips 2015; Quincey & Brown 2017).

**APPENDIX B: ROTATION MATRICES AND PLANE OF SKY PROJECTION**

The transformation from the body frame (unprimed) to observer-frame (primed) coordinates is a rotation about the  $y$  axis by an angle  $i$ , which is described by the rotation matrix:

$$\mathbf{A}_y(i) = \begin{pmatrix} \cos i & 0 & -\sin i \\ 0 & 1 & 0 \\ \sin i & 0 & \cos i \end{pmatrix}. \quad (\text{B1})$$

This is used in equation (8). A further application is to express the observer-frame Cartesian basis vectors in terms of the body-frame basis:

$$\hat{x}' = \mathbf{A}_y(-i) \begin{pmatrix} 1 \\ 0 \\ 0 \end{pmatrix} = \begin{pmatrix} \cos i \\ 0 \\ -\sin i \end{pmatrix}, \quad (\text{B2})$$

$$\hat{y}' = \mathbf{A}_y(-i) \begin{pmatrix} 0 \\ 1 \\ 0 \end{pmatrix} = \begin{pmatrix} 0 \\ 1 \\ 0 \end{pmatrix}, \quad (\text{B3})$$

$$\hat{z}' = \mathbf{A}_y(-i) \begin{pmatrix} 0 \\ 0 \\ 1 \end{pmatrix} = \begin{pmatrix} \sin i \\ 0 \\ \cos i \end{pmatrix}. \quad (\text{B4})$$

Note that in this case the sign of  $i$  is reversed because it is the inverse operation to that in equation (8)

Since we are considering cylindrically symmetric bows, all azimuths  $\phi$  are equivalent, so it is sufficient to work with two-dimensional curves in the plane  $z = 0$  (which is also  $\phi = 0$ ) and then find the three-dimensional surface by rotating about the  $x$ -axis via the rotation matrix:

$$\mathbf{A}_x(\phi) = \begin{pmatrix} 1 & 0 & 0 \\ 0 & \cos \phi & -\sin \phi \\ 0 & \sin \phi & \cos \phi \end{pmatrix}, \quad (\text{B5})$$

where  $\phi$  takes all values in the interval  $[0, 2\pi]$ .

**APPENDIX C: PARABOLOIDS AND THEIR PLANE-OF-SKY PROJECTION**

Equation (25) for the  $xy$  coordinates of a quadric in the  $\phi = 0$  plane cannot be used in the case of a paraboloid ( $Q = 0$ ). Instead, a

convenient parametrization is

$$\begin{aligned} x &= R_0 \left(1 - \frac{1}{2} \Pi t^2\right) \\ y &= R_0 \Pi t, \end{aligned} \quad (\text{C1})$$

where we have “baked in” knowledge of the planitude,  $\Pi = R_c/R_0$  (see § 2). The projected plane-of-sky coordinates of the tangent line follow from equation (8) as

$$\begin{aligned} x'_T/R_0 &= \left(1 - \frac{1}{2} \Pi t^2\right) \cos i + \Pi t \sin \phi_T \sin i \\ y'_T/R_0 &= \Pi t \cos \phi_T, \end{aligned} \quad (\text{C2})$$

The azimuth of the tangent line is found from equations (10, 15) as  $\sin \phi_T = -t^{-1} \tan i$ , so that

$$\begin{aligned} x'_T/R_0 &= \cos i \left[1 + \frac{1}{2} \Pi \tan^2 i - \frac{1}{2} \Pi \left(t^2 - \tan^2 i\right)\right] \\ y'_T/R_0 &= \Pi \left(t^2 - \tan^2 i\right)^{1/2}. \end{aligned} \quad (\text{C3})$$

The projected star–apex distance,  $R'_0$ , is the value of  $x'_T$  when  $y'_T = 0$ , yielding

$$R'_0/R_0 = \cos i \left(1 + \frac{1}{2} \Pi \tan^2 i\right). \quad (\text{C4})$$

Note that this same result can be obtained from a Taylor expansion of equation (45) substituted into (49) in the limit  $Q \rightarrow 0$ .

Equation (C3) can be rewritten in the form

$$\begin{aligned} x'_T &= R'_0 \left(1 - \frac{1}{2} \Pi' t'^2\right) \\ y'_T &= R'_0 \Pi' t', \end{aligned} \quad (\text{C5})$$

where

$$\Pi' = \frac{2\Pi}{2 \cos^2 i + \Pi \sin^2 i} \quad (\text{C6})$$

$$t' = \cos i \left(t^2 - \tan^2 i\right)^{1/2}, \quad (\text{C7})$$

which demonstrates that the projected shape is also a parabola. It is apparent from (C6) that the projected planitude obeys

$$\lim_{i \rightarrow 90^\circ} \Pi' = 2,$$

for all values of the true planitude  $\Pi$ , as is shown by the black lines in Figure 10a. The projected alatitude can be found as

$$\Lambda' = (2\Pi')^{1/2}. \quad (\text{C8})$$

For the special case of the confocal paraboloid,  $\Pi = \Lambda = 2$ , we have  $\Pi' = \Pi$  and  $\Lambda' = \Lambda$  by equations (C6) and (C8) for all inclinations, so its shape is unaffected by projection.

## APPENDIX D: ANALYTIC DERIVATION OF THIN-SHELL BOW SHAPE PARAMETERS

In this appendix, we provide analytic calculations of the planitude, alatitude, and asymptotic opening angle for the wilkinoid, cantoids, and ancantoids. We first consider the most general case of the ancantoids, and then show how results for cantoids and the wilkinoid follow as special cases.

### D1 Planitude of ancantoids

From equations (3) and (5), the planitude depends on the apex second derivative,  $R_{\theta\theta,0}$ , as

$$\Pi = (1 - R_{\theta\theta,0}/R_0)^{-1}. \quad (\text{D1})$$

From equation (4), the second derivative can be found from the coefficient of  $\theta^2$  in the Taylor expansion of  $R(\theta)$ . Since we do not have  $R(\theta)$  in explicit analytic form, we proceed via a Taylor expansion of the implicit equations (60) and (61), retaining terms up to  $\theta^4$  to obtain from equation (61):

$$\theta_1^2 = \beta \theta^2 \left(1 + C_{k\beta} \theta^2\right) + O(\theta^6), \quad (\text{D2})$$

with the coefficient  $C_{k\beta}$  given by

$$C_{k\beta} = \frac{1}{15} - \frac{3k}{20} - \frac{\beta}{15}. \quad (\text{D3})$$

Note that it is necessary to include the  $\theta^4$  term in the expansion of  $\theta_1^2$  so that  $\theta_1/\theta$  is accurate to order  $\theta^2$ . Then, from equation (60) we find

$$\begin{aligned} \frac{R}{D} &= \frac{\sin \theta_1}{\sin(\theta + \theta_1)} \\ &= \frac{\beta^{1/2}}{1 + \beta^{1/2}} \left\{1 + \theta^2 \left[\frac{C_{k\beta}}{2(1 + \beta^{1/2})} + \frac{1}{6}(1 + 2\beta^{1/2})\right]\right\} + O(\theta^4), \end{aligned} \quad (\text{D4})$$

where in the second line we have carried out a Taylor expansion of the two sin terms and substituted (D2). Comparing coefficients of unity and  $\theta^2$  between equations (4) and (D4) we find

$$\frac{R_0}{D} = \frac{\beta^{1/2}}{1 + \beta^{1/2}} \quad (\text{D5})$$

$$\frac{R_{\theta\theta,0}}{R_0} = \frac{C_{k\beta}}{1 + \beta^{1/2}} + \frac{1}{3}(1 + 2\beta^{1/2}), \quad (\text{D6})$$

so that the final result for the planitude, from (D1), is

$$\text{ancantoid } \Pi = \left[1 - \frac{C_{k\beta}}{1 + \beta^{1/2}} - \frac{1}{3}(1 + 2\beta^{1/2})\right]^{-1}. \quad (\text{D7})$$

### D2 Alatitude of ancantoids

To find the alatitude,  $\Lambda = R_{90}/R_0$ , we use equation (60) at  $\theta = 90^\circ$  to write

$$\Lambda = \frac{D}{R_0} \tan \theta_{1,90}, \quad (\text{D8})$$

where  $\theta_{1,90} = \theta_1(\theta = 90^\circ)$ , which, following equation (61), must satisfy

$$\theta_{1,90} \cot \theta_{1,90} = 1 - \frac{2\beta}{k+2}. \quad (\text{D9})$$

Combining (D8) and (D9) with (D5) yields

$$\Lambda = \frac{\left(1 + \beta^{1/2}\right) \theta_{1,90}}{\beta^{1/2} (1 - \xi_k \beta)}, \quad (\text{D10})$$

where

$$\xi_k = \frac{2}{k+2}. \quad (\text{D11})$$

We now take the Taylor expansion of equation (D9) to find

$$\theta_{1,90}^2 + \frac{1}{15} \theta_{1,90}^4 + O(\theta_{1,90}^6) = 3\xi_k \beta, \quad (\text{D12})$$

## 24 Tarango-Yong & Henney

which, if  $\theta_{1,90}$  is small, has the approximate solution

$$\theta_{1,90} \approx \left( \frac{3\xi_k\beta}{1 + \frac{1}{5}\xi_k\beta} \right)^{1/2}. \quad (\text{D13})$$

Substituting back into equation (D8) yields an approximate value for the alatitude of

$$\text{ancantoid } \Lambda \approx \frac{(3\xi_k)^{1/2} (1 + \beta^{1/2})}{\left(1 + \frac{1}{5}\xi_k\beta\right)^{1/2} (1 - \xi_k\beta)}. \quad (\text{D14})$$

This approximation is surprisingly accurate, with a relative error of order 1% even for  $\beta$  as large as 0.5 with  $k = 0$ .

### D3 Planitude and alatitude of cantoids and wilkinoid

Since  $\Pi$  and  $\Lambda$  depend on only that portion of the inner wind emitted in the forward hemisphere,  $\theta \leq 90^\circ$ , the results for the cantoids can be found by taking  $k = 0$ , in which case equations (D3, D7, D11, D14) yield

$$\text{cantoid } \begin{cases} \Pi = \frac{5}{3(1 - \beta^{1/2})} \\ \Lambda = \frac{\sqrt{3}}{\left(1 + \frac{1}{5}\beta\right)^{1/2} (1 - \beta^{1/2})}. \end{cases} \quad (\text{D15})$$

The wilkinoid shape is equal to the  $\beta \rightarrow 0$  limit of the cantoid, so its planitude and alatitude are given by:

$$\text{wilkinoid } \begin{cases} \Pi = \frac{5}{3} \\ \Lambda = \sqrt{3}. \end{cases} \quad (\text{D16})$$

The wilkinoid results can also be obtained directly from equation (52), and in the case of  $\Lambda$  this has already been noted by several authors (Cox et al. 2012; Meyer et al. 2016).

### D4 Asymptotic opening angle

The asymptotic opening angle of the far wings,  $\theta_\infty$ , can be found from equation (61) for the ancantoids, together with the condition that  $\theta_\infty + \theta_{1\infty} = \pi$ . These yield the implicit equation

$$\theta_\infty - \left( \frac{k+2(1-\beta)}{k+2} \right) \tan \theta_\infty = \pi + 2\beta I_k(\pi/2), \quad (\text{D17})$$

where

$$I_k(\pi/2) = \frac{\sqrt{\pi}}{4} \frac{\Gamma\left(\frac{k+1}{2}\right)}{\Gamma\left(\frac{k+4}{2}\right)} \quad (\text{D18})$$

and  $\Gamma$  is the usual Gamma function. This can be compared with the equivalent result obtained by CRW for the cantoids:

$$\theta_\infty - \tan \theta_\infty = \frac{\pi}{1 - \beta}. \quad (\text{D19})$$

Note that, unlike in the cases of  $\Pi$  and  $\Lambda$ , equation (D17) does not reduce to equation (D19) in the limit  $k \rightarrow 0$ . This is because, for  $\theta > 90^\circ$ , the  $k = 0$  ancantoid differs from the cantoid since the former has no wind in the backward hemisphere (see Figure 13). Therefore there is less inner support for the far wings of the bow, and so  $\theta_\infty$  is smaller than in the cantoid case. The wilkinoid result again follows from  $\beta \rightarrow 0$ , implying that  $\theta_\infty = \pi$ , or, in other words, that

the far wings are asymptotically parallel to the symmetry axis, as is the case for the paraboloid (App. C). In the case of the wilkinoid, however, the behavior is cubic in the wings,  $z \sim r^3$ , as opposed to quadratic as in the paraboloid.

## APPENDIX E: EMPIRICAL DETERMINATION OF RADIUS OF CURVATURE FOR A BOW SHOCK OF UNKNOWN ORIENTATION

Consider a set of  $N$  points on the plane of the sky,<sup>22</sup> with Cartesian coordinates  $\mathbf{r}_k = (x_k, y_k)$  for  $k = 1 \dots N$ . We wish to estimate the radius of curvature of the smooth curve that the set of points is presumed to be sampled from. To do this, we fit a circle to the points as follows. The circle is defined by its center,  $\mathbf{r}_c = (x_c, y_c)$ , and radius,  $R_c$ . For a given circle, we define a mean radius of the set of points from the circle center:

$$\bar{R}_c(x_c, y_c) = \frac{1}{N} \sum_{k=1}^N |\mathbf{r}_k - \mathbf{r}_c|. \quad (\text{E1})$$

We then optimize to find best-fit values  $(x_c^*, y_c^*)$ , which minimize the objective function

$$f(x_c, y_c) = \sum_{k=1}^N (|\mathbf{r}_k - \mathbf{r}_c| - \bar{R}_c(x_c, y_c))^2. \quad (\text{E2})$$

The best-fit radius of curvature is then given by  $R_c^* = \bar{R}_c(x_c^*, y_c^*)$ .

If we also know the position,  $\mathbf{r}_0 = (x_0, y_0)$ , of the bow's central source, then we can find the unit vector in the direction of the bow's projected axis as

$$\hat{\xi} = \frac{\mathbf{r}_0 - \mathbf{r}_c^*}{|\mathbf{r}_0 - \mathbf{r}_c^*|}, \quad (\text{E3})$$

and the apex distance from the source as<sup>23</sup>

$$R_0 = |\mathbf{r}_c^* + R_c^* \hat{\xi} - \mathbf{r}_0|. \quad (\text{E4})$$

A refinement of the method is then to iteratively repeat the circle fit after restricting the set of points to those lying within a certain angle  $\Delta\theta$  of the bow axis, where we find that best results are obtained with  $\Delta\theta \approx 60^\circ$  to  $75^\circ$ . That is,

$$|\theta_k| < \Delta\theta, \quad (\text{E5})$$

where the signed angle  $\theta_k$  of each point from the axis,<sup>24</sup> measured at the source position  $\mathbf{r}_0$ , can be calculated as

$$\theta_k = \arctan \left[ \frac{(\mathbf{r}_k - \mathbf{r}_0) \cdot \hat{\xi}^\perp}{(\mathbf{r}_k - \mathbf{r}_0) \cdot \hat{\xi}} \right]. \quad (\text{E6})$$

In the preceding equation, the “perpendicular” operator ( $\perp$ ) rotates its vector argument counter-clockwise by  $90^\circ$ , so that  $(x, y)^\perp = (-y, x)$ .

Two or three iterations are sufficient for convergence in most cases, although in some cases it is possible that the process will converge to a stable flip-flop oscillation between two different solutions. This is due to the dependence of the  $\theta_k$ , via  $\hat{\xi}$ , on the  $\mathbf{r}_c^*$  of

<sup>22</sup> In the main body of the paper, the prime symbol ('') is used to distinguish projected from “true” quantities. In this Appendix, for simplicity, we omit the primes since *all* quantities are projected.

<sup>23</sup> This is only valid if the resultant  $R_0 < R_c^*$ , otherwise the opposite sign of  $\hat{\xi}$  must be taken.

<sup>24</sup> Although the sign of  $\theta_k$  is not relevant to equation (E5), it is used below in calculating the perpendicular radii.

the previous iteration, which can lead to points entering and leaving the fitted set. We have not found this to be a serious problem in practice, since the two solutions tend to be very close to one another. It could be mitigated by averaging  $\mathbf{r}_c^*$  over two previous iterations. The alternative of measuring the angle with respect to the center of curvature,  $\mathbf{r}_c^*$ , instead of the source,  $\mathbf{r}_0$ , is found to be much less stable.

If quantitative estimates exist for the uncertainties,  $\epsilon_k$ , in the measurements of  $\mathbf{r}_k$ , then it is appropriate to incorporate weights of  $\epsilon_k^{-2}$  in the objective function. However, it is rare for the  $\epsilon_k$  to be objectively quantifiable, since the uncertainties are often systematic and/or subjective. In cases where the bow shape is traced by eye, based on real or synthetic observations, a more practical approach is to maintain uniform weighting but to place a greater density of points  $\mathbf{r}_k$  in regions where the shape is well-determined and to place them more sparsely in regions where the shape is less certain.

Since there is no guarantee of symmetry about the axis  $\hat{\xi}$ , the perpendicular radius will in general be different in the two wings of the bow, with values  $R_{90+}$  and  $R_{90-}$ . These can be estimated by defining

$$R_k = |\mathbf{r}_k - \mathbf{r}_0| \quad (\text{E7})$$

and linearly interpolating between the points  $(\theta_k, R_k)$  at  $\theta = \pm 90^\circ$ .

Our Python language implementation of this algorithm is freely available at <https://github.com/div-B>equals-0/circle-fit>. An example application to real data is given in § 7 and Figure 28. Note that this method is not necessary if the orientation of the bow axis is known a priori, in which case the Taylor series method described in § 2 is more efficient and accurate.

This paper has been typeset from a TeX/LaTeX file prepared by the author.